

FOOT Conceptual Design Report

1 A. Alexandrov^a, G. Ambrosi^j, S. Argirò^{b,m}, G. Battistoni^c, N. Belcari^{d,t}, S. Biondi^{e,u},
2 M. G. Bisogni^{d,t}, G. Bruni^e, S. Brambilla^c, N. Camarlinghi^{d,t}, P. Cerello^b, E. Ciarrocchi^{d,t},
3 A. Clozza^f, G. De Lellis^{a,s}, A. Di Crescenzo^{a,s}, M. Durante^g, M. Emde[†], R. Faccini^{h,o},
4 V. Ferrero^b, F. Ferroni^{h,o}, C. Finck^x, M. Francesconi^{d,t}, M. Franchini^{e,u}, L. Galli^d,
5 M. Garbini^{i,e,u}, G. Giraudo^b, R. Hetzel[†], E. Iarocci^{h,o}, M. Ionica^j, K. Kanxheri^{j,w},
6 A. Lauria^{a,s}, C. La Tessa^{g,q}, M. Marafini^{l,h}, I. Mattei^c, R. Mirabelli^{h,o}, M. C. Montesi^{a,s},
7 M. C. Morone^{i,r}, M. Morrocchi^{d,t}, S. Muraro^d, L. Narici^{i,r}, R. Paramatti^h, A. Pastore^k,
8 N. Pastrone^b, V. Patera^{h,o,l}, C. Peroni^{b,m}, M. Pullia^z, L. Ramello^{b,n}, V. Rosso^{d,t},
9 M. Rovituso^g, C. Sanelli^f, A. Sarti^{o,f,l}, G. Sartorelli^{e,u}, O. Sato^p, A. Schiavi^{h,q}, C. Schuy^y,
10 E. Scifoni^g, A. Sciubba^{o,h,l}, M. Selvi^e, L. Servoli^j, M. Sitta^{b,n}, R. Spighi^e, E. Spiriti^f,
11 G. Sportelli^{d,t}, A. Stahl[†], M. Testa^f, V. Tioukov^a, F. Tommasino^{g,q}, G. Traini^{o,h},
12 S. M. Valle^{c,v}, M. Vanstalle^x, M. Villa^{e,u}, U. Weber^y, A. Zoccoli^{e,u}

13 ^a INFN, Sezione di Napoli, Italy

14 ^b INFN, Sezione di Torino, Italy

15 ^c INFN, Sezione di Milano, Italy

16 ^d INFN, Sezione di Pisa, Italy

17 ^e INFN, Sezione di Bologna, Italy

18 ^f INFN, Laboratori Nazionali di Frascati, Italy

19 ^g INFN, Trento Institute for Physics Applications, Italy

20 ^h INFN, Sezione di Roma 1, Italy

21 ⁱ INFN, Sezione di Roma 2, Italy

22 ^j INFN, Sezione di Perugia, Italy

23 ^k INFN, Sezione di Bari, Italy

24 ^l Museo Storico della Fisica e Centro Studi e Ricerche Enrico Fermi, Italy

25 ^m Università di Torino, Italy

26 ⁿ Università del Piemonte Orientale, Italy

27 ^o Università di Roma “La Sapienza”, Italy

28 ^p Nagoya University, Japan

29 ^q Università di Trento, Italy

30 ^r Università di Roma “Tor Vergata”, Italy

31 ^s Università di Napoli “Federico II”, Italy

32 ^t Università di Pisa, Italy

33 ^u Università di Bologna, Italy

34 ^v Università di Milano, Italy

35 ^w Università di Perugia, Italy

36 ^x Institut Pluridisciplinaire Hubert Curien (IPHC), Strasbourg, France

37 ^y GSI Helmholtzzentrum für Schwerionenforschung, Darmstadt, Germany

38 ^z CNAO, Italy

39 [†] RWTH University, Aachen, Germany

41	Contents		
42	1	Introduction	4
43	2	Motivations and Research Program	7
44	2.1	Radiobiological background and Rationale	7
45	2.2	Target fragmentation in proton beam irradiation	8
46	2.3	Projectile fragmentation for oxygen beams	9
47	2.4	Projectile fragmentation for Helium beams	11
48	2.5	Radio Protection in Space	12
49	3	The design criteria of FOOT apparatus	15
50	4	The Electronic Detector Setup	17
51	4.1	Upstream Region	18
52	4.2	The tracking system	19
53	4.2.1	Magnetic Spectrometer	19
54	4.2.2	Target and Vertex Tracker	21
55	4.2.3	Inner Tracker	23
56	4.3	Downstream Tracking: the Microstrip Silicon Detector	25
57	4.3.1	LGAD amplification mechanism	26
58	4.3.2	Spatial resolution, strip pitch and multi-track separation	27
59	4.3.3	dE/dx measurements	28
60	4.3.4	Module production, thinning and mechanical issues	29
61	4.3.5	Readout channels and readout chain	30
62	4.4	ΔE and TOF Detector	30
63	4.4.1	The ΔE /TOF prototype	31
64	4.4.2	Data acquisition	32
65	4.4.3	Expected performances and preliminary results	34
66	4.5	Calorimeter	38
67	4.5.1	Preliminary test	38
68	4.5.2	Layout and planning	39
69	5	The Emulsion Spectrometer	41
70	5.1	Vertex and tracking detector	42
71	5.2	Charge measurement	43
72	5.3	Energy and mass measurements	45
73	5.4	Automated microscopy for emulsion readout	46
74	6	DAQ and Trigger	48
75	6.1	Data acquisition principles and limiting conditions	48
76	6.2	Trigger system	48
77	6.3	Data acquisition infrastructure, data rates and volumes	49
78	6.4	Online monitoring	49
79	7	Software	51
80	7.1	Simulation	51
81	7.2	Emulsion Spectrometer simulation	53
82	7.3	Reconstruction	54

83 8	Expected Performances	57
84 8.1	Study of the out of target fragmentation	57
85 8.1.1	Expected fragmentation in Start Counter	57
86 8.1.2	Expected fragmentation in Beam Monitor	57
87 8.1.3	BM and SC rejection performances	58
88 8.2	Global Tracking and Momentum Measurement	60
89 8.2.1	Momentum Performance	60
90 8.3	Calorimetric measurement	63
91 8.3.1	Calorimeter Length study	63
92 8.3.2	Calorimeter fragments study	64
93 8.4	Particle identification	67
94 8.4.1	Charge identification	67
95 8.4.2	Mass identification	69
96 8.4.3	Systematic study on the resolution of the atomic mass number A	78
97 8.5	Inverse Kinematics	84
98 9	Logistics and Timescale	88

99 1. Introduction

100 In the last decade a continuous increase in the number of cancer patients treated with Charged
101 Particle Therapy (CPT) [1] has been registered, due to its effectiveness in the treatment of deep-
102 seated solid tumors [2]. The main advantage of this approach derives from the depth-dose profile
103 of charged particles. This is characterized by an entrance channel where a low amount of dose
104 is released, followed by a narrow region, the Bragg Peak (BP), where the maximum of the dose
105 is deposited and that is usually seated on the cancer region, allowing to spare healthy tissues.
106 Furthermore the increase in Linear Energy Transfer (LET) in the BP region produces an enhanced
107 biological effectiveness in cell killing as compared to conventional photon radiation. In biophysics
108 the Relative Biological Effectiveness (RBE), ratio of photon to charged particle dose producing
109 the same biological effect, quantifies this effectiveness. Even though track structure also plays a
110 role, as a general approximation, high LET corresponds to high RBE. This effect is particularly
111 important for ions like ^{12}C , since their LET exhibit significant variations in the proximity of the
112 Bragg Peak region.

113 In proton treatment, due to the high energy of the proton beam in the entrance channel
114 and to the low and slowly varying LET, a RBE close to one would be expected. A constant RBE
115 value equal to 1.1 is currently assigned to protons in clinical practice. However, radiobiological
116 measurements show a significant increase in RBE above 1.1 [3] and the topic of RBE variability
117 in protontherapy is being widely debated in recent years. In particular, as shown in ref. [4], the
118 increase of RBE can give rise to a biological range extension after BP or to an increase of biological
119 damage in the entrance channel (plateau region in the Bragg curve), i.e. in the region of healthy
120 tissues. In fact it emerges that using a constant RBE=1.1 can lead to an underestimation of the
121 dose in the healthy tissue region.

122 An hypothesis proposed in ref. [4] is that particles produced in target fragmentation could be
123 one of the causes contributing to the increase of proton RBE. When crossing the patient, nuclear
124 interactions occur between the beam and the patient tissues. In the case of proton beams, only
125 target fragmentation occurs, generating a spectrum of low energy heavy recoils that depends on
126 beam energy and target materials. These secondary charged particles have short range (e.g. order
127 of $10\text{--}100 \mu\text{m}$), very high LET and then high RBE. In proton therapy this process can have an
128 impact in particular in the entrance channel.

129 The determination of the RBE of fragments by means of radiobiological experiments is difficult
130 and there is lack cross section data for the production of heavy recoils after proton irradiation in
131 the energy range of interest (up to 250 MeV for protons and 400 MeV/u for carbon ions). In recent
132 years some experiments have been dedicated to the study of projectile fragmentation for ^{12}C ions,
133 however this program was carried out only for a few energies [5, 6]. On the other hand the process
134 of target fragmentation, which is the only relevant process of this kind in proton therapy, so far
135 has been almost completely neglected. Actually there are some measurements of light fragment
136 ($Z < 3$) production, but there is a total lack of data for larger A values. The new experiment FOOT
137 (FragmentatiOn Of Target) has therefore been proposed.

138 The main experimental difficulty in the measurement of the target fragmentation induced by
139 proton beams is due to the short range of produced fragments that have low probability to escape
140 the target: their range is confined to tens of microns and even a very thin solid target can badly
141 spoil the fragment energy measurement. A possible workaround can be envisaged in the use of
142 gaseous target but an inverse kinematic approach can be pursued, studying the fragmentation of
143 different ions beams (C, O, Ca, etc.) onto hydrogen enriched target, such as CH_2 , as already
144 adopted in ref.[7, 5]. Secondary fragments will have boosted energy and longer range, making the
145 detection easier. The authors of ref. [5] have already shown that the cross section on H can be
146 extracted by subtraction from the coupled data obtained using both CH_2 and pure C target.

147 The final goal of the experiment would be to measure the heavy fragment ($Z > 2$) cross section
148 with maximum uncertainty of 5% and the fragment energy spectrum (in the “patient” reference
149 frame) with an energy resolution of the order of 1-2 MeV/u, in order to contribute to a better
150 radiobiological characterization of protons. The charge and isotopic identification (at the level of

151 2-3% and 5% respectively) are also important goals of this measurement. Montecarlo calculations
152 based on the FLUKA code [8, 9] predict that the heavier fragments ($Z>2$) are forward peaked within
153 a polar angle of $\simeq 10^\circ$ and with a kinetic energy per nucleon peaked around the corresponding value
154 of the primary beam, while the light fragments have wider angular and kinetic energy distribution.
155 Due to the particular interest on the heavier fragments, the experiment is focused on the detection
156 of secondary production in a narrow cone ($\simeq 10^\circ$) around the beam direction.

157 Furthermore, on top of the measurement of the target fragmentation in proton therapy, the
158 measurements of projectile fragmentation cross sections induced by C and O beams can also be
159 extended and completed. Such measurements are needed to improve the projectile fragmentation
160 description of these beams in ion therapy and their specific Treatment Planning Systems.

161 The adoption of the inverse kinematics approach asks not only for a few % level of accuracy
162 on the energy and momenta of the produced fragments, but also for a resolution on the emission
163 angle with respect to the beam direction of the order of few mrad. To achieve such an angular
164 resolution, both the beam particles direction before the target and the fragment emission angle
165 after the target must be tracked with an angular accuracy at the mrad level. Furthermore the
166 multiple scattering angle of beam+fragment couple inside the target must be kept below the mrad
167 as well. This sets a severe limit on the allowed thickness of the target (of the order of $2\div 4 \text{ g/cm}^2$)
168 and limits accordingly the probability of the fragmentation events to order of 10^{-2} .

169 The general idea is to design an experimental setup which can be easily movable (“table top”)
170 and fits the space limitations set by the different experimental and treatment rooms where ion
171 beams of therapeutic energies are available. A good trade off between the detector cost, its portabil-
172 ity and the quest for the largest possible geometrical acceptance for the heavy-forward fragments
173 reconstruction can be found using a magnetic spectrometer composed by a permanent magnet and
174 high precision tracking detectors. However, the experience from previous experiments about nu-
175 clear fragmentation, together with the study of the relevant physics process by means of Montecarlo
176 simulations, show that it’s hard to achieve the desired acceptance for all secondary fragments with
177 an apparatus of limited size. The main reason comes from the fact that lower mass fragments
178 ($Z<3$) can be emitted within a wider angular aperture with respect to heavier nuclei. Therefore
179 the necessary size, and weight, of a magnetic apparatus would become impracticable in view of a
180 table top setup design. Therefore, the FOOT experiment will consider two complementary setups:

- 181 1. a setup based on electronic detectors and a magnetic spectrometer, aiming to the identifica-
182 tion and measurement of fragments heavier than the ${}^4\text{He}$, covering an angular acceptance up
183 to $10\div 20$ degrees with respect to the beam axis;
- 184 2. a setup exploiting the emulsion chamber capabilities. As already tested in the FIRST
185 experiment[6], a specific emulsion chamber will be coupled with the pre-target devices of
186 the FOOT setup to measure the production in target fragmentation of light charged frag-
187 ments as protons, deuterons, tritons and Helium nuclei. The emulsion spectrometer supplies
188 complementary measurements for fragments emitted at large angle with respect to the elec-
189 tronic detector, extending the angular acceptance up to about 70° .

190 The R&D for experiment during 2017 has been approved and funded by INFN. Final approval
191 for the 2018-2021 period is expected in september 2017.

192 The data taking will take place mainly using C,O beams in the 150-400 MeV/u energy range.
193 Further important features of the experimental site could be the possibility to mount and calibrate
194 the experimental setup before data taking for long time (1-2 week), beam time availability in the
195 week range. The preferred site is the experimental hall of the CNAO center in Pavia, Italy with
196 the possible alternative of the HIT center in Heidelberg. A possible date for the first data taking is
197 late 2018 for the emulsion setup, while late 2019 is the target data taking for the complete setup.

198 The measurements performed with the proposed experiment could be also interesting for other
199 applications, like radioprotection in space. NASA and other space agencies have started since
200 several years the study of the risk assessment for astronauts in view of long duration space missions,
201 such for instance the travel to Mars [10]. The design and optimization of spacecraft shielding
202 requires a detailed knowledge of fragmentation processes.

203 The present Conceptual Design Review offers a quite detailed description of the physics and
204 radiobiology motivations of FOOT and of the detector design, summarizing more of one year of
205 work of the collaboration on the physics case, design optimization and performance study.

206 **2. Motivations and Research Program**

207 At the end of 2014 more than 137000 patients received Charged Particle Therapy (CPT), mostly
208 with protons (86%) and with carbon ions (11%). Interest is recently arising in the use of helium
209 and oxygen as therapeutic ions [11].

210 In proton therapy, due to low LET and to the high energy of the proton beam in the entrance
211 channel, a RBE close to one would be expected. Actually, a constant RBE equal to 1.1 is currently
212 assigned to protons in treatment planning, according to existing recommendations by ICRU[12]
213 even if the experiments show a significant increase in RBE above 1.1 (reviewed in ref. [3]). For in-
214 stance, a RBE between ≈ 1.05 and ≈ 1.18 was observed after irradiation of CHO (Chinese Hamster
215 Ovary) cells with a modulated 65 MeV proton beam [12]. At the same time, looking at the regen-
216 eration of mouse intestinal crypt cells, RBE values of 1.16 ± 0.04 and of 1.10 ± 0.03 were obtained
217 in the initial plateau with an un-modulated and a modulated proton beam, respectively [13]. The
218 topic of RBE variability in protontherapy has been widely debated in recent years (see for instance
219 ref. [14]). In particular, as shown in ref. [4] , the increase of RBE can give rise to a biological range
220 extension after BP or to an increase of biological damage in the entrance channel (plateau region
221 in the Bragg curve), i.e. in the region of healthy tissues. Using a constant RBE=1.1 can lead to
222 an under or overestimation of the dose in the healthy tissue region. This is important, since one
223 of the future goals of research and development in hadrontherapy concerns the impact on Normal
224 Tissue Complication Probability. Recently has been suggested [4] that also in the case of protons,
225 nuclear fragmentation processes (target fragmentation) can contribute to the specific mechanisms
226 inducing biological damage.

227 In the energy range of therapeutic application (50-250 MeV for protons and 50-400 MeV/u for
228 carbon ions) the fragmentation process has not been completely covered by experimental measure-
229 ments and it is necessary to rely upon simulation models. These suffer from many uncertainties
230 since there is no exact calculable theory of these nuclear processes. In recent years some exper-
231 iments have been dedicated to the study of projectile fragmentation of ^{12}C ions, however this
232 program was carried out only for a few energies [5, 6] in the lower part of the energy range of
233 interest.

234 The FOOT (FragmentatiOn Of Target) experiment has therefore been conceived in order to
235 perform a set of measurements of nuclear fragmentation cross sections which will be used to develop
236 a new generation of biologically oriented Treatment Planning Systems for proton and ion therapy.

237 In the current section and in (Sec. 2.1) the main motivations deriving from physics and radio-
238 biology are briefly reviewed, particular attention to the issues of target fragmentation in proton
239 Therapy as been devoted in Sec. 2.2 and the topic of Oxygen and Helium projectile fragmentation
240 in ion therapy respectively are addressed in Sec. 2.3 and Sec. 2.4. Further interest for a program
241 of cross section measurements is also coming from the issue of radioprotection in space missions,
242 as discussed in Sec. 2.5.

243 *2.1. Radiobiological background and Rationale*

244 The accurate measurement of nuclear fragment spectra in an ion beam induced radiation field
245 is in general of paramount importance for particle radiotherapy [15, 16] and in particular for
246 the recent trend to design biologically driven treatment planning systems (BioTPS) that aim at
247 accounting as much as possible the biological effect. Thence, even if a clinical dose prescription
248 can be approximated with pure absorbed physical dose, a realistic quantification of the radiation
249 response requires an accurate description of RBE.

250 The overall biological effect arising from the mixed radiation field in a tissue voxel is strictly
251 dependent on the components of the beam, i.e., the different fragment contributions due to particle
252 type and energy, each of them interacting with the cells producing a specific damaging result. The
253 combination of such components of the beam is not linear and is performed in a treatment planning
254 system with different beam mixing algorithms [18] in order to obtain a voxel-by-voxel description
255 of a biologically effective (RBE-weighted) dose. For example in TRIP98 [19, 20], one of the most
256 advanced BioTPS, this combination in a simplified (monodimensional) form [21] may be written

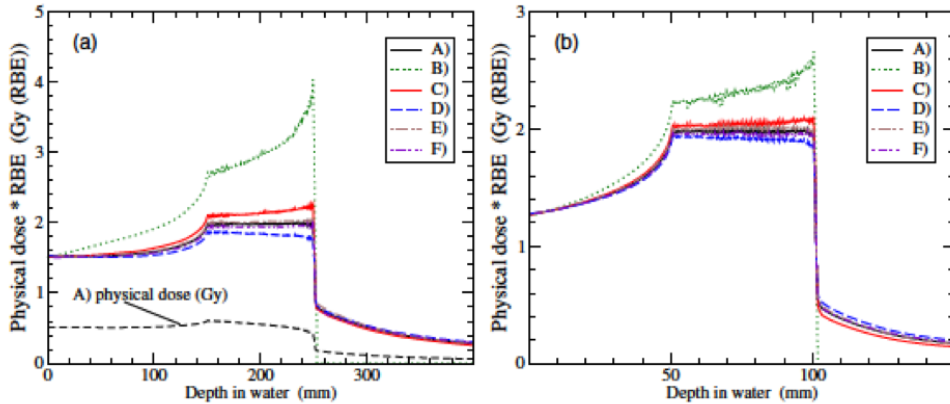


Figure 1 – Impact of Nuclear fragmentation modeling in the biological effective dose (RBE-weighted) of Carbon ion beams. 2 different cases of irradiation depths. From ref. [17]. A: Reference nuclear models of SHIELD-HIT10A; B: Turning off entirely nuclear reactions; C,D: respectively $\pm 20\%$ of all inelastic cross sections, E,F: different parameters in the Fermi-breakup model (See [17] for details.).

as an average of single particle type (Z) and energy (E) parameters, weighted by their relative abundance spectra (dN/dE) - discretized by a ΔE binning size - at a given depth z for each i_{th} initial energy of an actively scanned beam (E_0^i) and the corresponding linear energy transfer (LET=dE/dz)

$$\langle \xi \rangle = \frac{C}{D_{abs}} \sum_i N_i \sum_{Z,E} \frac{dN}{dE}(E_0^i, E, Z, z) \Delta E \frac{dE}{dz}(Z, E) \xi(Z, E) \quad (1)$$

where ξ is either α or $\sqrt{\beta}$. The weighted average $\langle \xi \rangle$ is performed on each of the two parameters defining the biological response (i.e. cell survival S , versus dose D) accordingly to the linear quadratic model ($-lnS = \alpha D + \beta D^2$), and the normalization factor, i.e. the sum of the weights, is corresponding to the absorbed dose D_{abs} scaled by a conversion constant C . The vector N_i , is the set of fluences to be irradiated for each i_{th} energy. N_i is an optimized quantity, which is tuned to give a uniform dose to the target accounting for the spectral decomposition, according to the medical prescription.

An accurate knowledge of the spectrum and cross sections of the different channels of nuclear fragmentation, may have a relevant impact on the resulting dose profile on a macroscopic scale. An example of the latter study is the sensitivity analysis performed for carbon ion in [17] (Fig. 1), by switching and scaling several inelastic processes in a Monte Carlo transport code (SHIELDIT) producing base data to be processed in TRIP98 for recalculation, after optimizing a flat RBE-weighted dose on the basis of the state of the art physics list of nuclear processes. In the explored case the sensitivity was found quite moderate: a 20% modification in all inelastic cross sections was reflected in a 3% in the overall RBE calculation.

While the fragmentation effect has been quite well characterized for carbon ions, the present challenge of the FOOT project is the characterization, in an unprecedented way, of target fragment production cross sections for proton beams. In addition, the project will provide also projectile fragment production cross sections for new, high LET ions, like oxygen beams and will cover the energy gap in available data of ^{12}C ion fragmentation cross sections.

2.2. Target fragmentation in proton beam irradiation

While for heavier ions there is broad consensus about the absolute need of accounting for RBE-weighted dose in treatment planning, BioTPS for protons is a highly debated issue recently appeared in a new attention as a possible explanation of patient toxicity data described by a Normal Tissue Complication Probability (NTCP). The commonly accepted and ubiquitously clinically

286 employed simple constant factor of 1.1 to scale the physical dose has been challenged, triggering
 287 large research efforts worldwide [22]. RBE for protons is especially regarded as important at the
 288 end of the range, but some open questions raised by the interpretation of several in vitro data are
 289 raising some open questions.

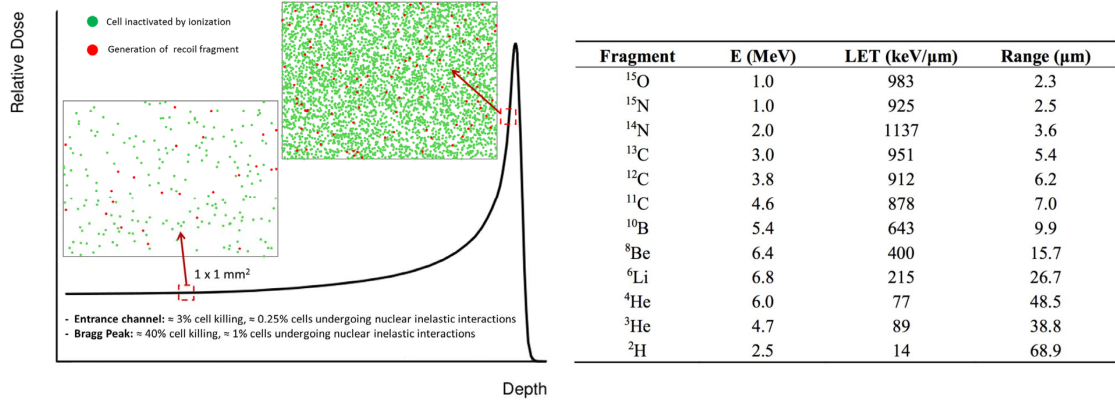


Figure 2 – Left: Illustrative image of the expected relative impact of target fragments in the entrance and in the peak regions as compared to the effect of inactivation by ionization [22]. Right: Average data for target fragments from a 180 MeV proton beam in water, estimated according to a semi-empirical formula.

290 As can be seen in Fig. 2 the target fragmentation in proton beam is more relevant in the
 291 entrance channel region, where the impact of nuclear fragmentation as compared to ionization
 292 induced cell killing is less overwhelmed than in the peak region. The fragmentation of the target
 293 nuclei in case of protons was addressed several years ago [23] and later on abandoned because of
 294 the difficulty to measure those fragments at very low energy with a reasonable accuracy. Since the
 295 target fragment spectra are extremely peaked to very low energies, this will prevent the particles
 296 traveling distances larger than few microns (see table in Fig. 2), thus making their experimental
 297 detection extremely difficult. We plan to overcome this experimental difficulty with the use of the
 298 inverse kinematic approach described later in the paper.

299 The measurement of single differential cross sections ($\frac{d\sigma}{dE}$) for such reaction channels will then
 300 open for the first time the possibility to investigate the target fragment effects on a biological level.
 301 In this case, the complete scenario of combined calculation of the mixed field is complicated by
 302 several issues. One of them is definitely the peculiar energy distribution, whose peak, differently
 303 from the typical projectile spectra, correlates with the region of maximum variation of the RBE
 304 components. This is visible in Fig. 3, where the full distribution of fragments produced by a typical
 305 proton beam at a therapeutic energy in a patient is compared to the energy distribution of the
 306 intrinsic-asymptotic RBE (RBE^*_{α}), i.e. the component of the RBE for a single particle crossing
 307 a single cell. This information is the typical biological input for TRiP98, usually computed with
 308 one of the LEM [24, 25] model versions, to be combined with spectral data. Therefore, a quite
 309 dense binning of the energy sampling in the lower end of the spectra is necessary, at least on the
 310 size of 1 MeV/u.

311 2.3. Projectile fragmentation for oxygen beams

312 In addition to the above mentioned data, FOOT will be able to provide other data from
 313 direct kinematics which are of great importance. This is in particular the case of Oxygen beam
 314 fragmentation data.

315 Oxygen beams are increasingly considered [11] as a fundamental tool against hypoxic tumours.
 316 Further advancement in BioTPS are indeed taking into account, beyond the RBE effect, additional
 317 biological information, like the oxygenation of a tissue [27], returning a voxel-by-voxel different
 318 sensitivity to the released dose quantified by the oxygen enhancement ratio (OER). Intra-tumour

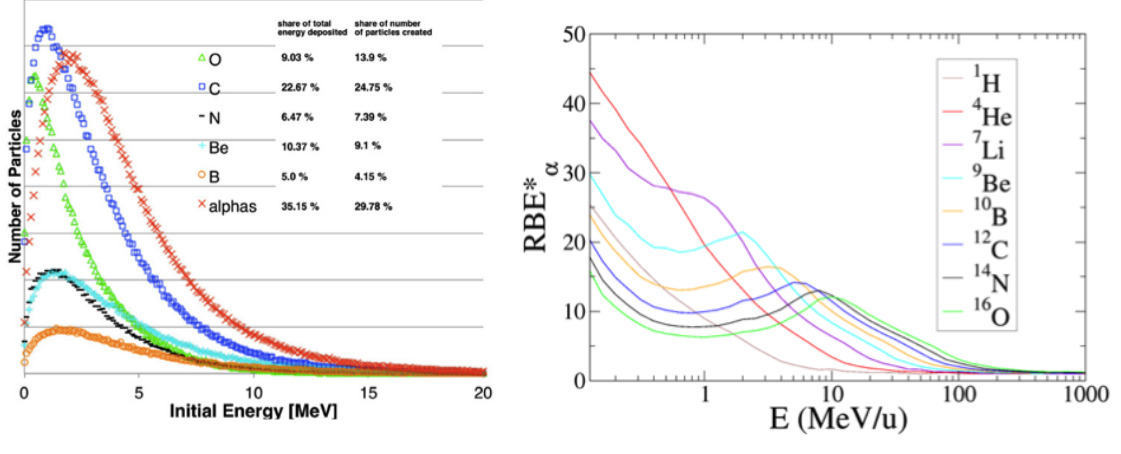


Figure 3 – Left: Full spectra of fragments from target media in the case of a prostate irradiation with protons of 160 MeV, integrated in the complete range of beam propagation (from [26]) Right: estimates of single particle traversal maximum RBE (intrinsic asymptotic) computed with LEM-IV model (data courtesy of T. Friedrich) for a specific cell type (CHO-k1) and different particles as available in the TRiP98 base dataset (with consistent color code).

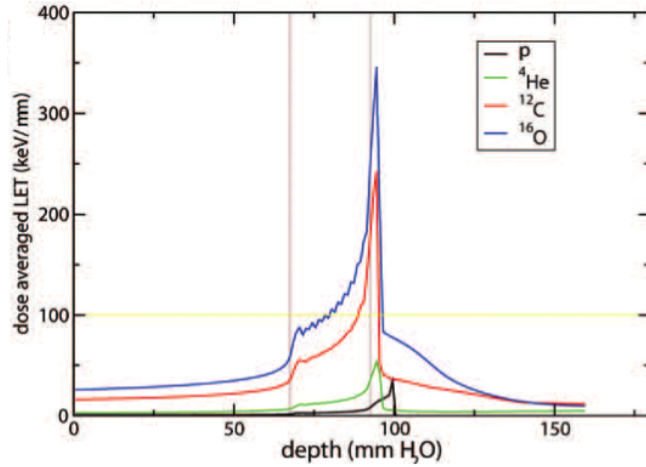


Figure 4 – Dose averaged LET profile across an extended target irradiation, as compared to other ions (the yellow line at 100 keV/ μ m indicates a value where OER significantly reduces)

319 heterogeneity and dedicated radiotherapy adaptive (painting) strategies represent a very important
 320 research direction.

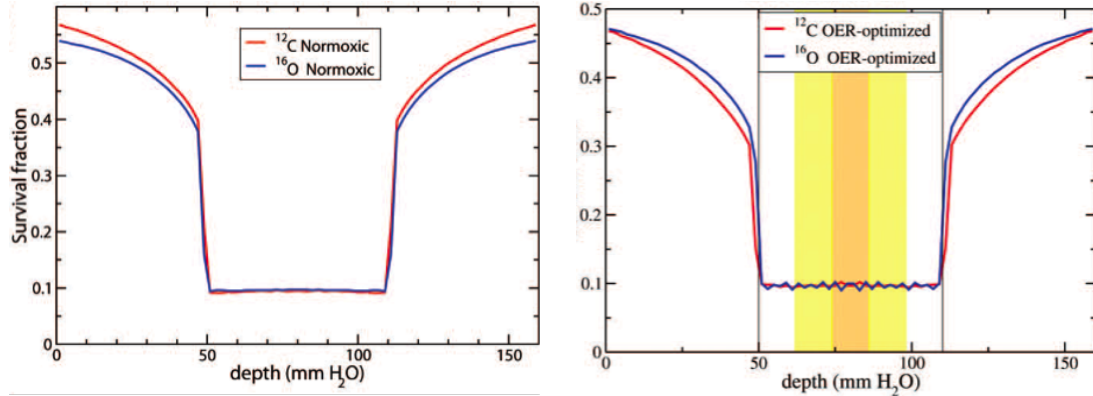


Figure 5 – survival profiles for 2 opposed ion fields for C and O in a normoxic, left, and in a partially hypoxic tumor, right (orange 0% ,yellow 0.5% pO₂ from ref [28]).

321 Since it has been shown that OER decreases substantially with LET, especially beyond \sim
 322 100keV/ μ m, the rationale for using O beams is basically driven by their similar characteristics
 323 as compared to carbon, but with an importantly larger LET distribution overall a typical target
 324 length, able to overcome such threshold value (see Fig. 4) and thus to be effective in contrasting
 325 hypoxia (lack of cell oxygenation, see Fig. 5 right). However, in normal (aerobic) conditions, the
 326 larger fragmentation of O beam in the target and entrance channel, makes their use less convenient
 327 as compared to lower Z ions (such as C), producing a worse differential profile between killing
 328 in the target and in the entrance channel (peak-to entrance ratio) as shown in Fig. 5 left. The
 329 challenge in an assessment considering a possible use of Oxygen is then a trade-off between the LET
 330 advantage and the worse fragmentation in the normal tissue, which should be evaluated, case by
 331 case, accordingly to geometry, tissue sensitivity and other patient based characteristics. In most of
 332 the cases, oxygen beam is envisaged not as a full alternative option, rather as a boost in combination
 333 with other types of (lower LET) particles. In any case, the correct assessment of the potential use
 334 of this new beam is strictly related to a very accurate description of its fragmentation cascade, for a
 335 large range of initial energies and in the complete range of its propagation. Additionally, the correct
 336 description of the physical products in an oxygen beam, will contribute also for the estimation of
 337 the dose averaged LET itself, thus contributing also, at the same time, in the assessment of the
 338 OER reduction.

339 2.4. Projectile fragmentation for Helium beams

340 Finally, growing interest is dedicated to a possible use of Helium beams [29]. Helium is regarded
 341 as a promising alternative to protons, with a cost/benefit ratio of implementation more affordable
 342 compared to higher LET ions (Carbon). The advantage of introducing helium ions over protons is
 343 related mainly to the lower impact of multiple Coulomb scattering, allowing an higher resolution
 344 in close lateral proximity of organs at risk [27] (see Fig. 6). In addition, the effect of RBE (and
 345 then the need of BioTPS) is established as not negligible for helium, increasing substantially the
 346 biological effectiveness in the target. As compared to Carbon, on the other hand, helium, beside the
 347 mentioned lower cost, is convenient for a much lower impact of nuclear fragmentation, especially in
 348 the tail after the peak. This is an important constraint, especially in pediatric tumors, for example
 349 in a crano-spinal irradiation of a medulloblastoma, where the dose coverage should necessarily
 350 stop right after the target, and which is one of the reasons why at the moment carbon ions have
 351 been not employed for such cases [28].

352 Recent measurements have started feeding data for Helium ions [30] [31] [32], and FOOT will
 353 allow extending also this database with unprecedented accuracy.

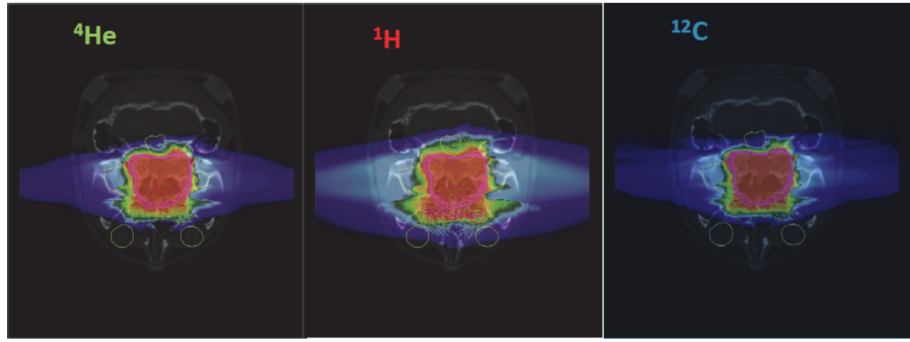


Figure 6 – Comparison of treatment plans on a skull chordoma, with two opposed fields of different ions, showing the intermediate behavior of Helium ions, much more convenient as compared to protons in case of laterally seated organs at risk (adapted from [27]).

All the above mentioned issues are at the core interest of the MoVe IT (Modeling and Verification in Ion Beam treatment planning) - INFN CSN5 Call project (www.tifpa.infn.it/projects/move-it/), aiming at advancing BioTPS towards the most important open challenges in particle therapy and allowing a realization of comparative TPS studies for all the most relevant ions available in the state-of-the art centers, which could be able to provide selective indications for different patient cases.

2.5. Radio Protection in Space

The measurements performed with the proposed experiment could be also interesting for other applications, like radioprotection in space. NASA and other space agencies have started since several years the study of the risk assessment for astronauts in view of long duration space missions, such for instance the travel to Mars [33]. Beyond many important risks of other nature several radiation sources in space have to be considered, then the design and optimization of the spacecraft shielding requires a detailed knowledge of the fragmentation processes.

There are three main sources of energetic particles in space: Solar Particle Events (SPEs), Galactic Cosmic Rays (GCR) and the geomagnetically trapped particles.

SPEs are mainly composed by protons emitted from the sun during coronal mass ejections and solar flares. Their energy spectrum can reach the GeV region and, being unpredictable, they can inflict a lethal dose to the astronauts. GCRs consist of high energy protons and highly energetic charged particles (HZE) originated from supernovae within the Milky Way Galaxy whose energy spectrum ranges from MeV to TeV. The elemental abundance and energy spectrum of the Galactic Cosmic Rays are well known (86% of protons, 12% of alpha particles, 1% of heavier ions like C, Si and Fe) but their biological effects are poorly understood, even though they are one of the most significant hazard for humans in space. Even if heavy ions are rare with respect to protons and alphas they contribute significantly to the total dose because of its dependence from the square of the nuclear charge ($D \propto Z^2$). Moreover, the GCR radiation cannot be easily shielded because of the nuclear fragmentation into lighter and thus more penetrating ions.

The geomagnetically trapped particles consist of protons and electrons confined by the Earth magnetic field in two regions, called Van Allen belts. Protons reach energies up to a few hundreds MeV in the inner belt and electron up to 100 keV in the outer belt.

For the radiation exposure in space exploration risk assessment the accurate knowledge of the particles spectrum in terms of composition and energy at various sites in the solar system is not sufficient. In space the outer radiation is modified by the interaction with the walls of the spacecraft and its shielding material creating a mixed field. To quantify the radiation field inside the vessel, and thus the cumulative dose received by the astronauts, the atomic and nuclear interactions occurring between the incoming particles and material of/in the spacecraft have to be characterized. Dose estimates can be obtained through direct measurements or calculations

390 with deterministic and Monte Carlo transport codes and an essential ingredient for validating and
 391 benchmarking the codes are the cross sections related to the processes of interest. For example,
 392 nuclear cross sections describe the slow-down of the primary ion and its nuclear fragmentation.

393 An overview of the nuclear cross section already available can be found in [34]. The review
 394 identifies the gaps in the data and recommends future measurements with a focus on space radi-
 395 ation. Figures 7-8 show the available measurements of double differential cross sections in energy
 396 and angle for protons and medium-light fragments ($Z_F = 3 - 9$), respectively. The data are plotted
 397 as a function of projectile and target charge Z and divided into two projectile energy ranges (below
 398 290 MeV/u and between 290 MeV/u and 3 GeV/u). Recommendations for future measurements
 399 are summarized in Table 9 for Hydrogen (top) and medium-light fragments (bottom).

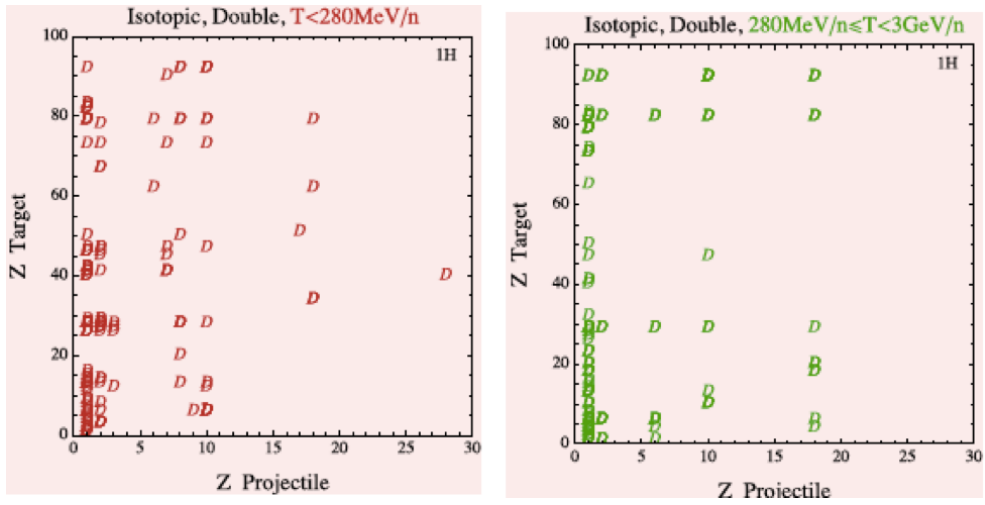


Figure 7 – Double differential cross sections available from literature for the production of protons. The data are shown as function of projectile and target charge Z and divided into two projectile energy ranges (below 290 MeV/u and between 290 MeV/u and 3 GeV/u).

400 There is a common ground between protecting astronauts from the harmful effects of space
 401 radiation and providing tumor therapy to patients using ions. The pool of particle species currently
 402 available in radiotherapy (protons and Carbon) or considered as promising alternative candidates
 403 (Helium, Lithium and Oxygen) are among the most abundant in space. The overlap is also in terms
 404 of energy, especially around the pion threshold which is near the optimum for tumor therapy. This
 405 is the same energy region of the solar flare protons and Van Allen trapped protons as well as near
 406 the peak of the GCR spectrum. The shared interest of ion species and energy range between space
 407 radioprotection and hadrontherapy allows the interchange of cross sections data. In both fields,
 408 isotopic cross sections provide the best test of theoretical models. Double differential cross sections
 409 for light ions are especially important, as they have high penetrating power and large angular
 410 spread from the primary beam. Measurements on hydrogen targets are missing and thus required,
 411 as hydrogen-rich materials are among the best shielding options. Modeling the interactions of light
 412 projectiles and/or light targets is a difficult task, as they do not follow the systematics of heavier
 413 system and have to be investigated separately.

414 The measurements campaign proposed within the FOOT project will fill several of the existing
 415 gaps in the nuclear cross sections database as indicated by the data reported in Table 9. The
 416 experimental setup allows a complete characterization of all fragments, thus providing isotopic
 417 double differential cross sections which are the optimal data for model benchmarking.

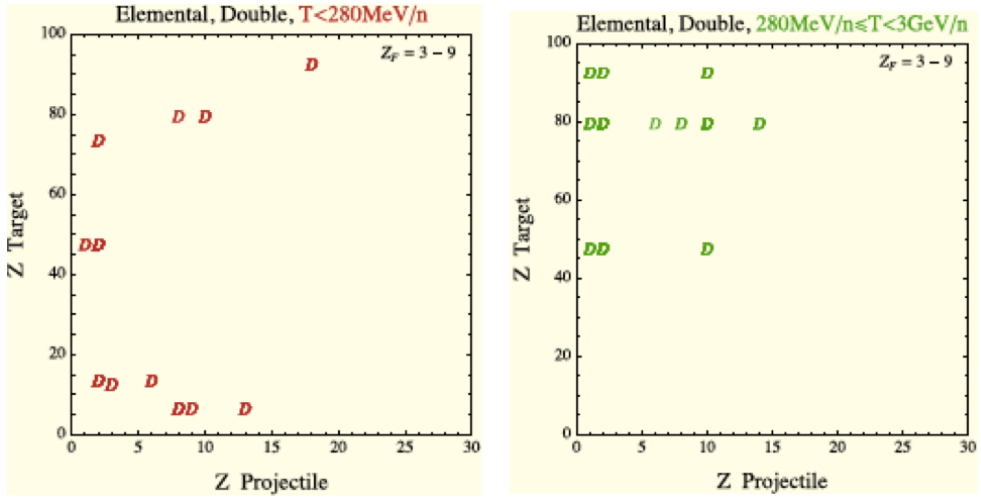


Figure 8 – Double differential cross sections available from literature for the production of medium-light fragments ($Z_F = 3 - 9$). The data are shown as function of projectile and target charge Z and divided into two projectile energy ranges (below 290 MeV/u and between 290 MeV/u and 3 GeV/u).

Cross-section	Fragment	Below π threshold projectile	Low energy projectile	Medium energy projectile	High energy projectile
σ	H	All	He,O, Si, Fe(T)	All	All
	$^{1,2,3}\text{H}$	He(T), C, O(H), Si, Fe	He($\frac{1}{2}$), O(T), Si, Fe	He(H), C($\frac{1}{2}$), O, Si, Fe	All
$dE/d\Omega$	H	All	All	All	All
	$^{1,2,3}\text{H}$	He(H), C, O(H), Si, Fe	O, Si, Fe	All	All

Cross-section	Fragment	Below π threshold projectile	Low energy projectile	Medium energy projectile	High energy projectile
σ	Elemental	C(T), O, Fe	—	C($\frac{1}{2}$), O(H), Fe	CFe
	Isotopic	C(H), O, Si, Fe	Fe($\frac{1}{2}$)	C($\frac{1}{2}$), O, Si(H), Fe	C, O, Si, Fe
$dE/d\Omega$	Elemental	C, O, Si, Fe	C, O, Si, Fe	C, O, Si, Fe	C, O, Si, Fe
	Isotopic	C, O, Si, Fe	C, O, Si, Fe	C, O, Si, Fe	C, O, Si, Fe

Figure 9 – H (top) and medium-light ($Z_F = 3 - 9$) (bottom) elemental and isotopic fragment measurement recommendations. A complete measurement set for C, O, Si and Fe projectiles would be required to fill this gap. Projectiles needed for only H targets are listed with (H). Projectiles needed for a range of targets, except H, are listed with (\mathcal{H}). No parentheses indicates that a range of targets, including H, is needed. The notation (T) means that only a few additional targets are required. H projectiles are not considered.

418 **3. The design criteria of FOOT apparatus**

419 The design of the detector is driven mainly by the radiobiology outcome requests. In particular
420 the main challenge is the detection of very short range (order of tens of microns) and very low
421 energy (few MeV) fragments produced by the target fragmentation of the proton beam. To this
422 aim an inverse kinematic approach can be pursued, studying the fragmentation of different ions
423 beams (C, O, Ca, etc.) onto hydrogen enriched target, such as CH₂, as already adopted in ref. [5, 7]
424 where secondary fragments in the inverse kinematic reference frame have boosted energy and a
425 much longer range, making their detection easier. The authors of ref. [5] have already shown that
426 the cross section on H can be extracted by subtraction from the data obtained using a pure C
427 target. Some other details are given in Section 8.5

428 The adoption of the inverse kinematics approach asks not only for a few % level accuracy on
429 the measurement of the energy and momenta of the produced fragments, but also for an emission
430 angle resolution with respect to the beam of the order of few mrad. To achieve such an angular
431 resolution, both the beam particles direction before the target and the fragment emission angle
432 after the target must be tracked with an angular accuracy at the mrad level. Furthermore the
433 multiple scattering angle of beam+fragment couple inside the target must be kept well below the
434 mrad. This sets a severe limit on the allowed thickness of the target (of the order of 2÷4 mm) and
435 limits accordingly the probability to have the fragmentation in the target at the order of 10⁻².

436 The general idea is to design an experimental setup which can be easily transportable (“table
437 top setup”) for two main reasons. The different beams needed will be available in various treatment
438 and research centers requiring then a transportability easiness. Moreover the limited dimension
439 of the available experimental and treatment rooms where ion beams of therapeutic energies are
440 available. The second main constraint is the redundancy of the fragment features measurement:
441 contemporary detection of momentum, velocity and kinetic energy are needed to study with limited
442 systematics the produced fragments in the energy range of interest.

443 A good balancing between the detector cost, its portability and the quest for the largest possible
444 geometrical acceptance for the heavy-forward peaked fragments reconstruction can be found using a
445 magnetic spectrometer composed by a permanent magnet with an high precision tracking system.
446 However, the experience from previous experiments about nuclear fragmentation, together with
447 the study of the relevant physics process by means of Montecarlo simulations, show that it's hard
448 to achieve the desired acceptance for all secondary fragments with an apparatus of limited size.
449 The main reason comes from the fact that lower mass fragments, protons, deuterons, etc., can be
450 emitted within a wider angular aperture with respect to heavier nuclei. Therefore the necessary
451 size, and weight, of a magnetic apparatus would become impracticable in view of a table top setup
452 design. Therefore, the FOOT experiment will consider to implement two different setups:

- 453 1. a setup based on electronic detectors and a magnetic spectrometer concept, aiming to the
454 identification and measurement of fragments heavier than ⁴He, covering an angular acceptance
455 up to 10÷20 degrees with respect to the beam axis;
 - 456 2. a setup exploiting the emulsion chamber capabilities. As already tested in the FIRST ex-
457 periment [6], a specific emulsion chamber will be coupled with the interaction region of the
458 FOOT setup to measure the production in target fragmentation of light charged fragments
459 as protons, deuterons, tritons and Helium nuclei. The emulsion spectrometer supplies com-
460 plementary measurements for large angle fragments with respect to the electronic detector,
461 extending the angular acceptance up to about 70 degrees.
- 462 The FOOT measurements related to radio protection in space are the measurement of the frag-
463 mentation cross section of H, ⁴He and ¹²C beam with kinetic energy extended up to 1GeV/u on
464 C and C₂H₄ targets. For this measurement the main focus is the Z identification. We foresee to
465 detect the light fragments with the emulsion setup and the heavier ones with the electronic setup.
466 In particular the electronic setup will be modified according to the higher kinetic energy of the
467 beam.

468 The angular aperture of the produced fragments will decrease with the increase of the kinetic
469 energy. At beam kinetic energy of 1 GeV/u the fragments will have an aperture of 2-4 deg. This
470 will allow not only to move the calorimeter at longer (double) distance to have longer lever arm for
471 the TOF measurement, but also to move the magnets downstream , doubling the distance between
472 the magnetic elements to ease the bending measurement. The reduction of the fragments multiple
473 scattering in air (due to higher momentum) will compensate the increase of the path travelled.
474 the stretching of the detector size is not a real issue for this measurements, since the beams with
475 the needed energy of $\simeq 1\text{GeV}/U$ are available only in research facility as GSI where the space
476 limitation is by far less severe than in a treatment center.

477 The setup of the electronic detector is described in Section 4, while the emulsion spectrometer
478 setup is discussed in Section 5.

479 **4. The Electronic Detector Setup**

480 One of the main requirements of the FOOT detector design is a robust charge and isotopic
481 identification of the produced fragments. Therefore the setup measures the following quantities of
482 the fragments produced: momentum, kinetic energy, Time Of Flight (TOF). The fragment dE/dx
483 is measured twice through the energy release (ΔE) in a thin slab of plastic scintillator and thin
484 silicon detector. The detector performances to be achieved are the following:

- 485 • momentum resolution $\sigma(p)/p$ at the level of 5%;
486 • time of flight (TOF) resolution at the level of 100 ps;
487 • energy resolution $\sigma(E_k)/(E_k)$ at the level of 2%;
488 • $\sigma(\Delta E)/(\Delta E)$ at level of 2%;

489 These performances must be achieved on the heavier fragment (C,N,O) that are the most
490 difficult to be correctly identified, and can be released on the lighter particles produced. The
491 charge can be identified by crossing the ΔE measurements with TOF or kinetic energy, while
492 the mass can be extracted by momentum and kinetic energy measurements through the following
493 relationships:

$$p = mc\beta\gamma \quad E_k = mc^2(\gamma - 1) \quad E_K = \sqrt{p^2c^2 + m^2c^4 - mc^2} \quad (2)$$

494 where $\beta = \frac{v}{c}$ and $\gamma = \frac{1}{\sqrt{1-\beta^2}}$ are derived from the fragment TOF.

495 The fragmentation contribution due to detector material must be kept as low as possible,
496 evaluated using both MC and data itself and finally subtracted.

497 Designing the detector as compact as possible makes it capable of exploiting particle beams
498 at different therapeutic centers: Centro Nazionale di Adroterapia Oncologica (CNAO) in Pavia
499 (Italy) or Heidelberg Ion Therapy Center (HIT) in Heidelberg (Germany). As a consequence the
500 overall detector size should lie within the 1.5-2 meters range. GSI beam can be considered as well.

501 The design of the detector was driven by the FLUKA simulation of the fragmentation. The
502 nuclear models embedded in FLUKA are not yet fully satisfactory for the clinical application, but
503 they are sufficiently robust to drive the detector design. The experience of the FIRST experiment
504 at GSI[6] was also exploited. The detector geometry is driven by two main factors: the emission
505 angle of the (heavy) fragments and the angular separation between two fragments emitted in the
506 same events. The first item decides the angular acceptance while the second rules the granularity.
507 An example of the prediction from Monte Carlo calculation is given in Figs. 10 and 11 where the
508 angular distribution of different fragments produced by a 200MeV/u ^{16}O beam impinging on a
509 C_2H_4 target, and their angular separation, are shown as resulting from the FLUKA code [8, 9].

510 The detector can be divided downstream in three different regions: the upstream/target region,
511 the magnetic tracking region and the calorimeter region. A schematic view of the detector is shown
512 in Fig. 12

- 513 • The target and vertexing region. Here the beam crosses a thin plastic scintillator counter
514 ($250\mu\text{m}$) that provides trigger information and the start of the TOF. A drift chamber acts
515 as beam monitor, tracks the beam direction and position. The target is the last element of
516 this region.
- 517 • The magnetic spectrometer. A telescope of pixel trackers provides the vertex reconstruction
518 and the initial tracking of the produced fragments, following the experience gained in the
519 FIRST experiment[6, 35]. Then the fragments enter in a magnetic region, where the field is
520 provided by two permanent dipole magnets (Halbach geometry). Between the two magnets,
521 the fragment direction is measured by two additional layers of silicon pixel trackers. At the
522 exit of the magnet systems, a telescope of silicon microstrips provides a further precision
523 tracking and the first measurement of the fragment $\frac{dE}{dx}$. All these tracking elements allow
524 the measurement of the fragment momentum.

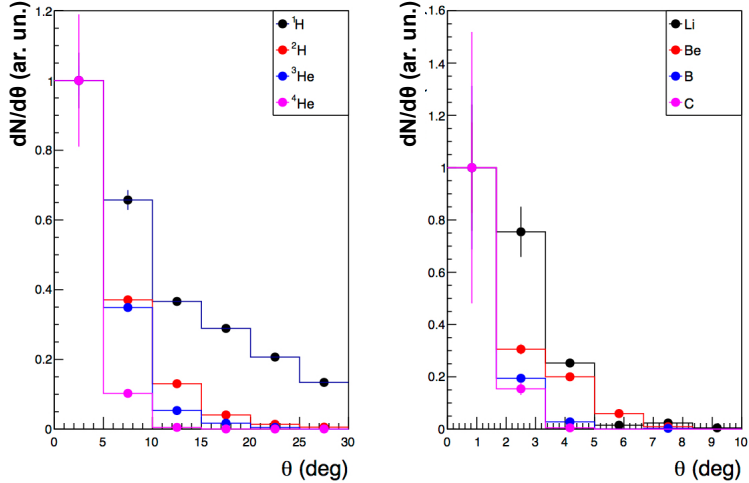


Figure 10 – MC calculation [8, 9] of the angular distribution of different fragments produced by a 200MeV/u ^{16}O beam impinging on a CH_2 target.

- 525 • The calorimeter region. Downstream the magnetic spectrometer the fragments travel ~ 1
526 meter to reach a ΔE and TOF detector made of two orthogonal planes consisting of 3mm
527 thick, 40 cm long plastic scintillator rods. Finally the fragments kinetic energy is measured
528 in a $\simeq 10\text{cm}$ thick BGO crystal calorimeter. The 20 cm radius of the calorimeter is dictated
529 by the emission angle of the heavy fragments, while the $2 \times 2\text{cm}^2$ granularity of the crystals
530 in the transverse plane is requested to keep the events with multiple fragment impinging in
531 one crystal below the % level.

532 The nuclear interactions of fragments in the calorimeter affect the measurement of energy release
533 because of processes where “invisible energy” is produced. One of the most relevant cause are
534 neutrons which punch through the crystals and this occurs in 10~20% of events, depending on
535 energy. Multiple independent measurements of the fragment mass allow to detect the presence of
536 those neutrons.

537 *4.1. Upstream Region*

538 The Start Counter (SC) has been already used in the FIRST experiment[6], and it is made
539 of by a $250 \mu\text{m}$ thick scintillator disk, a EJ-228 fast scintillator foil, with a radius of 26 mm,
540 sufficient to cover the typical beam transverse size. As shown in Fig. 13, the light produced in the
541 scintillator is collected radially by 160 optical fibers grouped in four bundles and readout by fast
542 PMT Hamamatsu H10721-210 with 40% quantum efficiency. The thickness of the scintillator was
543 minimized to reduce the pre-target particle interaction probability, less than 5% with respect to
544 the on-target one, assuming a 2mm thick graphite target.

545 The SC, placed 20-30 cm upstream of the target, provides the trigger signal to the whole
546 experiment and the measurement of incoming ion flux to be used for the cross section measurement.
547 The SC provides the reference time for all the other detectors and allows the TOF measurement in
548 combination with the ΔE -TOF scintillator detector. Details of the detector are shown in Fig. 13

549 The SC performances on a LNS ^{12}C beam with kinetic energy of 80 MeV/u have been reported
550 in ref. [35] showing an excellent efficiency very close to unity. A time resolution of the order of
551 $\sigma_t = 100\text{ps}$ has been measured using only one of the four channels of the device. Such a results
552 indicate that the SC can fulfill the FOOT detector requirements.

553 The Beam Monitor (BM) is a drift chamber consisting of twelve layers of wires, with three drift
554 cells per layer. Planes with wires oriented along the x and y axes are alternated in such a way to

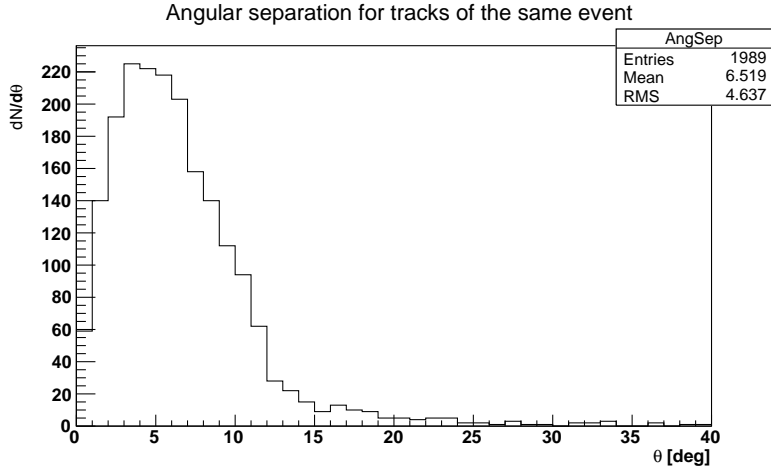


Figure 11 – MC calculation [8, 9] of angle separation between different fragments produced by a 200MeV/u ^{16}O beam impinging on a CH_2 target.

reconstruct the beam profile. The cell shape is rectangular ($16\text{mm} \times 10\text{mm}$) with the long side orthogonal to the beam. In each view two consecutive layers are staggered by half a cell to solve left-right ambiguities in track reconstruction [35]. The BM was operated at atmospheric pressure, at the working voltage of 1.8 kV in Ar/CO₂, 80/20 gas mixture. The BM efficiency was measured to be close to unity for carbon ion beam and the mean track spatial resolution was measured to be of the order of $\simeq 140 \mu\text{m}$ [36, 37]. A technical drawing of the chamber is shown in Fig. 14.

The BM detector will be placed between the SC and the target and will be used to measure the direction and impinging point of the ion beam on the target, a crucial information needed to address the pile-up ambiguity in the slow VTX detector (readout time = $187\mu\text{s}$). In fact the BM read-out time, of the order of $1 \mu\text{s}$ or less, is fast enough to ensure that tracks belonging to different events cannot be mixed. In pile-up events, the vertices reconstructed in the pixel vertex detector (VTX) are randomly distributed with a shape dictated by the transverse size of the beam. In our baseline CNAO or HIT facilities, the beam spot is a gaussian with FWHM of the order of a few mm. The positions of the vertices reconstructed by the VTX for each event can be compared with the position of the BM track extrapolated to the target, and only the closest vertex to the BM extrapolation is selected as matched vertex. For this reason a precision of few hundred μm in the impact point provided by the BM is needed to discriminate the right vertex in pile-up events. Of course this procedure requires a good alignment between BM and VTX.

4.2. The tracking system

The overall tracking system of FOOT is conceived as a magnetic spectrometer arranged in three measuring stations. The needs in terms of momentum resolution and global acceptance together with the minimization multiple scattering and re-fragmentation in both the sensors and mechanical structures themselves suggest the use of monolithic pixel sensors in the two upstream stations, while a telescope of silicon microstrip detectors (MSD) can be envisaged for the downstream station. In the following we shall describe the magnetic setup, the two upstream tracking stations, the mechanical structure holding the VTX and the magnets designed to bend the fragments in their path from the vertex to the inner tracker and the MSD telescope.

4.2.1. Magnetic Spectrometer

A key element for the FOOT spectrometer is the magnetic system used to bend the fragments produced in the target. The main constrains are the momentum resolution at the level of few percent and the portability of the system. We'll briefly discuss both.

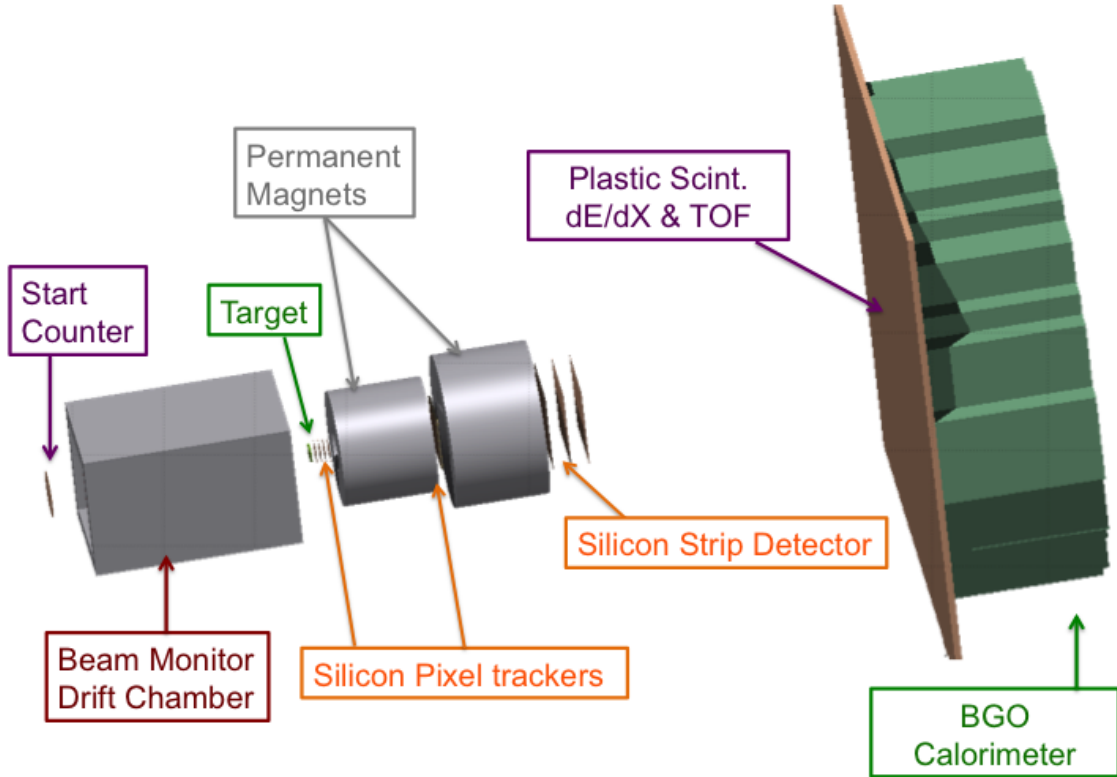


Figure 12 – Schematic view of the FOOT apparatus.

587 The momentum resolution is defined by the identification capability of the atomic mass number
 588 for the different fragments and for projectiles like Carbon or Oxygen and by the requirements
 589 to reconstruct the Linear Energy Transfer (LET) of the fragments produced by protons in the
 590 Hadrontherapy treatment by means of the inverse kinematics approach. Moreover for the direct
 591 fragmentation measurements the momentum resolution is essential for the double differential cross
 592 section.

593 The portability of the system is also essential. The portability forces choice of permanentmagnets
 594 producing the needed $B * L$ in a limited sizes and weight.

595 A preliminary feasibility study has been done to evaluate the performances we could get with
 596 this kind of solution [38]. A Halbach (showed in Fig. 15) and Halbach-like configuration have
 597 been studied: the dipolar magnetic field is obtained with a cylindrical geometry with the internal
 598 cylindrical hole being the region where the magnetic field is rather uniform. The magnetic structure
 599 is made of twelve single pieces: their material and dimensions affect the final magnetic field. For
 600 the material two options are typically available: the SmCo (Samarium-Cobalt) and the NeFeB
 601 (Neodymium-Iron-Boron). Both the thickness of the single Permanent Magnet (PM) and the
 602 material used contribute to the strength of the produced field.

603 Simulations with the SmCo material in different configurations have been done in 2D and 3D.
 604 2D simulation used the “2D Pandira” code from a code for Permanent Magnets developed at the
 605 Los Alamos laboratories providing the transversal field map for an infinite length magnet. 3D
 606 simulations were performed with the OPERA code version 16R1. 2D simulations aiming at a 0.6
 607 T field in the center of the magnet have shown that a uniformity at the percent level in the field
 608 strength in a region extending up to 3 cm from the magnet axis is possible for a configuration with

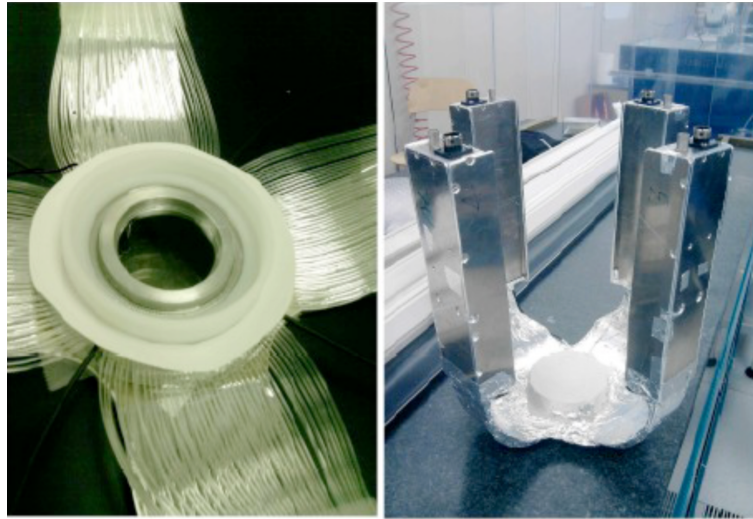


Figure 13 – Details of the Start Counter: the thin scintillator foil and the optical fibers grouped in four different arms.

609 an internal aperture of 7 cm and a thickness of the PM of 3.5 cm. Moreover 2D simulations have
 610 shown an almost linear dependence of the field amplitude in the center versus the thickness of the
 611 magnetic blocks, reaching 0.9 Tesla with 6.5 cm thickness.

612 The 3D simulation produces the behaviour of the field on the axis for a length of the magnet
 613 similar to the internal diameter. Assuming a magnet length of 9 cm and a thickness of the magnetic
 614 material of 3.5 cm like in the 2D simulation, the maximum field strength in the center is 0.51 Tesla.
 615 This value can be restored to 0.6 Tesla by increasing the PM thickness to 4.5 cm. It can be further
 616 improved to 0.9 Tesla raising the thickness of the PM to 11 cm.

617 An additional simulation was performed for the two magnet configuration. The field along the
 618 two magnet central axis is shown in Fig. 17 : it behaves like the sum of two gaussian functions with
 619 displaced and symmetric centers. This features indicates that the inner tracker, sitting in-between
 620 the two magnets, will experience a field at the level of 0.6 T, depending on the distance from the
 621 magnets.

622 The required level of performances can be achieved with a total weight and size that is com-
 623 patible with the inspiring concept of portability. The mechanical structure needs to be sufficiently
 624 robust to withstand to the magnetic forces produced by all this amount of permanently magnetic
 625 material. The robustness of the mechanical structure has also an impact on the overall precision
 626 that could spoil the intrinsic accuracy of about 10 μm achievable with the sensors. Needless to
 627 say, a detailed field map has to be produced with the expertise and tools available at the Frascati
 628 Laboratories.

629 4.2.2. Target and Vertex Tracker

630 The Vertex detector implementation will profit of the experience of the FIRST experiment and
 631 will use the same mechanical structure. It holds up to five different targets in a sliding tray that
 632 can eventually be moved also automatically by a remote controlled actuator as shown in the left
 633 picture of Fig. 18. The stack of sensors is placed as shown schematically in the right side of Fig. 18:
 634 this arrangement guarantees an acceptance at the level of about ± 40 degrees for the fragments
 635 produced in the target.

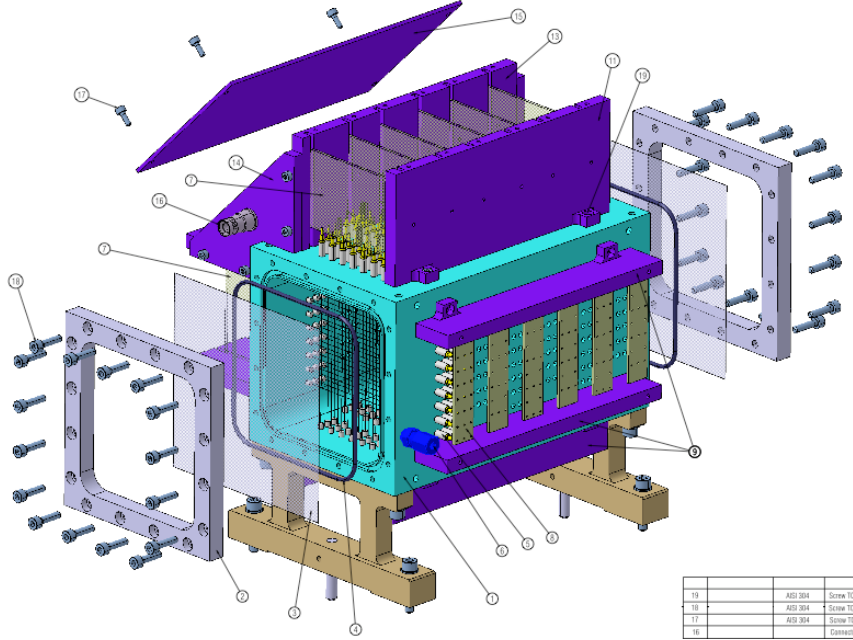


Figure 14 – Technical drawing of the BM drift chamber.

636 The four tracking layers of the vertex tracker will use as sensing element the M28 chip imple-
 637 mented by the Strasbourg CNRS PICSEL group [39] as the final sensor for the upgrade of the
 638 vertex detector inner layer of the STAR experiment [40, 41]. The M28 chip is from the family of
 639 the CMOS Monolithic Active Pixel Sensors (MAPS) that are widely used in optical imaging, X-ray
 640 imaging and charged particle detection for experiments in particle and heavy-ion physics.

641 The architecture of the MIMOSA28 integrates a fast binary readout and a zero suppression
 642 logic to reduce the amount of data produced. The sensor consists of a matrix composed by 928
 643 (rows) x 960 (columns) pixels of $20.7 \mu\text{m}$ pitch for a size of the chip of $20.22 \text{ mm} \times 22.71 \text{ mm}$ and is
 644 implemented in the Austria Micro System AMS-C35B4/OPTO design process that uses 4 metal-
 645 and 2 poly- layers. The thickness of the epitaxial layer is $15 \mu\text{m}$ on a high resistivity substrate of
 646 the order of $400 \Omega \cdot \text{cm}$.

647 The high hit rate of the STAR vertex detector of $2.4 \times 10^5 \text{ hits/s/cm}^2$ has driven the design
 648 of the sensor for a fast readout frequency in order to keep the track multiplicity per frame at a
 649 manageable level for the zero suppression logic implemented in the chip. Each pixel includes an
 650 amplification and a Correlated Double Sampling (CDS) circuitry. All the pixels CDS output of
 651 one row are readout in parallel row by row at the end of the column where 960 discriminators
 652 are placed, one per column. All the discriminators are arranged in four groups, each one with
 653 a different threshold level, programmable by the slow control, used to compensate process non
 654 uniformities along the entire sensing area. All four M28 sensors are thinned to $50 \mu\text{m}$, then the
 655 overall material budget for the entire Vertex tracker is $200 \mu\text{m}$.

656 In the left picture of Fig. 18 we see the system used for the FIRST experiment equipped with
 657 two M26 MIMOSA sensor planes (the two printed circuit boards behind the squared aluminum
 658 cover). Those boards will be replaced in the FOOT apparatus with four new boards completely
 659 redesigned on purpose to host a M28 MIMOSA sensor each. A M28 sensor is shown in Fig. 19.

660 The sensors in the stack will be arranged in such a way to form different gaps. The stack
 661 will consist of two sub-stations with two sensors each. Within the same sub-station the sensors will
 662 be placed at a relative distance of 2 mm to each other, while the two sub-stations will be separated
 663 by about 10 mm due to the size of the electronic components on the readout boards.

664 M28 sensors have been already used in different activities. As an example we report the results

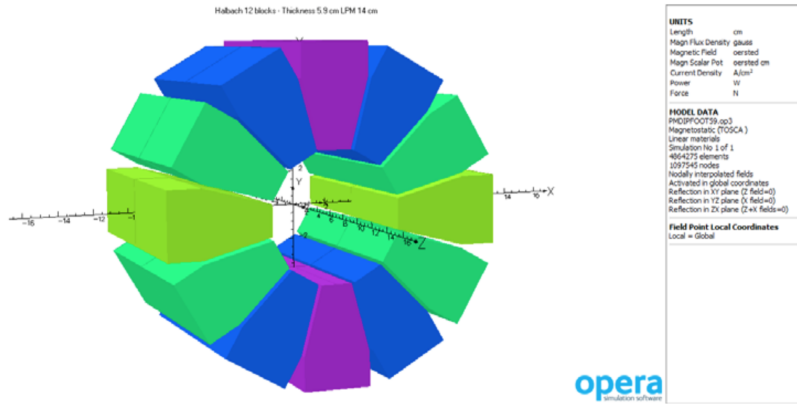


Figure 15 – Typical Halbach configuration with 12 single magnetic material pieces

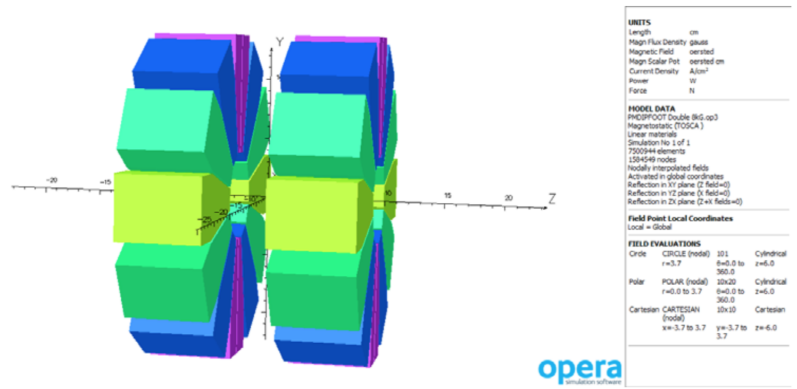


Figure 16 – Double magnet design

recently produced at the BTF (Beam Test Facility) at INFN Frascati laboratory. Two sensors at a distance of about 11 mm were put orthogonal to the beam axis. The beam was operating at a repetition rate of 50 Hz and showed a multiplicity ranging from 1 to $15 \div 20$ particles per spill. The data were collected by a data acquisition system implemented with a System on Chip (SoCKit) board housing an Altera FPGA interfaced to the control and data signals of the chips. The System on Chip FPGA included an ARM dual-core Cortex-A9 running the data acquisition program that was connected to the outside world by a GigaBit Ethernet interface. In Fig. 20 we show the results: in the first two plots the beam profile in the two M28 sensors (axis in μm) and in the last one on the right the reconstructed angular divergence of the beam in milli-radians. Obtaining this result required to implement the software analysis code to do the cluster reconstruction, the alignment of the two sensor ant then the tracking to evaluate each single track deflection angle.

4.2.3. Inner Tracker

The FOOT Inner Tracking station foresees two planes of pixel sensors to measure both the position of the track in the plane orthogonal to the beam axis and the direction of the track itself. While the transverse displacements of the two sensing planes can be reconstructed from the data, their longitudinal distance requires a precise mechanics with a spacer, as it will be described in the following.

We will cover an area of about $8 \text{ cm} \times 8 \text{ cm}$ in between the two permanent magnets at the moment designed with an aperture of 5 cm and 9.2 cm in diameter respectively. Moreover, even though the residual magnetic field is not negligible in the inner tracker position (z coordinate equal

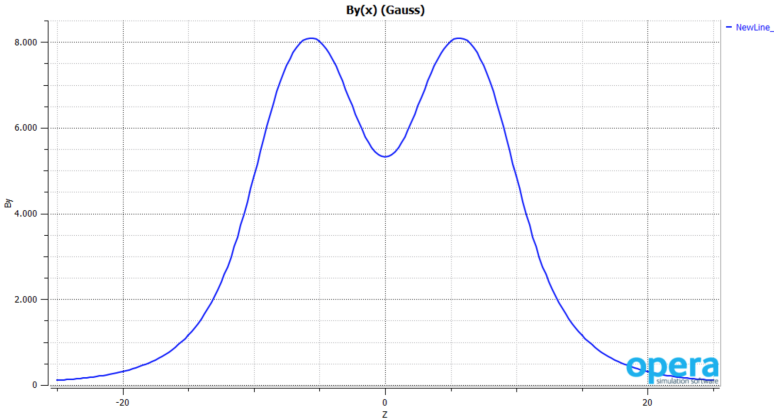


Figure 17 – Longitudinal magnetic field amplitude (Gauss) along the axis of the two magnets system

to zero in the plot of Fig. 17), sensor performances should not be significantly affected as reported in ref. [42]. We plan to use two planes of 16 M28 sensors, each sensor covering about $2 \times 2 \text{ cm}^2$. The use of the same technology of VTX will simplify the DAQ, the procurement of the sensors and the need for specific know-how. The main motivation for M28 sensors thinned to $50 \mu\text{m}$ is the minimization of the multiple scattering and nucleus re-fragmentation like in the Vertex. In this respect the performances will be slightly worse because the mechanical arrangement, due to the much larger area to cover, will introduce some more material to hold the sensors themselves and the support to fix the distances between the two planes. Moreover the material budget will also increase due to the need to cover the dead (not sensing) area of the sensors, especially at the bottom where the readout logic is placed, superimposing two ladders in those areas as described later in the overall Inner Tracker geometry description.

Our proposal is to implement a structure composed by ladders similar to the ones implemented in the PLUME project [43] in Fig. 21. In PLUME, a project started at IPHC Strasbourg in collaboration with the University of Bristol and DESY in Hamburg, a ladder is composed by two modules housing six M26 MIMOSA pixel sensors each to implement a double plane tracker.

Our arrangement foresees four M28 sensors in each module. Each ladder will see two modules face to face, and four ladders will be placed on a metallic frame to hold the entire tracker as in the arrangement schematically shown in Fig. 22. We have four ladders: two placed on the front side of the metallic support frame (gray color in the scheme) and two on the opposite side.

A single module is based on four sensors glued and bonded on a FPC (Flexible Printed Cable) made of Kapton having two or three conductive planes and an overall thickness of the order of $100 \mu\text{m}$. The distance between two consecutive sensors in the module can be limited to about 30 μm , as achieved in the PLUME project, to minimize the horizontal dead area. The top side of the sensor will be aligned with the FPC border, while on the bottom one the FPC will stand few millimeters out of the sensor to allow enough room for the bonding pads. The Kapton cable will have one or two SMD low insertion force connectors to manage the power supply and control the data signals from and to the sensors. The use of one or two connector will be decided according to the constraints of the final design, placing them on both ends of the FPC. This was not the case in the PLUME project due to specific requirements in the monitoring of the beam background for the Belle II experiment.

At the end of the sensors rows the support Kapton cable will exceed the sensor size. Those two "tails" on one side, the left one in the Fig. 22 will have two "ears" to fix the ladder to the metallic support structure, on the right side the tail is longer with four "ears" again to hold the system and to accommodate the connector/connectors for the sensors control. A 2 mm thick plate made of a special SiC foam with very low density, as in the PLUME project of ref. [44] will act as a spacer

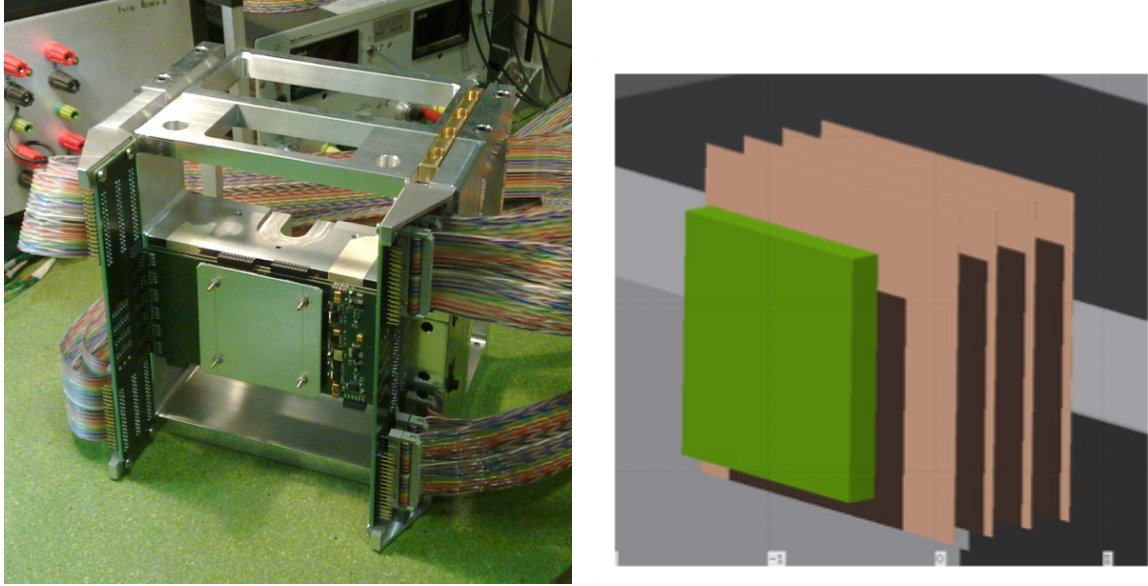


Figure 18 – Target and vertex tracker geometrical scheme

720 to define the distance between of the two planes. Two modules will be glued on the spacer. The
 721 dead area due to the readout electronics will superimpose, while horizontally the sensor will be
 722 shifted by few hundreds of μm to avoid the overlap of the dead area between adjacent sensors. This
 723 assembly procedure requires to design and construct jig: we have identified the required know-how
 724 in an experienced Company [45].

725 On the right side of picture in Fig. 22 we see how the four modules are located in the global
 726 structure. Each module has two connectors, in red and green color, respectively on the front and
 727 back side of the ladder.

728 4.3. Downstream Tracking: the Microstrip Silicon Detector

729 Tracking of fragments downstream the magnetic volumes is essential for the measurement of
 730 momentum and is also fundamental to match the reconstructed tracks with the hits in the TOF
 731 scintillator and the calorimeter. Also the redundant measurement of dE/dx would be mandatory
 732 to improve the reliability of the experiment. The choice of a microstrip silicon detector has been
 733 dictated by the need to:

- 734 • work as close as possible to the last magnet;
- 735 • provide a sufficient spatial resolution ($<35 \mu\text{m}$) for at least 3 x-y points;
- 736 • minimize the amount of material to reduce the impact of multiple scattering and also to
 737 reduce secondary fragmentation effects;
- 738 • provide a precise dE/dx measurement for heavy ions up to the 200-700 MeV/u kinetic energy
 739 range;
- 740 • provide the capability for dE/dx measurements up to 1 GeV/u in order to extend the physics
 741 potential of the FOOT experiment in the astrophysical domain.

742 According to the 10° opening angle needed to cover ions with $Z>2$, the surface that ought to
 743 be covered right after the second magnet is $9\times 9 \text{ cm}^2$. Three x-y planes will be separated one to
 744 each other by a 2 cm gap along the beam direction, ensuring a compact measurement system. In
 745 order to reduce the amount of material needed for each measurement plane to $\sim 150 \mu\text{m}$, and to

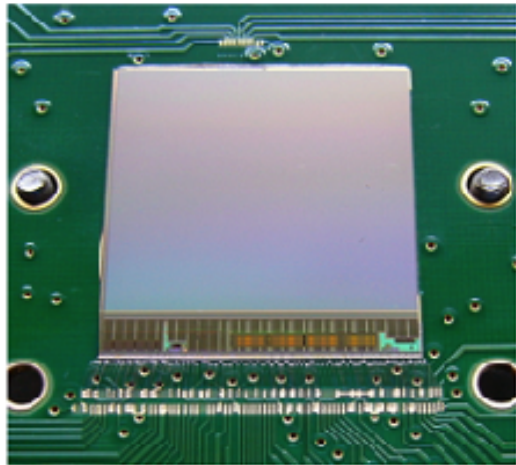


Figure 19 – M28 pixel sensor picture

746 ensure the x-y coordinate readout, a solution exploiting two silicon planes thinned down to $70 \mu\text{m}$
 747 each one and glued together using a $30 \mu\text{m}$ thick bi-adhesive Kapton foil will be used (Fig. 23),
 748 giving an equivalent silicon thickness of $\sim 155 \mu\text{m}$.

749 The two independent layers solution with respect to the one with a single $150 \mu\text{m}$ thick plane
 750 will ensure two independent dE/dx measurements and more rigid mechanical behavior. The front-
 751 end hybrids, hosting the readout chips, will be glued at one side of each silicon module minimizing
 752 the dead space in the beam region. To compensate for the smaller signal produced in the silicon,
 753 the on strip amplification mechanism guaranteed by the Low Gain Avalanche Diode mechanism
 754 (LGAD) [46, 47, 48] will be implemented, aiming at working with gain ~ 10 .

755 4.3.1. *LGAD amplification mechanism*

756 The Low Gain Avalanche Diode working principle lies in the Avalanche Photo Diodes, with a
 757 region with high electric fields ($>200 \text{ kV/cm}$) where the charge multiplication mechanism due to
 758 impact ionization takes place. LGAD are produced using a p-type multiplication layer, with an n⁺
 759 type electrode. Typical structure is shown in Fig. 24, with n⁺⁺ electrode, p⁺ multiplication layer,
 760 p⁻ substrate, p⁺⁺ electrode. The three components of the signal are due to electron and holes
 761 drifting from creation point to collecting electrodes, electrons due to multiplication traveling a short
 762 path to reach the n⁺⁺ electrode, holes due to multiplication process traveling the entire device
 763 thickness to reach the p⁺⁺ electrode. The most significant contribution is the last component [49].

764 The signal amplitude produced by a ^{90}Sr source has been measured as a function of the bias
 765 applied to the device, and the gain factor reaches easily a factor > 5 already with a polarization of
 766 60-70 V, while the noise remains essentially unchanged (Fig. 25). So this mechanism could be used
 767 to amplify the S/N figure when the detector thickness reduces, recovering signal amplitude. At $70 \mu\text{m}$
 768 thickness the expected MPV for Minimum Ionizing Particles is $\sim 49 \text{ e-h}/\mu\text{m}$ [50], for a total
 769 of $\sim 3450 \text{ e-h}$, to be compared with the 2000-3000 ENC as seen in Fig. 25. Given the minimum
 770 signal of 3 MIPs that should be expected by charged fragments in the energy range of the FOOT
 771 experiment, to recover an acceptable S/N ratio a gain factor > 5 would be sufficient. On the other
 772 hand the LGAD gain should be chosen in a way that, coupled with the front-end dynamic range,
 773 the measurement of deposited charge remains linear especially for the heavy fragments in all the
 774 energy range. For example ^{16}O at 200 MeV/u will deposit $\sim 3.7 \text{ MeV}$ energy in $70 \mu\text{m}$ thick silicon
 775 layer, corresponding to $\sim 10^6 \text{ e-h}$ and an amplification of 5 would mean 0.5 pC, and this should

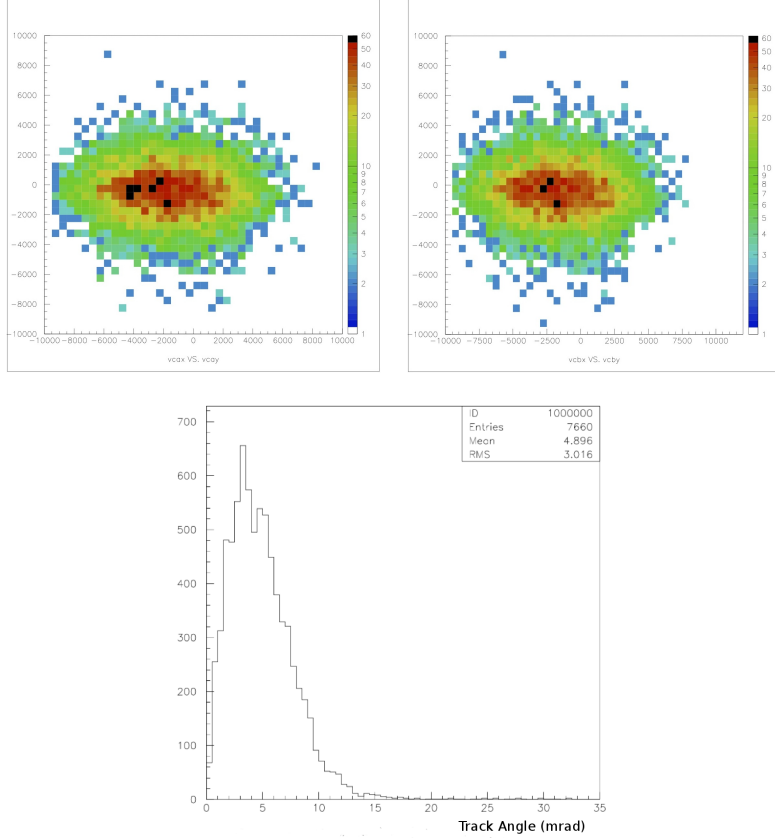


Figure 20 – Beam profile in the two M28 sensors (Upper left and right panel; units on both axes are in μm). Bottom panel: reconstructed angular divergence of the beam in milliradians.

776 be taken into account when choosing the readout chip.

777 It should be mentioned that if higher energy fragments would be studied, that would imply a
 778 smaller amount of energy released in the same silicon layers, hence the tailoring for 200 MeV/u
 779 energies does not prevent the same detector to be used to identify heavy ions in a range of energies
 780 of astrophysics interest.

781 A scientific collaboration with N. Cartiglia research group (Torino) has been already established
 782 to proceed in a focused R&D effort to study the behavior of thinned silicon sensors with LGAD
 783 amplification mechanism when traversed by heavy fragments. Up to now the prototypes with
 784 LGAD mechanism have been produced by FBK (Trento).

785 4.3.2. Spatial resolution, strip pitch and multi-track separation

786 To obtain a spatial resolution better than $35 \mu\text{m}$ keeping low the number of electronic readout
 787 channels it is mandatory to use an analogue readout. A strip pitch of $125 \mu\text{m}$ if read out digitally
 788 is enough to give the required spatial resolution, but with analog readout a further factor 3 could
 789 be easily gained [51, 52].

790 With this choice, an estimation of the number of strips, and hence of electronic readout channels
 791 could be derived; given no dead space, maximum number of strips in 9 cm is 720, so in total each x-y
 792 plane will have 2×720 channels, and in total $3 \times 2 \times 720 = 4320$ channels will be needed. An important
 793 issue to be evaluated is the capability of multi-track resolution for the various ion species at different
 794 energies. Two components are necessary: cluster size for each ion species and track multiplicity on
 795 event by event basis at the exit of the magnetic volume. The cluster multiplicity, given the $70 \mu\text{m}$
 796 thickness and the $125 \mu\text{m}$ pitch is usually confined to few strips for MIPs or relativistic ions [53].



Figure 21 – Picture of a PLUME ladder

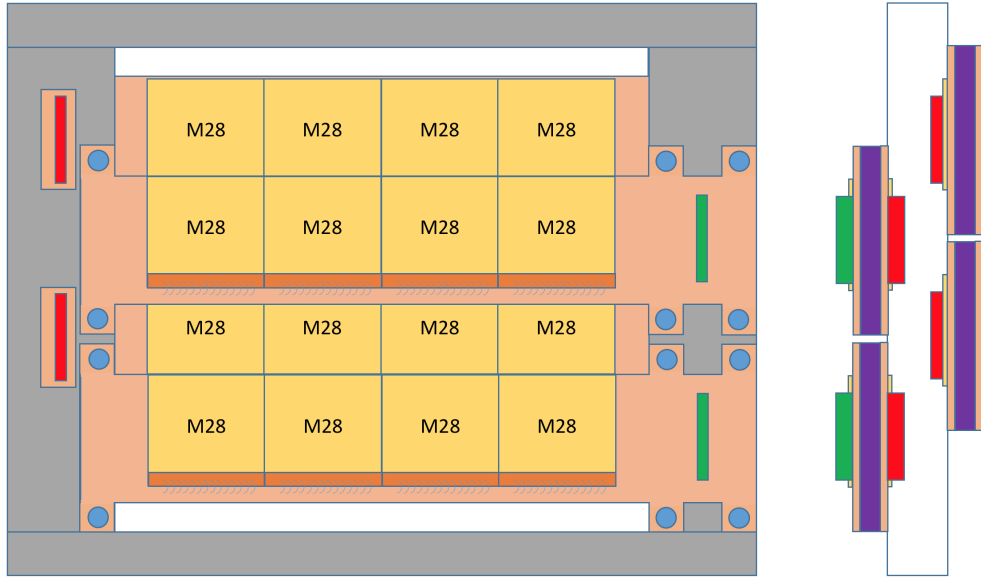


Figure 22 – Inner tracker scheme

797 The second factor has been studied from the distribution of closest distance among hits belonging
 798 to the same event (Fig. 26). The probability of two hits to have superimposing clusters is hence
 799 negligible.

800 4.3.3. *dE/dx measurements*

801 Using silicon layers dE/dx measurement of single ions will be possible with high level precision.
 802 This has already been proved by the AMS collaboration during construction phase of silicon mi-
 803 crostrip detector [53, 54], equipped with an earlier version of the same readout electronic that will
 804 be used for FOOT MSD. Main results are the ion identification with less than 10% confusion for
 805 all species up to the carbon (Fig. 27 (a) and (b)), and less than 0.1% when two informations are
 806 combined (Fig. 27 (c)). Comparing the $350 \mu\text{m}$ thickness of a single AMS layer with the total 420
 807 μm of MSD and taking into account the 6 independent measurements, we could expect, without
 808 LGAD mechanism, similar or better performances with respect to the AMS layer. The goal would
 809 be to obtain a superposition for all the adjacent pairs of ions $< 5\%$.

810 A FLUKA2 simulation of energy deposition in $70\text{m } \mu\text{m}$ thick silicon from ions at both 200
 811 MeV/u and 700 MeV/u has been carried out and the results are shown in Fig. 28 (left). The peaks
 812 are separated at 20% level for a single layer measurement without using the LGAD amplification
 813 mechanism. Summing up two layers, the simulations shows a separation that is roughly halved

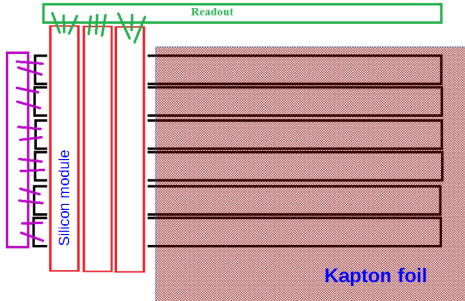


Figure 23 – Conceptual sketch of x-y plane: x and y 70 μm modules glued to a 30 μm biadhesive kapton foil. Electronic front-end is at the periphery of the modules.

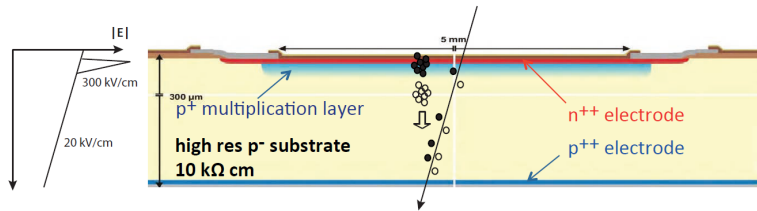


Figure 24 – LGAD concept: $n^{++}/p^{+}/p^{-}/p^{++}$ doping structure. Main signal contribution due to holes moving toward p^{++} electrode.

814 (~ 10%), and with 3 x-y planes (6 independent measurements), another factor 3 should be possible,
815 bringing down the superposition to ~ 3%.

816 The presence of LGAD devices will allow, using the gain handle, to increase the S/N to use at
817 its maximum the dynamic range of the readout electronics, as the beam energy would change.

818 This will be fundamental to measure the dE/dx for the energies of interest of the astrophysical
819 sector. Looking for example at Fig. 28 (right), at 700 MeV/u the superposition among adjacent
820 ions is increased to ~ 40%. Using the gain guaranteed by LGAD devices, a factor 5 would help in
821 separating the ion species and in recovering at least partially the small superposition obtainable
822 with lower ion energies.

823 4.3.4. Module production, thinning and mechanical issues

824 It has already been proved that 9x9 cm^2 strip modules could be produced in one single piece
825 during the construction of the GLAST/FERMI experiment, resulting in almost no dead space [55]
826 (Fig. 29 left). Also rectangular modules 10x1.3 cm^2 thinned down to 50 μm have already been
827 produced, mainly in the framework of the ILC programme [56] and tested for performances with
828 Minimum Ionizing Particles (Fig. 29 right).

829 Thinning of silicon substrates during production flow is a standard practice in IC production
830 that could be done in a variety of methods at the wafer level: mechanical grinding, chemical me-
831 chanical polishing (CMP), wet etching and atmospheric downstream plasma (ADP), dry chemical
832 etching (DCE). The preferred method for very thin devices usually is the deep anisotropic etching,
833 that leaves a ring of thick substrate at the periphery of the thinned region. It is possible then
834 to etch most of a wafer leaving just the peripheric region thicker, so it will be possible to obtain
835 modules long enough for the MSD construction. LGAD test structures, thinned down to 50 μm
836 and optimized for triggering purposes, have already been produced and tested [57, 58]. FBK is
837 currently producing a further batch of test structures for this application that will be also tested
838 for MSD purposes in the framework of the collaboration with N. Cartiglia research group. In the
839 past silicon microstrip modules 150 μm thick have already been produced and have demonstrated

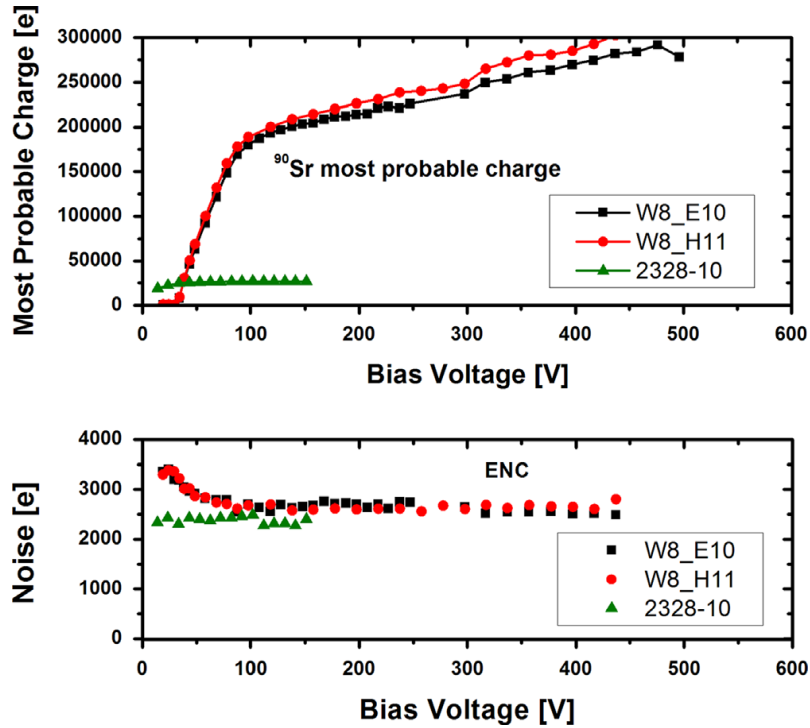


Figure 25 – Two amplified (W8-E10 black squares and W8-H11 red dots) and one non-amplified (2328-10, green triangles) sensors irradiated with ^{90}Sr source: signal (upper plot) and noise (lower plot) as a function of bias [48].

840 to be mechanically stable. The $70 + 30 + 70 \mu\text{m}$ solution, with crossed modules should be at least
 841 as stable as the latter one.

842 Each plane will then be glued to a carbon fiber frame, to be fixed to an aluminum/steel structure
 843 connected with high precision to the overall mechanical structure of the experiment.

844 4.3.5. Readout channels and readout chain

845 The DAQ chain will use the already developed DAMPE components [59] namely:

- 846 • The Tracker Front-end Hybrid (TFH) (Fig. 30). This hybrid will host the VA140 ASIC, a
 847 64 channel charge sensitive preamplifier-shaper, low noise, high dynamic range ($\pm 200 \text{ fC}$)
 848 designed by IDEAS Inc. (Norway) [60, 61]. Each hybrid will serve one 1.5 cm module with
 849 120 strips, hence two VA140 chips will be needed on the hybrid, plus the control lines and
 850 the common output amplifier. The power source VSS/VDD for the readout electronics and
 851 HV bias (80V) for silicon strip module in the TFH are supplied through the connector by
 852 the Tracker Readout Board (TRB).
- 853 • The Tracker Readout Board (TRB) (Fig. 31). Each plane will be equipped with one of
 854 these boards. They are responsible for the detector readout and data process for their front
 855 connected TFHs. Each TRB module consists of 3 electronics boards: power board, control
 856 board and SADC board. These boards are already existing and the schematics could be
 857 used for the FOOT MSD. The customization part will mainly concern the reduced number
 858 of TFHs to be connected to each board (6 in the current version).

859 4.4. ΔE and TOF Detector

860 This detector will provide the stop to the TOF measurement and the measurement of the energy
 861 release ΔE in a thin slab of plastic scintillator to identify the charge of the crossing fragment. The

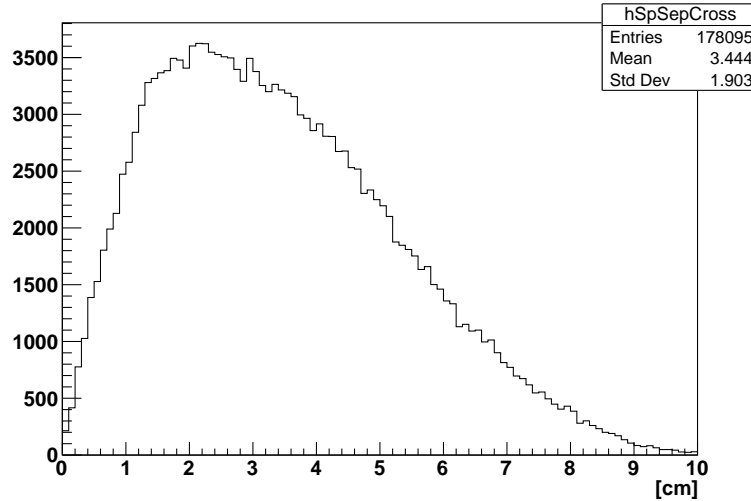


Figure 26 – Distribution of closest distances between hits at the exit of the magnetic volume.

862 dE/dx measurement should achieve accuracy of the order of 2-3% while a 70 ps time resolution
 863 should be achieved on the heavy fragments (C,O) at 200 MeV/u, to fulfill the 100 ps requirements
 864 on TOF resolution.

865 This detector is made of two orthogonal layers of 20 plastic scintillator rods, each one 3 mm
 866 thick, 2 cm large and 40 cm long. The $40 \times 40 \text{ cm}^2$ size matches the fragments aperture at 1 m
 867 distance form the target. The 2 cm granularity matches the $2 \times 2 \text{ cm}^2$ transverse surface of the
 868 calorimeter units and is enough to keep the occurrence of double fragments in the same rod below
 869 the % level. The thickness chosen is a trade off between two opposite trends: a thicker rod will
 870 integrate more energy release and more emitted light, so improving the resolution on both ΔE
 871 and TOF, but on the other hand a re-fragmentation inside the thicker plastic rod would spoil the
 872 dE/dx measurement.

873 A similar setup has been already used for the charge identification of relativistic ions for space
 874 mission [62] . In that reference the scintillator rod had a larger thickness, 1 cm instead of the 6
 875 mm of a double FOOT layer. If we assume that the energy resolution is limited by the light yield,
 876 such a difference is more than compensated by the lower energy release of relativistic fragments
 877 with respect to the target fragmentation case ($\beta \simeq 0.6$). On the contrary, if the limit is given by
 878 the Landau fluctuation a maximum worsening of $\sqrt{\frac{1}{0.6}}$ is expected. Fig. 32 shows the separation
 879 power of such a technique, perfectly adequate for our purposes.

880 4.4.1. The $\Delta E/TOF$ prototype

881 The dE/dx detector prototype we are currently testing is composed by two layers of plastic
 882 scintillator bars coupled at both ends to silicon photomultipliers (SiPM) via optical glue (Saint-
 883 Gobain, BC-630). A picture of a single bar is shown in Fig. 33. The two layers are arranged
 884 orthogonally to identify the two-dimensional interaction position of the particle in the detector.
 885 The spatial resolution in the two directions is given by the bar section, *i.e.* 20 mm, which matches
 886 the calorimeter pixel size. A check of the interaction position is given by the difference in amplitude
 887 of the signal collected at the two ends of each bar. Each layer provides time and energy information
 888 which can be combined to improve the precision of the time-of-flight and dE/dx determination.

889 The detector bar is made of polystyrene and it is 440 mm long and 20 mm large. When the
 890 bar thickness increases, the time resolution improves, while the fragmentation probability inside
 891 the detector increases. Therefore different thickness values are being investigated to determine the
 892 best compromise.

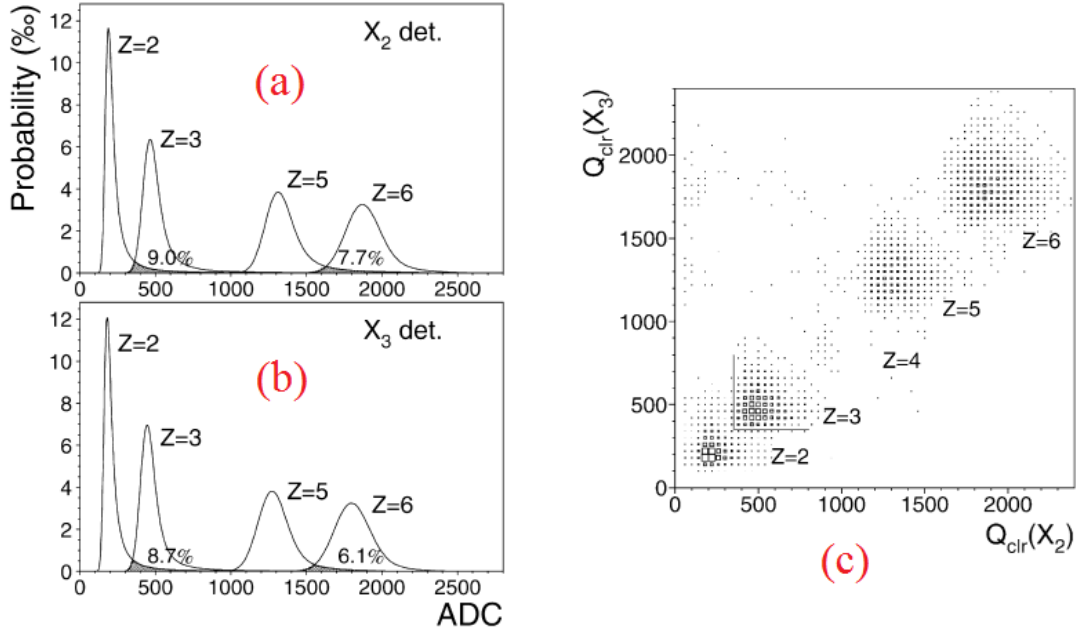


Figure 27 – Different ion species identification capability of AMS tracker for two silicon layers. (a) and (b) Normalized cluster charge distributions and percentage of overlaps; (c) Correlation of cluster charge measured by both silicon layers.

Table 1 – Properties of the plastic scintillator employed in the dE/dx detector [63].

Base material	Polystyrene
Density (g/cm ³)	1.05
Max emission wavelength (nm)	415
Rise time (ns)	0.9
Primary decay time (ns)	2.40
Light output (%relative to Anthracene)	50-60
H/C ratio	1.10
Refractive index	1.58
Reflector and light shielding sheet	Aluminum foil and black vinyl

The four sides of the bars are wrapped with a reflecting Aluminum foil to guide light to the photodetectors and covered with black vinyl for light-tightness. The ends coupled to the photodetectors are polished. The properties of a suitable plastic scintillator material [63] are summarized in Table 1. The scintillator bar is read-out at both ends via silicon photo-multipliers (ASD-NUV SiPMs, produced by AdvanSiD for the detection of near ultraviolet-light [64]). The SiPMs have 3 mm × 3 mm active area and 40 μm side micro-cells, with 60% fill-factor. The typical dark count rate is less than 100 cps/mm², and the maximum photon detection efficiency is 43% at 420 nm. For the 3 mm × 3 mm SiPM, the single photon time resolution reported in ref. [65] is 180 ps FWHM. The number of photo-detectors coupled to each end will be optimized according to the expected performances of the final detector. In fact, SiPMs can be connected in series to cover a larger fraction of the scintillating bar, thus increasing the fraction of collected light, without compromising the time performance of the photo-detector (*i.e.* without increasing the total capacitance nor degrading the rising edge of the SiPM).

4.4.2. Data acquisition

The SiPM signal is amplified and sent to a fast-digitizer, which can sample the signal at a maximum rate of 5.12 GSamples/s with a dynamic range of 1 V, adjustable according to the po-

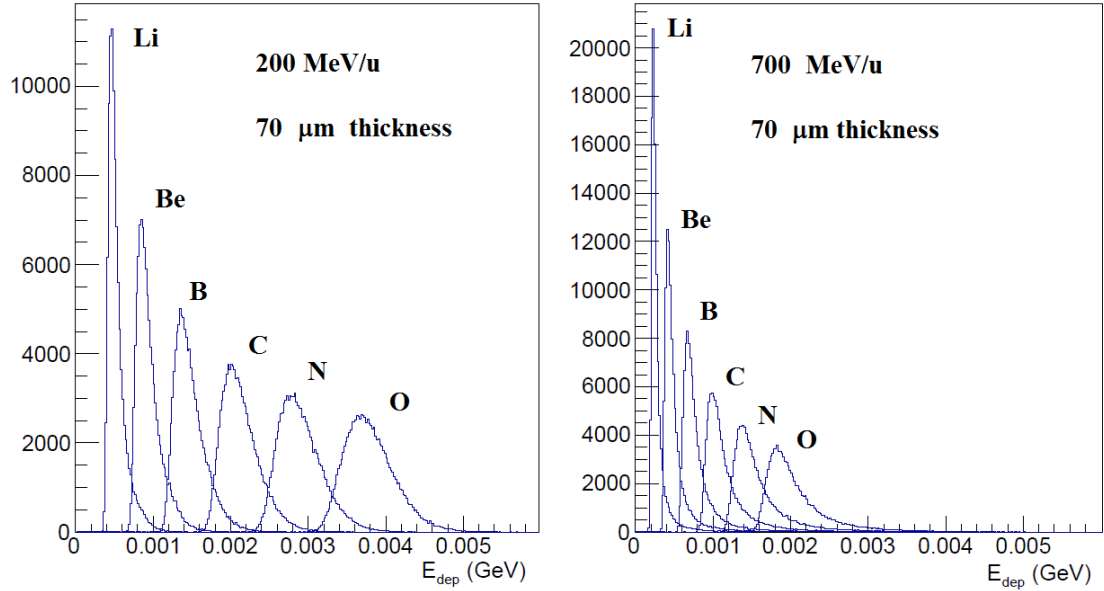


Figure 28 – Energy deposition of ions with different Z (from 3 to 8) in 70 μm thick silicon: 200 MeV/u (left), 700 MeV/u (right).

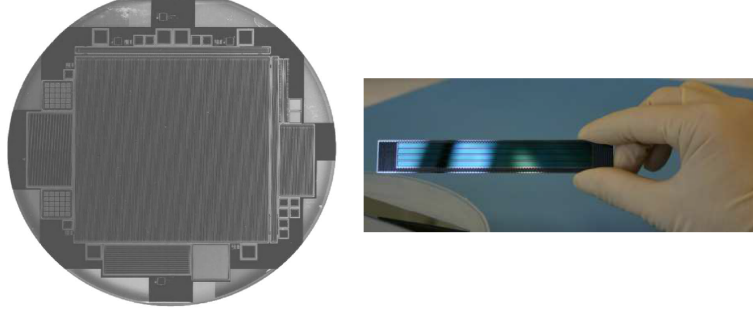


Figure 29 – Left: wafer with 9x9 cm² strip module for GLAST/FERMI [55]. Right: 10x1.3 cm² ILC module thinned to 50 μm [56].

909 larity of the detector output signal. The data acquisition, called WaveDAQ, is based on the DRS
 910 ASIC [66] developed at the Paul Scherrer Institute (PSI) and on the MEG DAQ [67] designed
 911 in collaboration by PSI and INFN. It is an innovative and highly flexible device with integrated
 912 complex trigger functionalities. Detector signals are connected to a custom board called Wave-
 913 DREAM (WDB) which provides 16 channels with variable gain amplification and flexible shaping
 914 through a programmable pole-zero cancellation. Switchable gain-10 amplifiers and programmable
 915 attenuators allow an overall input gain from 0.5 to 100. If needed, the WDB can also supply SiPMs
 916 thanks to an on-board power supply. The input signals are digitised by both the DRS and ADC (80MHz - 12bit) whose stream is received and used by an FPGA to perform some online
 917 reconstruction which is eventually finalised by higher level trigger board connected by means of
 918 Gb serial links.
 919

920 Contributions to the time measurements come from the DRS chip time calibration and the
 921 reference clock distribution jitter between the different digitizers. This has been measured to be
 922 ≈ 10 ps, well below the experimental requests. The baseline fluctuation has been measured to be
 923 from 1 mV to 5 mV depending on the configuration.



Figure 30 – DAMPE Tracker Front-end Hybrid (TFH) block diagram, modified for MSD.

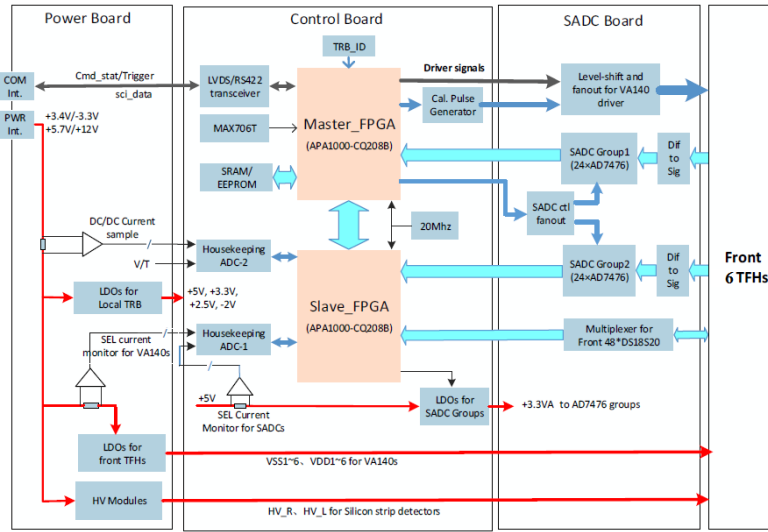


Figure 31 – DAMPE Tracker Readout Board (TRB) block diagram.

924 4.4.3. Expected performances and preliminary results

925 A preliminary test beam was performed at the Proton Therapy Centre (PTC) of the Trento
 926 Hospital (Trento, Italy) to measure the time and energy resolution of the dE/dx detector prototype.
 927 A picture of the setup used for the test beam is shown in Fig. 34. A 200 mm×20 mm×2 mm bar
 928 was coupled at each end to two SiPM arrays connected in series. Scans over the beam position,
 929 the beam energy and the SiPM over-voltage were performed, using protons as primary particles.
 930 The settings are summarized in Table 2. The beam position is relative to the bar center, according
 931 to Fig. 34.

932 *Energy resolution.* The distribution of the energy collected at the two bar ends is the convolution
 933 of the energy released by the particle in the scintillator (following a Landau distribution) and the
 934 detector response (distributed as a Gaussian). The mean and the full width at half maximum of the
 935 measured energy distribution (μ , $FWHM$)_{E,exp} were calculated from the experimental data, for
 936 each of the two SiPM groups. The distribution of the energy released in the bar was estimated with
 937 a Geant4 Monte Carlo simulation, and the mean and full width at half maximum were calculated

Table 2 – Summary of preliminary dE/dx detector performance tests with proton beams. Beam positions are with respect to the center of the bar. The fast digitizer sampling rate was 5 GSample/s.

Scan	Beam position	Beam energy	SiPM over-voltage	Time resolution
Beam position	[-7,+7], 0.5 cm steps	110 MeV	5 V	with STS1
Beam energy	0 cm	70-230 MeV	5 V	with STS1
SiPM over-voltage	0 cm	140 MeV	2-7, 1 V steps	with μ (STS1,STS2)

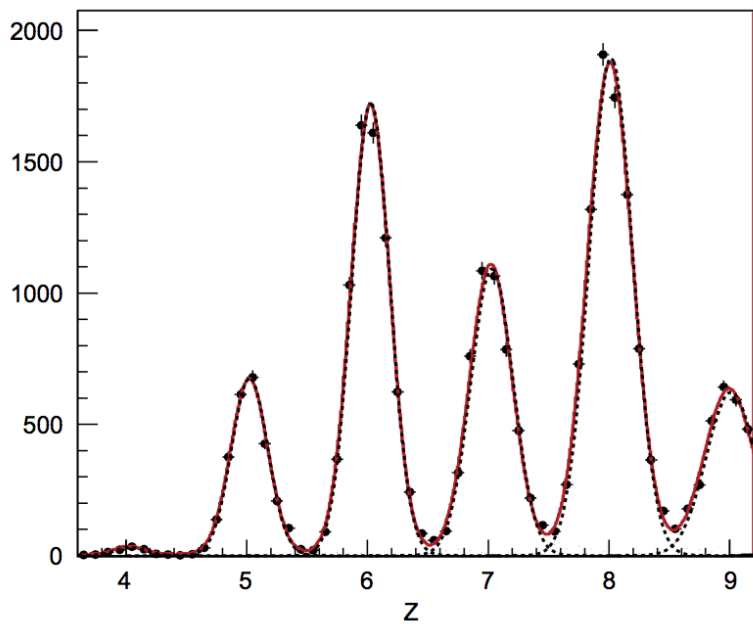


Figure 32 – Charge distributions from the scintillator for Be, B, C, N, O, from [62].

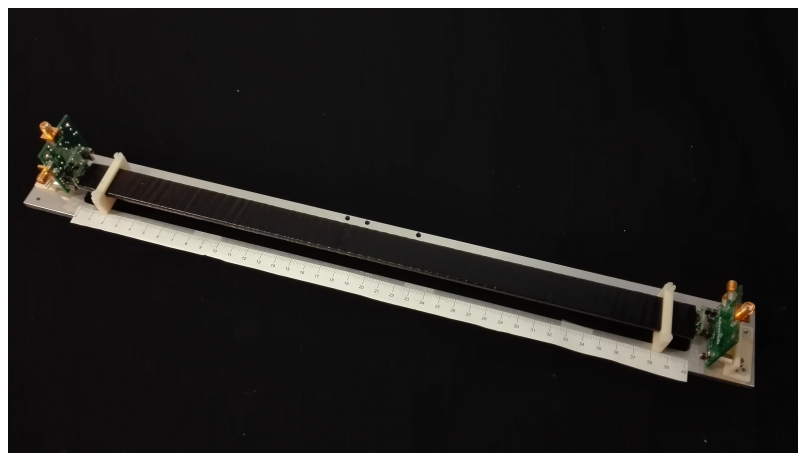


Figure 33 – Picture of the dE/dx detector prototype.

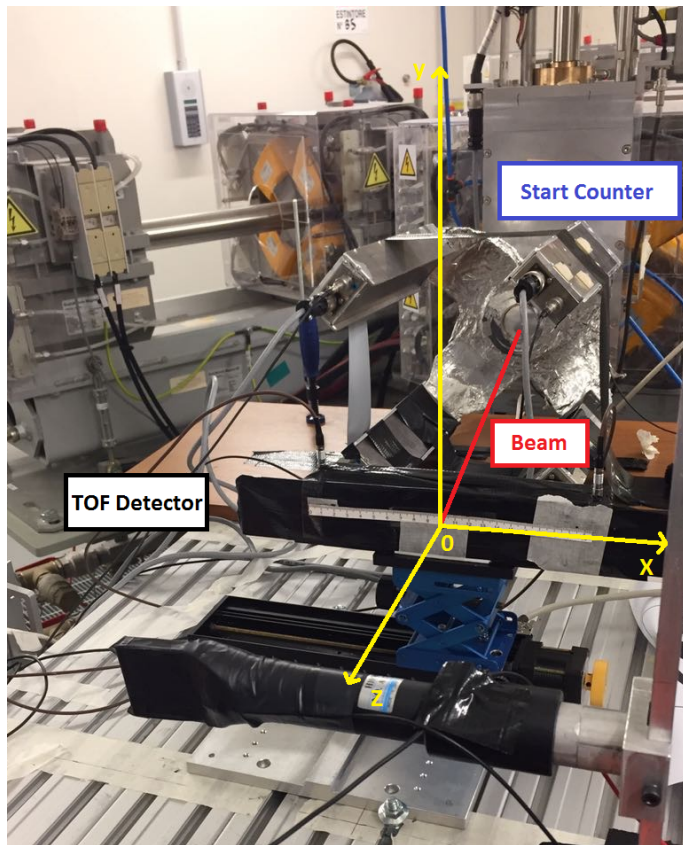


Figure 34 – Picture of the setup used for the preliminary test beam: the beam enters the Margherita start counter, then the TOF detector, followed by the trigger counters (denominated STS 1 and STS 2) and finally by the dose profiler.

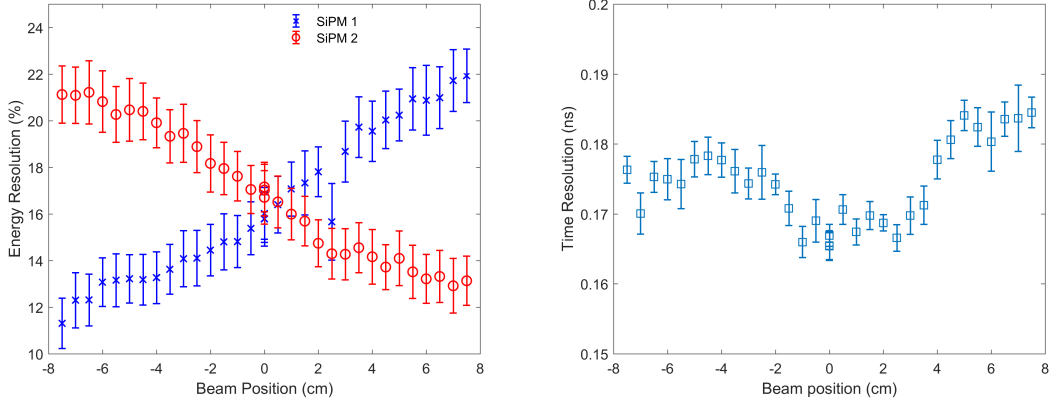


Figure 35 – Energy resolution at the two ends of the dE/dx detector bar (left) and time resolution with the STS1 channel (right).

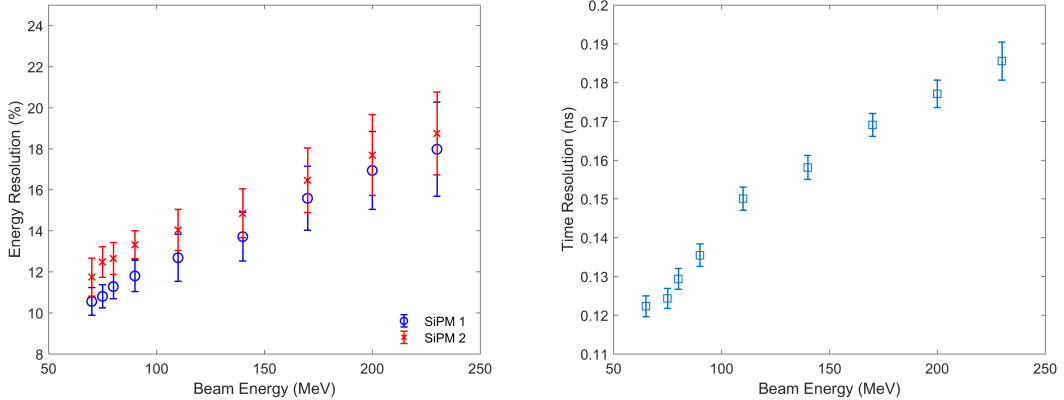


Figure 36 – Energy resolution at the two ends of the dE/dx detector bar (left) and time resolution with the STS1 channel (right), for different values of the proton kinetic energy.

938 $(\mu, FWHM)_{E,sim}$. The detector resolution was then calculated as

$$\left(\frac{\sigma}{\mu}\right)_{E, det} = \frac{1}{2.35} \sqrt{\left(\frac{FWHM}{\mu}\right)_{E, exp}^2 - \left(\frac{FWHM}{\mu}\right)_{E, sim}^2} \quad (3)$$

939 **Time resolution.** The mean of the arrival time of the scintillation photons at the two bar ends
940 was calculated for each event. The difference of these values and a reference timestamp was then
941 calculated, using as the reference timestamp one of the trigger scintillation counters (STS) or the
942 mean of the timestamps measured by the two STSs. The time resolution was determined as the
943 standard deviation of this difference, following a Gaussian distribution.

944 The energy resolution and the time resolution (obtained with the STS1 trigger scheme) are
945 shown in Fig. 35 as a function of the beam interaction position. The energy resolution ranges from
946 10 to 25%, while a time resolution of 170–180 ns was measured.

947 The energy resolution and the time resolution (with the STS1 channel) are shown in Fig. 36
948 as a function of the beam energy. The fact that the energy resolution is slightly higher at one end
949 of the bar is due to differences in the SiPMs breakdown voltage and to uncertainties in the beam
950 positioning.

951 The energy resolution and the time resolution (with the mean STS information) are shown in

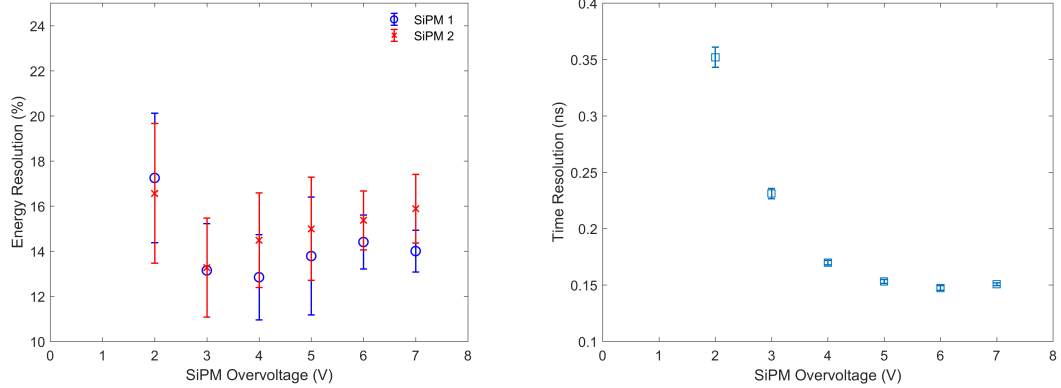


Figure 37 – Energy resolution at the two ends of the dE/dx detector bar (left) and time resolution with the mean of the STS signals (right), for different SiPM over-voltage values.

Fig. 37 as a function of the SiPM over-voltage. As expected, resolutions worsen for increasing energy.

4.5. Calorimeter

The FOOT calorimeter is the most downstream detector. It is designed to measure the energy of projectile fragments produced in the target. The upper bound of the fragments energy range is defined by the beam energy, while the lower bound is set by the intensity of the magnetic field.

FOOT will operate in a range in which fragments are below the energy threshold that triggers a shower in a calorimeter. Therefore, the mechanisms for energy loss will be driven by the electromagnetic interaction and nuclear interactions: the production of neutrons escaping the calorimeter undetected produces a systematic underestimation of the initial energy.

Since FOOT will work at a relatively low beam intensity, the ideal material for a calorimeter is a dense crystal, with high light yield, without strict requirements of the response speed. BGO is then a natural solution, also because it would open the opportunity to reuse crystals in past experiments. The typical transverse size of BGO crystals used for EM calorimeters corresponds approximately to the Molière radius, *i.e.* 2.2 cm. On the other hand, the thickness could vary, depending on the statistical and systematic requirements on the energy resolution.

4.5.1. Preliminary test

An early test with BGO crystals was already run with proton beams in the 125-228 MeV range. The layout, shown in Fig. 38, makes use of two plastic scintillators 1 cm thick (EL-208 read out by Hamamatsu 8024 PMT), that in coincidence provide the trigger signal. Then a 7 cm thick BGO crystal follows, read out by a H6524 Hamamatsu PMT.

The time difference between the STS2 trigger scintillator and the BGO shows a resolution ranging between 230-300 ps, slightly increasing with the proton energy. Due to the very good time performance of the plastic scintillator this fluctuation is entirely due to the BGO crystal.

The measured energy, shown in Fig. 39 for 228 MeV protons, demonstrates that the resolution is remarkably good: $\Delta E/E \sim 2\%$, which meets the requirements. Should be stressed that this value should be considered as an upper value since for the fragment of interest ($3 \leq Z \leq 8$ and $200\text{MeV}/u \leq E_{kin} \leq 400\text{MeV}/u$) the contribution to the resolution of the statistical term will become negligible. However, a long tail corresponds to events in which nuclear interactions generate neutrons escaping the BGO crystal without interacting. This effect causes a systematic underestimation for a not negligible fraction of events to be minimized in the design of the final layout. A little part of this tail, *i.e.* the one nearby the peak, can be associated to neutrons escaping the BGO crystal laterally and entering adjacent BGO crystals. A fraction of them will

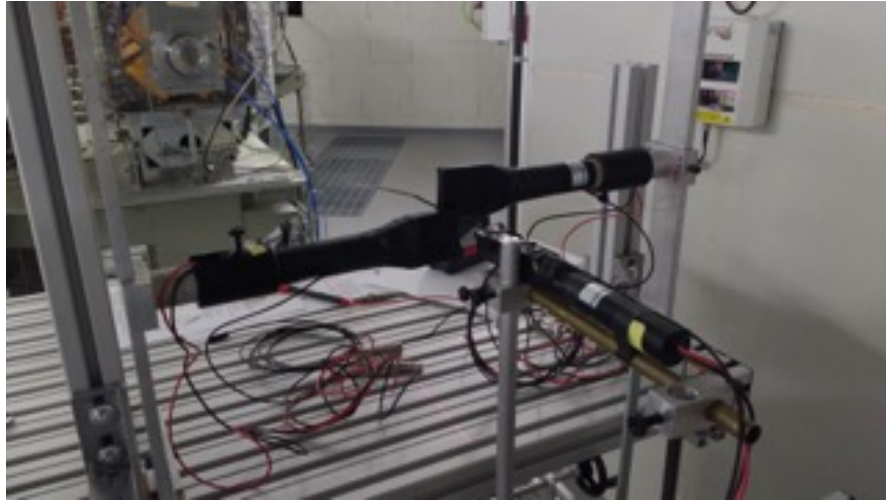


Figure 38 – Layout for the BGO test with proton beams.

985 re-interact and, thanks to the time measurement and the identification of the primary by the TOF
 986 detector in front of the calorimeter, will reduce the systematic effect.

987 On the other hand this effect is expected to be more pronounced for light projectiles, so the
 988 heavy fragments show a better behavior with respect to this tail as shown in Fig. 68.

989 Secondary neutrons that travel forward carry the largest fraction of the initial proton energy. An
 990 increase of the BGO crystal thickness would increase the probability of re-interaction of neutrons.
 991 The effect can be simulated, but an experimental test with 21 cm long BGO crystals is also foreseen.

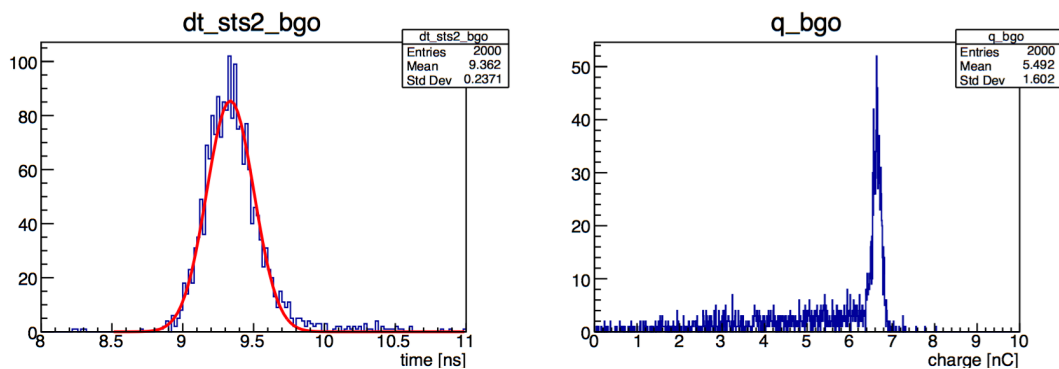


Figure 39 – Time and energy response of the BGO crystal.

992 The linearity of the energy measurement was also measured: the results reported in Fig. 40
 993 show that the slope decreases when increasing the beam energy. Since light ion fragments will
 994 reach energies up to a few GeV, the energy response linearity will have to be assessed over the full
 995 expected range, and will be the ultimate limit to the energy resolution.

996 4.5.2. Layout and planning

997 The calorimeter will cover a circular surface of about 20 cm radius, which corresponds to about
 998 350 BGO crystals with $2 \times 2 \text{ cm}^2$ transverse size. As shown in Fig. 11, in the case of a 200MeV/u
 999 Oxygen beam on a CH_2 target, this granularity will allow that only in $\simeq 1\%$ of events two fragments
 1000 hit the same crystals, if the calorimeter is 120cm away from the target. This number doubles with
 1001 the beam energy raised to 400MeV/u .

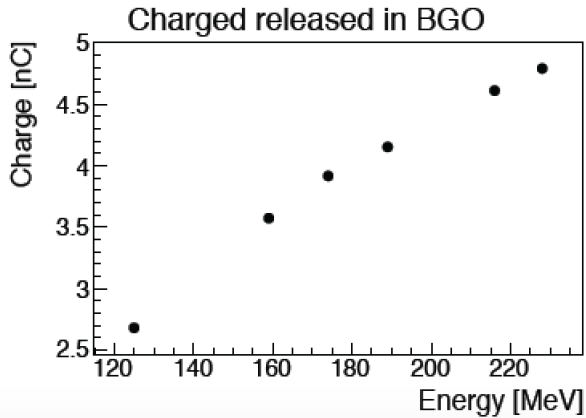


Figure 40 – Charge vs proton energy of the BGO crystal.

Depending on the effectiveness in recovering the energy leakage caused by neutrons, the transverse size could extend up to about 25 cm radius (*i.e.* about 500 crystals).

The crystal thickness is still an open parameter, which will range between 10 cm and 21 cm: the optimal value will be defined as a trade off between performance on one side, mechanical constraints and cost on the other.

Presently, two options are being evaluated for the BGO readout: PMTs and Silicon Photo-multipliers (SiPM). The choice of PMT is more conventional and it will guarantee the expected performance in terms of energy resolution and (to some extent) linearity. In particular in the baseline approach is foreseen the use of XP192, 19mm diameter PMT by HZC Photonics [68]. A cost effective solution for the Front End Electronics is to interface such a PMT with a waveform digitiser as the CAEN V1742, avoiding the standard splitter/delay/ADC/TDC scheme, as already adopted in the building of the BGO calorimeter of the PADME experiment [69, 70]. Such a readout solution has been proven to provide a resolution of the order of $\frac{2\%}{\sqrt{(E_k \text{ in } GeV)}} \oplus 1\%$ and a linearity of 2% up to 1 GeV as measured in ref [?]. The reported performances are very similar to the FOOT calorimeter requirements.

However, it is our intention to evaluate SiPMs as an alternative solution, as they would allow a more compact design. SiPMs should be carefully evaluated in terms of dynamic range: presently available designs, with 25 μm micro-cell pitch, might saturate with the high signals induced by light ion fragments.

In view of the evaluation of the future calorimeter features, a new prototype of 2x2 BGO crystals, 7 cm thick, is being assembled and will be tested and characterized during 2017 at HIT (Heidelberg, Germany), where carbon beams that cover the full expected energy range are available. The crystals will be readout with both PMTs and SiPMs, so as to compare the performance with the two possible options. The test will also include longer crystals (21 cm), to evaluate the impact of neutron leakage in the two configurations. Once a readout choice is made, the mechanics will be designed. The final calorimeter design will be ready by the end of 2017, in such a way to be able to place orders for the BGO crystals and the front-end electronics in early 2018.

1029 5. The Emulsion Spectrometer

1030 To characterize the production of low Z fragments, an emulsion spectrometer has been included
1031 in the FOOT setup as described in Sec. 3. In Fig. 41 the arrangement of the emulsion spectrometer
1032 (ES) inside the FOOT detector is shown: the ES will be placed behind the Start Counter and the
1033 Beam Monitor.

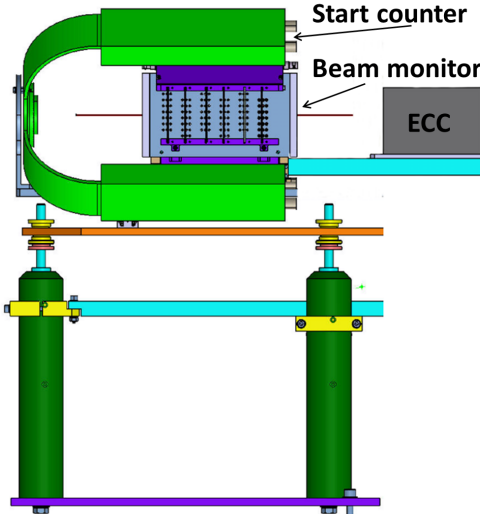


Figure 41 – Emulsion spectrometer setup inside the FOOT detector.

1034 Among all tracking devices used in particle physics, nuclear emulsion detectors achieve the
1035 highest spatial resolution (sub-micrometric) for tracking ionizing particles. Emulsions have a long
1036 history and contributed to outstanding achievements and discoveries in particle physics. After
1037 a natural decline with the advent of fast electronic detectors in the sixties, this technique has
1038 experienced a vigorous rebirth in the last twenty years thanks to the advances in high-speed
1039 automated scanning and the industrial production and handling of emulsions. Nowadays, they are
1040 still unsurpassed for the detection of short-lived particles and for specific applications in neutrino
1041 physics and other emerging fields [71].

1042 Emulsion chambers integrate target and detector in a very compact setup and provide a very
1043 accurate reconstruction of the interactions occurring inside the target. Moreover, no power supply
1044 or any readout electronics is required and this helps to keep the emulsion setup compact and
1045 without angular limitations. The use of emulsions is coupled to the achievements in the automated
1046 scanning system technique [72, 73, 74]. Last generation microscopes [75, 76, 77, 78] allow very fast
1047 scanning with wide angular acceptances (more than 70°) and real time analysis of huge data sets,
1048 about one order of magnitude faster than those used for the OPERA experiment [73, 74].

1049 The emulsion technique has been already exploited to study the fragmentation of Carbon ions
1050 in polycarbonate (Lexan). In the experiment, a detector made of nuclear emulsion films [82]
1051 alternated to lexan plates (to simulate the human tissue) has been exposed to a 400 MeV/u ^{12}C
1052 beam at the Heavy Ion Medical Accelerator (HIMAC) in Chiba (Japan) to identify the secondary
1053 nuclei produced by fragmentation [83, 84]. By analyzing the grain density along the particle
1054 track, the fragment charge could be assessed with a very high efficiency (above than 99%). The
1055 discrimination of Hydrogen, Helium, Lithium, Beryllium, Boron and Carbon can be achieved at
1056 least at two standard deviations, depending on the track length of the detected particles [83]. In a
1057 second step of the investigation, total charge-changing cross section was also obtained by analyzing
1058 the carbon interaction vertices and measuring the charge of all the fragments produced [84].

1059 Thanks to the huge progresses in the automated scanning system (large angle particles are
1060 detected above 70° with respect to the incident angle), emulsion detectors were adopted also in the

¹⁰⁶¹ framework of the FIRST (Fragmentation of Ions Relevant for Space and Therapy) experiment [6]
¹⁰⁶² to study fragments produced at large angles by 400 MeV/u ^{12}C ions impinging on a composite
¹⁰⁶³ target [85]. The kinematical properties of protons emitted with angles up to 80° with respect to
¹⁰⁶⁴ incident beam axis were investigated with this methodology.

¹⁰⁶⁵ Based on the Emulsion Cloud Chamber (ECC) concept [71], the ES for the FOOT experiment
¹⁰⁶⁶ will be designed with passive materials (as Carbon) alternated to nuclear emulsions films acting
¹⁰⁶⁷ as both high-resolution tracking devices and ionization detectors. It will be composed of three
¹⁰⁶⁸ sections (Fig. 42): vertex and tracking detector, ionization detector for charge identification and
¹⁰⁶⁹ tracking detector for momentum measurements.

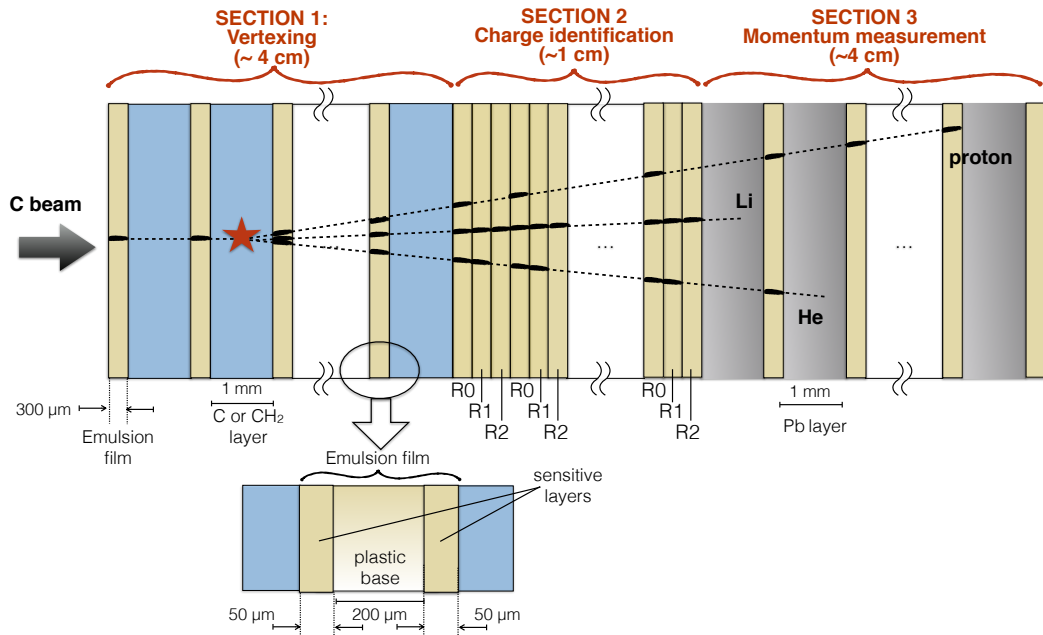


Figure 42 – Scheme of the emulsion spectrometer (ES) composition for the FOOT experiment.

¹⁰⁷⁰ The nuclear emulsion films consist of two 50 μm thick sensitive layers deposited on both sides
¹⁰⁷¹ of a 200 μm plastic base, resulting in a total thickness of 300 μm . The sensitive regions are made of
¹⁰⁷² AgBr crystals of 0.2 μm diameter scattered in a gelatine binder, able to detect Minimum Ionizing
¹⁰⁷³ Particles (MIPs). The trajectory of a MIP is recorded by all AgBr crystals along its path, which
¹⁰⁷⁴ act as latent image centers. A chemical process, known as development, enhances the latent images
¹⁰⁷⁵ inducing the growth of silver clusters (grains) with a diameter of 0.6 μm , which can be seen with
¹⁰⁷⁶ an optical microscope. The grains density is proportional to the ionizations caused by the passage
¹⁰⁷⁷ of the charge particle within the dynamical range.

¹⁰⁷⁸ After the development, the emulsion will be scanned by an automated system. The acquired
¹⁰⁷⁹ image is then analyzed by a dedicated software to recognize clusters of dark pixels aligned, which
¹⁰⁸⁰ represent the track produced by the penetrating particle. A straight sequence of pixels in one
¹⁰⁸¹ emulsion layer defines a "micro-track". Two aligned micro-tracks belonging to the top and bottom
¹⁰⁸² layers of an emulsion film form a "base-track", as shown in Fig. 43. Base-tracks belonging to a
¹⁰⁸³ straight line along different films, are connected to form volume-tracks. Through the propagation
¹⁰⁸⁴ of track segments from an emulsion layer to the next, the particle track is reconstructed and the
¹⁰⁸⁵ segments fitted.

¹⁰⁸⁶ 5.1. Vertex and tracking detector

¹⁰⁸⁷ The ES section 1 will be made of several elementary cells made of Carbon or C_2H_4 layers (1
¹⁰⁸⁸ mm) alternated with emulsion films (300 μm) as shown in Fig. 44. The ^{12}C ions beam will interact

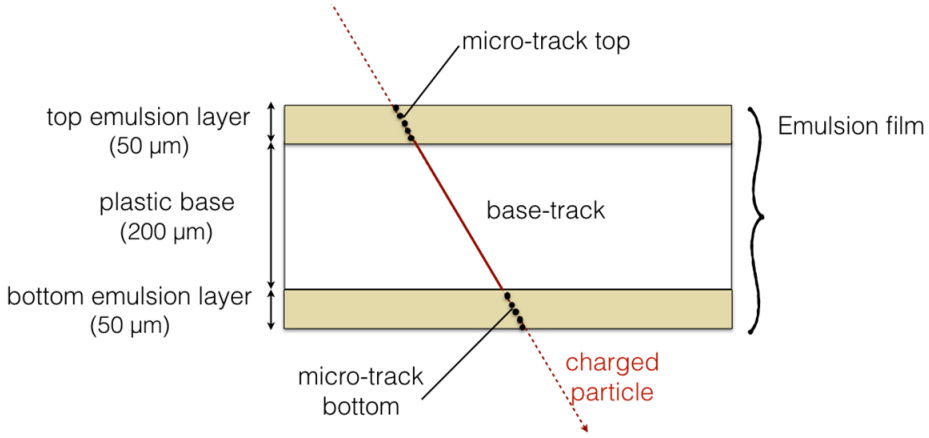


Figure 43 – Scheme of the tracking reconstruction: a sequence of clusters aligned in the top and bottom layers forms a micro-track; geometrically aligned top and bottom micro-tracks forms base-tracks.

with the cells and originate secondary fragments. The detector emulsion structure will track the fragments and reconstruct the interaction vertex position with a micrometric resolution. The section 1 length will be optimized to achieve a statistically significant number of reactions. Assuming that 20% of all ^{12}C ions (at an energy of 400 MeV/u) interact within 30 mm of Carbon [84], the total length of section 1 could be 39 mm, corresponding to 30 elementary cells.

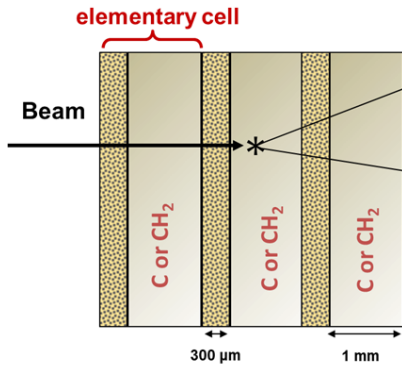


Figure 44 – Scheme ES Section 1: vertex and tracking detector.

5.2. Charge measurement

In nuclear emulsions like those produced for the OPERA experiment [82], the trajectories of particles at the minimum of their ionizing power are observed as thin tracks with a grain density of about 30 grains/100 μm. The latter is almost proportional to the energy loss over a certain range, above which a saturation effect occurs and prevents charge measurements for highly ionizing particles. By keeping the emulsions for an appropriate time at a relatively high temperature (above 30° Celsius) and relative humidity (around 98%), the tracks can be partially or totally erased. In this way, films may be made insensitive to MIPs and suited for highly ionizing particles. This treatment is a controlled fading and is called refreshing because resets the detector. The identification of particles with very different energy release can be achieved using the combination of several films, treated with different refreshing procedure after exposure. This technique allows to overcome the saturation effects of large ionization. This is the basis of the method described

in [83, 84] that will be adopted in FOOT to enlarge the dynamical range of emulsions. The implementation of this technique requires a dedicated machine that must be located inside a dark room equipped also for nuclear emulsion packaging and development. The procedure requires some tuning to be optimized according to the film characteristics.

As the specific ionization along the particle track is proportional to the grain density, the sum of the grain pixels belonging to the same track normalized to a given track length is a variable sensitive to the specific ionization, hence to the particle charge. This variable is called track volume.

The ES section 2, dedicated to the charge identification for low Z fragments (Hydrogen, Helium and Lithium), will be composed by elementary cells, each containing three emulsion films, as shown in Fig. 45.

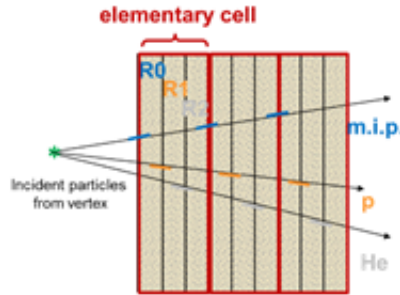


Figure 45 – Scheme of ES section 2: charge identification detector.

In previous works [83, 84] the following refreshing procedure was adopted. Three different treatments were applied to consecutive film triplets and their information was combined to expand the overall dynamical range. The emulsion films, denoted as R_0 , R_1 and R_2 , treated at different temperatures after the radiation exposure and before their chemical development. R_0 was not refreshed and was developed soon after the exposure at room temperature (20°). R_1 and R_2 underwent a three days refreshing at 98% relative humidity and 30°C and 38°C , respectively. For each refreshing condition, a track is characterized by three volume variables, referred to as VR_0 , VR_1 and VR_2 . The R_2 refreshing process results in a complete erase of all tracks caused by particles with charge equal to 1. Therefore, only VR_0 and VR_1 are used for Hydrogen identification. For Helium and heavier nuclei only VR_1 and VR_2 are effective since VR_0 shows saturation. The charge separation is obtained by looking at the correlations between appropriate pairs of variables. The distributions of track volume variables providing the Hydrogen-Helium (H-He) or Helium, Lithium, Beryllium, Boron and Carbon (He-Li-Be-B-C) separation, respectively, are shown in Fig. 46 [83].

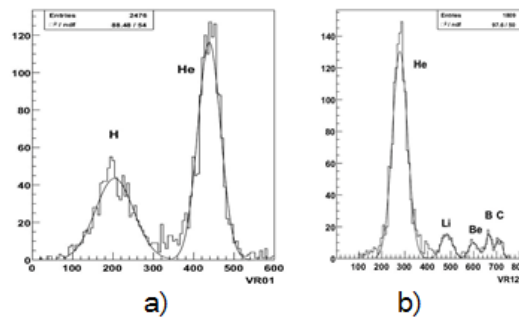


Figure 46 – Track volume distributions providing the charge separation between (a) Hydrogen and Helium (H-He), and (b) Helium-Lithium-Beryllium-Boron-Carbon He-Li-Be-B-C).

Cell	3	9	13	20
<i>H – He</i>	3.3	4.5	6.5	
<i>He – Li</i>	2.6	3.9	4.3	5.0
<i>Li – Be</i>	1.7	2.7	3.1	3.5

Table 3 – Separation of pairs of nuclei expressed in standard deviation for different numbers of elementary cells.

To achieve a separation of H-He and He-Li with an accuracy of approximately 3σ , 3 and 9 elementary cells are required, respectively [83]. The standard deviation for the separation of pairs of nuclei as function of the elementary cells number is reported in Table 3. According to these data, a separation at 3σ of He-Li pairs could be achieved with a detector total length of at least 8.1 mm, corresponding to 9 elementary cells.

The refreshing conditions must be optimized for new batches of emulsions, like those that will be use for this experiment. Different thermal and humidity conditions will be tested in a dark room to establish the working conditions to maximize the emulsion dynamic range and effectively measure the charge of fragments at least up to Lithium.

5.3. Energy and mass measurements

The ES section 3, dedicated to the momentum measurements, is made of emulsion films (300 μm thick) interleaved with 1 mm thick lead plates as passive material (Fig. 47). The momentum will be evaluated with the range technique. Measuring the length of the whole particle track, its kinetic energy will be estimated on the basis of the correlation between range and momentum, using data supplied by NIST [86]. The section length will be set according to the incident beam energy; the number of lead plates will range between 10 and 50.

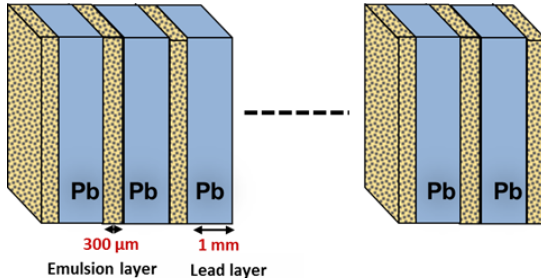


Figure 47 – Scheme of ES section 3 dedicated to the momentum measurement.

The particle trajectory measurements, with high resolution in position and slope, provide also an estimate of the charged particles momentum through the Multiple Coulomb Scattering (MCS) method [87, 88]. For each particle track, the x-y spatial coordinates and the slope (θ_x , θ_y) are estimated. Given the different measurements along a track, the particle momentum is estimated by the MCS method according to the following formula:

$$p(\text{MeV}/c) = \frac{13.6}{\beta \cdot \delta\theta(\text{mrad})} \sqrt{\frac{x}{X_0}} \quad (4)$$

where p is the particle momentum, β the particle velocity, x the traversed distance, X_0 the radiation length in the material and $\delta\theta$ the deviation of the track slope along its path.

By using two independent methods for the energy and momentum estimate (i.e the range and multiple Coulomb scattering) the fragments mass for the isotopic identification can be assessed.

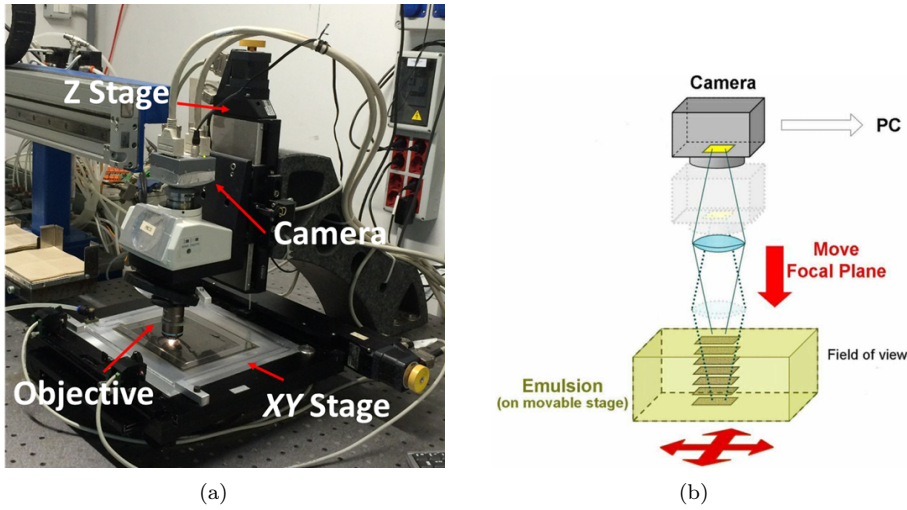


Figure 48 – Emulsion scanning microscope (a) and its schematic layout (b).

1154 5.4. Automated microscopy for emulsion readout

1155 The automated scanning is a fundamental issue for achieving a large scale application of the
 1156 nuclear emulsions. The system consists of a microscope whose main components are: (i) a mo-
 1157 torized stage for the horizontal XY motion of the scanning plate housing the emulsion film; (ii) a
 1158 motor for vertical motion control along Z for focusing; (iii) optics; (iv) CMOS camera for image
 1159 acquisition; (v) an illumination system (Fig. 48(a)) [73, 74].

1160 By adjusting the focal plane of the objective lens through the whole emulsion thickness (Fig. 48(b)),
 1161 a sequence of tomographic images of each field of view are acquired at several depth levels, processed
 1162 and analyzed to recognize aligned clusters of dark pixels (grains) produced along the fragment tra-
 1163 jectory. Each 50 μm -thick sensitive emulsion layer is spanned by 16 tomographic images in order to
 1164 reconstruct micro-tracks as a sequence of grains geometrically aligned. The base-tracks are created
 1165 by connecting micro-tracks across the plastic base. The reconstruction of fragments tracks passing
 1166 through the emulsion spectrometer is obtained by connecting the base-tracks geometrically aligned
 1167 in several consecutive nuclear emulsions (Fig. 42).

1168 A high tracking efficiency working at a speed of about 20 cm²/h and recording tracks with an
 1169 angular acceptance $\theta=30^\circ$ (where θ is the track angle with respect to the direction perpendicular
 1170 to the emulsion plane) was reached with a system developed for the OPERA experiment [73, 74].

1171 Since 2011, the Napoli group carried out a R&D program dedicated to improve the scanning
 1172 performances. A new reconstruction software, LASSO (Large Angle Scanning System for OPERA),
 1173 to extend the track recognition up to $\theta=72^\circ$ and increase the scanning speed was developed [75].
 1174 Two scanning modalities are supported by the LASSO software: the standard Stop&Go (SG)
 1175 mode and the novel Continuous Motion (CM) mode. The scanning speed is 24 cm²/h for the SG
 1176 mode but increases up to 40 cm²/h for the CM mode [76]. The SG and CM LASSO techniques
 1177 are illustrated in Fig. 49. The SG operation mode consists of two steps: the acquisition motion,
 1178 during which the objective lens moves along the vertical axis, and the reset motion, during which
 1179 the objective moves to the next field of view (see the upper section of Fig. 49). The CM operation
 1180 mode consists of a periodic movement of the vertical axis coupled with a horizontal movement at a
 1181 constant speed: during one period of the objective lens displacement, the stage moves from exactly
 1182 from one field of view to the next. The horizontal stage has a constant speed along one of the axes
 1183 while the vertical stage performs the DAQ and the reset motion (lower section of Fig. 49).

1184 The modular structure of the LASSO software is easily tunable to the microscope upgrades
 1185 with new hardware components. The development of a new generation scanning system has been
 1186 accomplished by upgrading the objective lens (Nikon Plan Fluor 20X 0.75 NA) and the CMOS

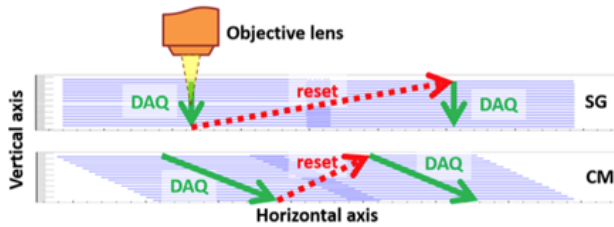


Figure 49 – Schematic representation of the SG (upper section) and the CM (lower section) LASSO scanning techniques.

1187 digital camera (Mikrotron MC-4082camera). A new processing approach based on GPU (Graphics
 1188 Processing Unit) has been employed. The new hardware components integrated with LASSO
 1189 software allows to reach a recording speed of $84 \text{ cm}^2/\text{h}$ in the SG mode [77]. An additional
 1190 factor two in the scanning speed ($190 \text{ cm}^2/\text{h}$) has been achieved by implementing the LASSO
 1191 CM mode [78]. To cope with the scanning volume and large angle track detection requirements
 1192 of the films for the FOOT emulsion spectrometer, the microscope will be upgraded with the new
 1193 hardware and equipped it with the latest generation software.

1194 6. DAQ and Trigger

1195 6.1. Data acquisition principles and limiting conditions

1196 The FOOT detector will be equipped with a DAQ system designed to acquire the largest sample
1197 size with high accuracy in a controlled and online-monitored environment. For a proficient system
1198 few guidelines will be considered in the design:

- 1199** • The maximum acquisition rate should depend on the beam characteristics and/or on the
1200 slowest detectors in the experiment. Along the DAQ chain there should be no bottleneck
1201 that limits the rate.
- 1202** • The system should work in different laboratories and in different acquisition conditions: the
1203 DAQ should be parametrizable and it should store detector data as RAW data files and
1204 configuration data in databases or text files.
- 1205** • The DAQ system should allow an online monitoring of the data taking and a fast quality
1206 assessment of the acquired data.
- 1207** • The storage system should be reliable and the data should be transferred as soon as possible
1208 to the analysis center(s).

1209 At the moment of this writing the slowest detectors are the MIMOSA 28 chips in the pixel
1210 tracker, which have a frame readout time of $180 \mu\text{s}$ [39], needed to readout about 10^6 pixels per
1211 chip. This figure fixes the overall maximum readout rate at about $R_{\max} = 5 \text{ kHz}$. The system will
1212 be designed to handle a maximum DAQ rate of $R_{\text{daq}} = R_{\max}$, but in order to reduce pile-up effects
1213 in the MIMOSA chips the actual trigger rate will be of the order of $R_{\text{trigger}} = 1 \text{ kHz}$. With this
1214 rate, considering a duty cycle of $f_{\text{dc}} = 30\%$, during stable running conditions, up to $N_{\text{day}} \approx 25 \cdot 10^6$
1215 events per day can be collected with a minimum bias trigger. In the following we will consider the
1216 C-C interaction at 200 MeV/u as our run condition baseline. Given the size of the target and the
1217 process cross section, about $25 \cdot 10^4$ events per day of nuclear fragmentation are expected. This
1218 sample size will be enough to perform cross section measurements which will not be dominated by
1219 statistical effects, at least for a large part of the covered scattering angles.

1220 6.2. Trigger system

1221 To avoid any source of systematics due to the trigger selection, the main trigger of the ex-
1222 periment will be very simple: a minimum bias trigger on signals provided by the Beam Counter.
1223 The electronics that will be used to perform the trigger function is a CAEN V2495 board, whose
1224 FPGA and internal logic is fully programmable. At its minimum the board will receive 4 logic
1225 signals from the 4 PMT of the detector and one signal each from each detector with its DAQ status
1226 (IDLE/BUSY) and it will provide the trigger signals (to be distributed by wire to all detectors) and
1227 a couple of time-stamping signals to be used by the different detectors for a spare and additional
1228 synchronization check possibility.

1229 The trigger signal will be obtained asking for at least a time coincidence between two PMT
1230 signals within a gate of 20 ns. This will ensure a negligible amount of noise triggers in practically
1231 all experimental conditions. The internal trigger will be broadcasted to all detectors only if all the
1232 detectors will be idle and enough time has passed since the previous trigger so to complete the
1233 readout cycle.

1234 The board will be also a source of DAQ information about the trigger given: its time (in clock
1235 ticks) since the previous trigger, live time since previous trigger, PMT signal counters, information
1236 for synchronization, information on the BUSY signal releases, global information on the beam
1237 suitable to be used for normalization of the data acquired.

Table 4 – DAQ components, rates and bandwidths.

Detector	Board(s)	DAQ channels	max event rate (kHz)	Event size (bytes)
Trigger	V2495	1	10	40 B
Start Counter	DreamWave	4	1	8.2 kB
Beam Monitor	TDC	36	5	0.1 kB
Vertex detector	SoC on DEx	$4 \cdot 10^6$	2	0.9 kB
Inner tracker	SoC on DEx	$28 \cdot 10^6$	2	2.1 kB
Outer tracker	Custom	$6 \cdot 10^3$	2	0.5 kB
$\Delta E/\Delta x$	DreamWave	80	1	8.4 kB
Calorimeter	QDC	400	2	1.7 kB
Total DAQ	Storage PC	-	1	22 kB

6.3. Data acquisition infrastructure, data rates and volumes

The DAQ system we will implement is a flexible hierarchical distributed system based on linux PCs, VME crates and boards and standard communication links like ethernet, USB and optical fibers, as already done in several big[89] and small[90], [91] experiments. The control of the system will be hosted on a PC (Head PC) used to run the DAQ GUI interface to start/stop a single run, to control and to configure other nodes in the system. Another PC (Storage PC) will be used to collect the information coming from the different detectors, to perform an event building and to store on disk the acquired data. On the same PC a MYSQL DB will have the role to store the configuration data (structured DB tables or in form of retrievable text files) and to store DAQ process information (start/stop DAQ time, events collected, other global DAQ information). An electronic logbook[92] interfaced with the DAQ system will actually be installed on the same machine.

The actual readout systems can be in the form of standard VME boards placed in VME crates or in the form of PC or other boards reachable by the DAQ via ethernet. The ethernet link is required by the DAQ system for providing commands (and receiving feedbacks). The data to be collected can use ethernet, USB or optical fibers to reach the Storage PC. In case of VME crates, a Single Board Computer (SBC) is needed in each crate to dispatch DAQ commands on the different boards in the crate. Each single board in a crate can be individually configured and read out during the different DAQ phases. VME boards reading different detectors can be placed inside the same crate.

Taking into account the possibility to perform the zero suppression algorithms online on most of the detectors in the front-end electronics, the estimated average event data size is of the order of 22 kB to be acquired at an average rate of 1 kHz. This fixes the data collection capability of the system at the busiest node (the storage PC) to be of the order 22 MB/s on average. Taking into consideration a safety factor of 4, a minimal bandwidth of 90 MB/s will be considered in the DAQ system design. This number is in principle still compatible with an event dispatch performed mainly on ethernet links, but needs to be checked with realistic ethernet frame lengths and frame rates. Tests on lab with a realistic data switch will provide the information if we need dual or quad -port ethernet card on the storage PC. The minimal bandwidth needed is not fully compatible with the average performance of standard hard disks. For this reason the storage PC will be equipped with a 1 TB SSD element (mean transfer rate of 400 MB/s) to be used for temporary data storage during running conditions. During data taking, the final storage will be on a dedicated NAS system. Considering a typical beam test of 1 week time, and allowing a 30% beam efficiency, in about 50 h of stable running conditions a total data size of 36 TB of data per test beam can be foreseen. During beam test time, the acquired data will also be transferred to the CNAF analysis center for offline processing.

6.4. Online monitoring

The DAQ system will be equipped at least with several sets of online monitoring information. Simple information pieces on the DAQ running can be collected from each VME board or data

1277 provider at a monitoring rate (typically each 10 s) and provided to a network of PCs connected to
1278 the experiment. A second more informative information will come in the form of histograms filled
1279 on each PC in the system using local data. Typical histograms will show detector occupancies,
1280 particle arrival times, particle energies, collected charges and so on. In general, at this level, any
1281 information that can be obtained processing data collected by a single PC can be shown.

1282 A third and more powerful online information will come from a fast online event reconstruction
1283 performed on the fly on a fraction of events. With a complete reconstruction it will be possible
1284 to have, on part of the data, track momentum spectra, times-of-flight, A and Z reconstructed for
1285 charged tracks.

1286 All these data will be available to the DAQ crew and detector experts during data taking.

1287 7. Software

1288 Software plays a fundamental role in FOOT. At present, the most important software components
1289 are those concerning simulation and data reconstruction. Section 7.1 describes the general
1290 simulation framework, with a specific attention to the electronic detector setup, while Sec. 7.2 is
1291 dedicated to the simulation of the emulsion spectrometer. The software framework for data recon-
1292 struction (both simulated and real) is then discussed in Sec. 7.3. The reconstruction software for
1293 the emulsion setup has been described elsewhere in literature [77, 78].

1294 7.1. Simulation

1295 During the planning stage the complete simulation of the entire FOOT experimental setup
1296 is a powerful tool to optimise the design and to identify possible critical points in the layout.
1297 The simulation aims to investigate the detectors expected performances, in order to improve the
1298 experimental accuracy and to learn how to reconstruct the events by combining the signals from
1299 the different detectors.

1300 The FOOT simulation has been built in the framework of the FLUKA code [8, 9]. FLUKA
1301 is a Monte Carlo transport simulation code robustly tested through the comparison with many
1302 experimental data and now extensively adopted in many physics fields of study, such as particle,
1303 nuclear and medical physics. In particular, many FLUKA developments, concerning both physics
1304 models and user interface, have been studied for its application in the context of hadrontherapy. To
1305 this purpose, FLUKA is used at CNAO and HIT. A recent review of FLUKA application in particle
1306 therapy can be found in ref. [93]. Furthermore FLUKA has been used also for the simulation of
1307 experiments dedicated to fragmentation [94, 6] and test beams for the study of secondary particles
1308 production with therapeutic beams [95, 96, 97].

1309 To run the simulation, the user must provide a description of the setup and some physical
1310 specifications, which have to be included in input and geometry files. The required FLUKA input
1311 specifications are:

- 1312** • dimensions and distances between the geometry regions, *i.e.* targets and detectors
- 1313** • material compositions and properties
- 1314** • source position, beam particle type, energy, spatial and/or momentum spread
- 1315** • magnetic fields description
- 1316** • physics options (*e.g.* production and transport energy cutoffs, δ -rays production thresholds
1317 and activation of heavy fragments evaporation to achieve accurate results for residual nuclei
1318 production)

1319 A geometry and input files configuration program has been developed in order to simplify the
1320 implementation of geometry or simulation parameters changes. Starting from some user defined
1321 values of detectors dimensions, positions, distances and other customized parameters, this program
1322 produces the input and geometry files in a FLUKA readable format.

1323 The entire setup geometry and materials have been accurately implemented in the input and
1324 geometry files (see Fig. 12 for a 3D rendering). The MC code handles the transport of all primary
1325 and secondary particles throughout the experimental volume and scores the quantities of interest.
1326 To simulate particles interactions with the different materials, FLUKA makes use of experimental
1327 cross sections, if available, otherwise different theoretical models are employed, according to the
1328 interacting particle type and energy. An example of simulated interaction of a primary ^{16}O ion
1329 with a polyethylene target is sketched in Fig. 50

1330 At present, the primaries are simulated as a beam along the z direction, with a FWHM in the
1331 transverse directions mimicking a real therapeutic beam. However, the ion source parameters can
1332 be adjusted to simulate the real beam of a selected facility.

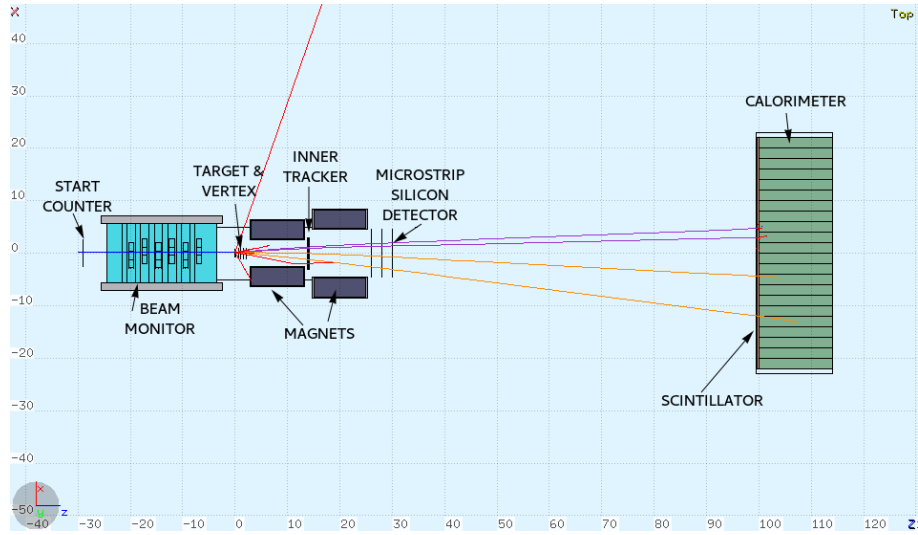


Figure 50 – Schematic 2D event display of a primary ^{16}O (blue) ion interacting with a polyethylene target (colored lines: fragments).

In order to achieve a very accurate tracking of particles interactions in air, target and active regions of the detectors, low production and transport cutoffs and δ -rays thresholds have been specified. Higher thresholds and cutoffs have instead been applied to the insensitive regions to save CPU time and effort.

We decided not to include in the simulation step any detectors response efficiency or smearing, as they will be implemented in the reconstruction step.

Although FLUKA offers a wide range of options for the scoring of the most common quantities of interest, a non-standard output was required to fully handle the simulation and to study detectors responses and performances. This was achieved by means of FORTRAN77 user routines, which allow the user to build its own customized output and to overcome some standard FLUKA limitations.

Another *ad hoc* user routine was used to integrate a 3D magnetic field map in the simulation. The map is stored in an ASCII file containing the three magnetic field component correspondent to a grid of 3D points. At present, an approximated field map with B_x and B_z null and B_y z -dependent has been adopted. B_y was calculated as a sum of two Gaussian, their means coincident with the magnets centers and reasonable sigmas. FLUKA combines the magnetic map to the geometry layout to perform a correct particle transport throughout the detector setup (see Fig. 51). However, when tracking particles in magnetic field, the crossings between different regions is approximated by FLUKA: to find the crossing point, the equation describing the surface of the region and the equation describing the particle helix trajectory in magnetic field must be intersected, and this implies to solve an up to 4th grade equation. For the distance between two subsequent interaction a default accuracy of 0.05 cm is adopted in generic inputs. However, when dealing with very thin detectors (\sim tens or hundreds of μm) as in the case of FOOT silicon detectors, an increased accuracy must be specified. The suitable accuracy value was set as the best compromise between the requested precision and an excessive CPU time consume.

The FOOT simulations output is an ASCII file which stores *event by event* information about all the generated particles and their interactions with the detectors. To make the handling of the FLUKA output easier, the ASCII file is converted into a ROOT file by a simple portable code. The output information is therefore stored in Tree Branches that can be easily read by the reconstruction algorithm.

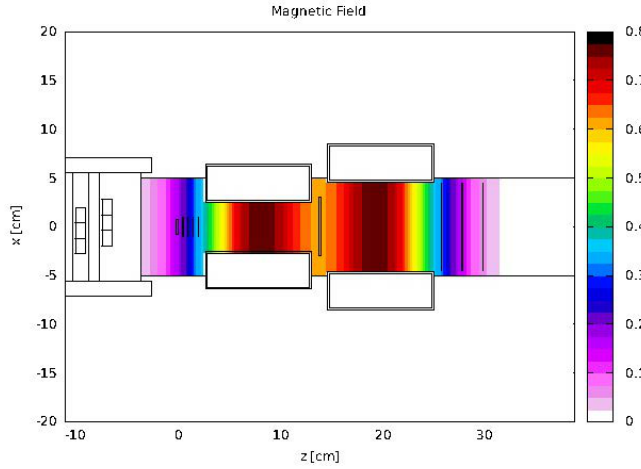


Figure 51 – Representation of the magnetic field intensity read from a magnetic field map and integrated in the FOOT setup. The picture has been created from Flair, the FLUKA geoviewer [98].

1363 7.2. Emulsion Spectrometer simulation

1364 The experimental layout for the run with nuclear emulsions will consist in the Start Counter,
 1365 the Beam Monitor and the Emulsion Spectrometer, as shown in Fig. 52. In order to evaluate
 1366 the performances of the ES, a simulated 250 MeV/u ^{12}C beam centered in zero with a gaussian
 1367 distribution in x-y plane with FWHM \sim 1cm was used.

1368 Less than 1% of carbon ions interact in the detector material before reaching the ES, while
 1369 \sim 13% undergo inelastic scattering in the first section of the Emulsion Detector (ES Section 1),
 1370 devoted to the reconstruction of the interaction vertex. The remaining ions are divided in the
 1371 following categories: interacting in ES Section 2 (\sim 4%), interacting or absorbed in ES Section 3
 1372 (\sim 83%).

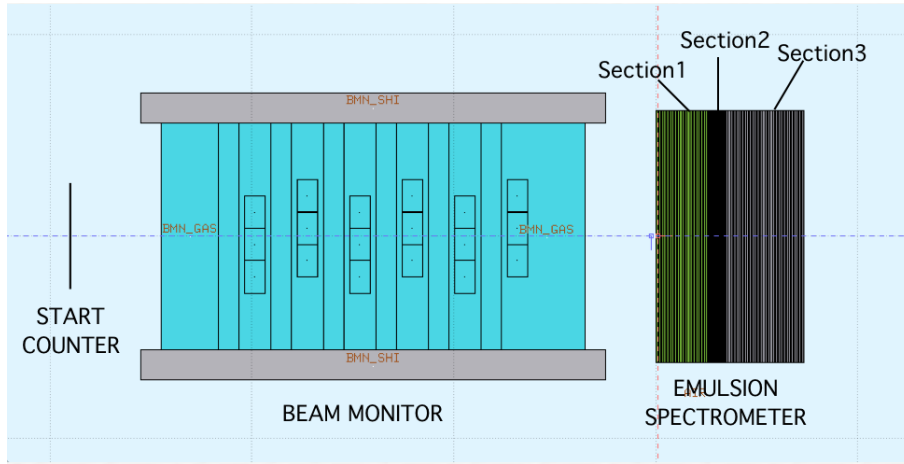


Figure 52 – Schematic 2D view of the simulated setup for the measurements with the Emulsion Spectrometer.

1373 The position of carbon interaction vertices along the beam axis is shown in left panel of Fig. 53,
 1374 while the right one reports the final kinetic energy of the carbon ions as function of the interaction
 1375 depth. The 250 MeV/u C beam is completely absorbed within 5.3 cm, corresponding to about the
 1376 middle of ES Section 3.

1377 On average Carbon interactions produce seven charged fragments of which the kinetic energy
 1378 and the emission angle distributions are reported in Fig. 54. Must be remarked that the simulation

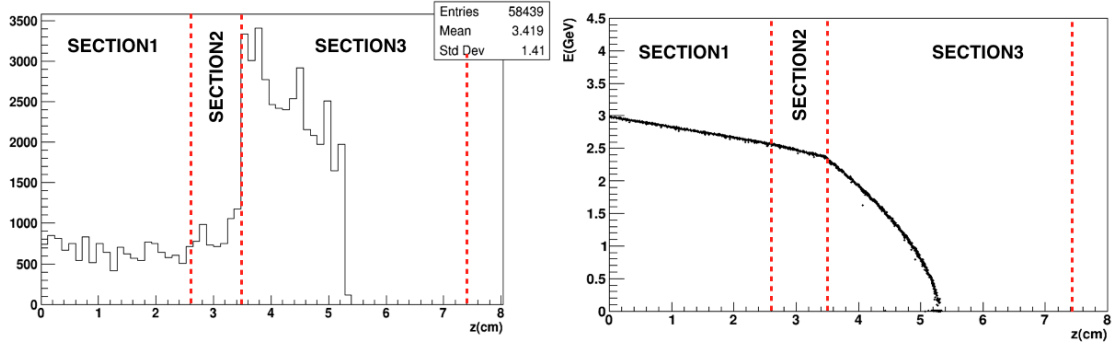


Figure 53 – Left: position of carbon interaction vertices in the Emulsion Spectrometer. Right: final kinetic energy of C ions as function of interaction depth. Red vertical lines represent the limits of the three sections.

1379 results obtained are generated by the FLUKA nuclear model and can be taken only as general
 1380 indication of the future data features.

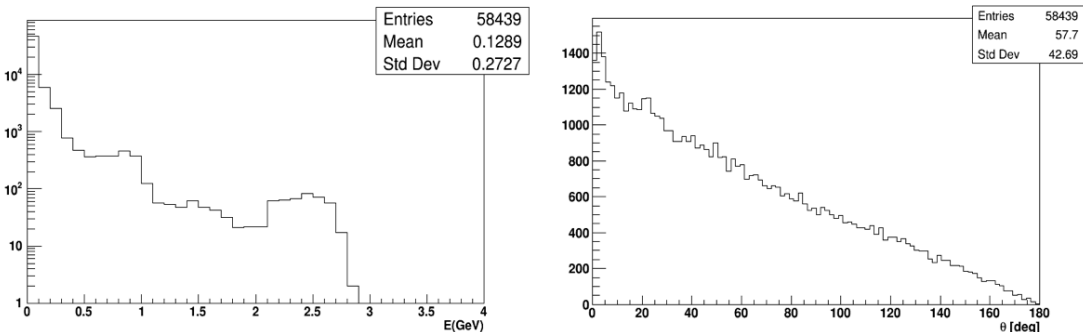


Figure 54 – Kinetic energy (left) and emission angle (right) distribution of fragments produced in 250 MeV/u ^{12}C interactions in the Emulsion Spectrometer.

1381 7.3. Reconstruction

1382 In the FOOT experiment, the full reconstruction chain for both data and simulated events
 1383 (from different detectors I/O digestion to fragment identification) is performed by a ROOT based
 1384 framework, developed in the GSI laboratory within the FIRST collaboration. The code uses a
 1385 hierarchical structure to obtain a solid and simple object-oriented architecture. A high final user
 1386 customization level is guaranteed through several parameter card-files.

1387 While the I/O and the chain of algorithms is handled by the *TAGroot* and *TAGdata* base
 1388 classes, the actual code that is going to be executed for each event is provided by the user through
 1389 the implementation of classes that are inheriting from *TAGaction*. Such algorithms need as input
 1390 either a root ntuple (MC) or a *TAGdata* object, and provide an output in the form of a *TAGdata*
 1391 object that can be (re)used by subsequent actions to perform structured tasks. Additionally, the
 1392 actions can use *TAGpara* objects that are used to implement both the geometrical and calibration
 1393 information of each detector and that can be retrieved and applied during the reconstruction
 1394 process.

1395 The reconstruction software package handles the decoding of the data and simulation events,
 1396 building in two main steps all the necessary input information to perform a full event reconstruc-
 1397 tion and analysis. The first step of the reconstruction code consists in reading, interpreting and

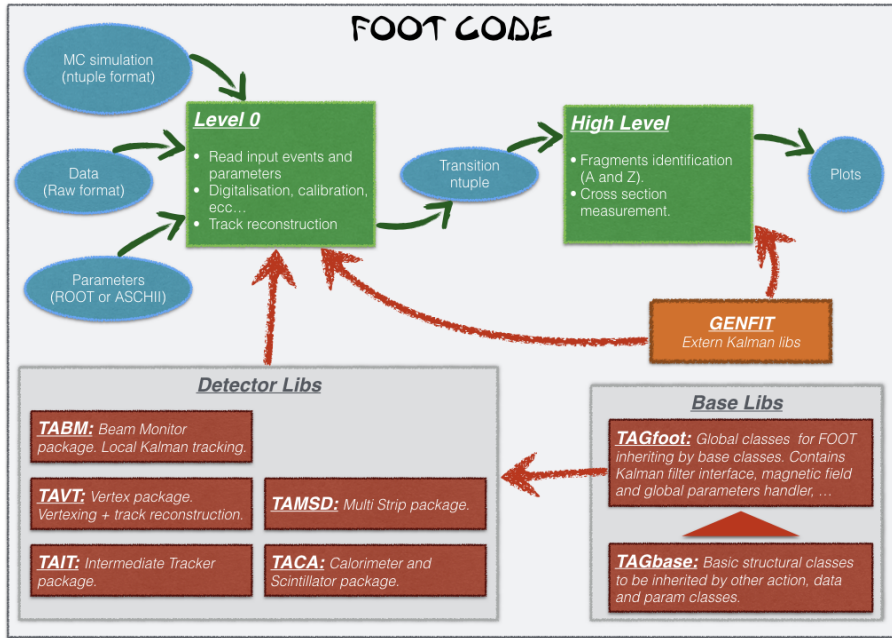


Figure 55 – FOOT code diagram.

1398 converting in a single software-object format both the data and the simulation events provided
 1399 in different input formats. Data are given in raw format by the DAQ system (digitized signals,
 1400 ascii and dat files) while the simulation files are in ntuple format (scoring performed using the
 1401 FLUKA software and simulation in ROOT files). In a second step, events are processed by track
 1402 identification and reconstruction algorithm giving the needed information for the fragmentation
 1403 studies and results. The basic structure is detailed in fig. 55.

1404 The first reconstruction level will be referred to, in the following, as *Level0*. At the *Level0*, the
 1405 signals collected during the data acquisition runs are decoded, the detector dependent calibration
 1406 constants are applied and the output of each detector is organized in "Hit", "Cluster" and "Track"
 1407 objects whose definition and additional informations will depend on the detector type.

1408 Simulated events are executed and processed by specific algorithms that takes the FLUKA
 1409 simulation geometry, apply the necessary scaling factors, resolutions, efficiencies (that will be
 1410 calibrated and fine tuned against the collected data) and provide the output in the same object
 1411 format provided during data events decoding ("Hit", "Cluster", "Track"). The only additional
 1412 information, that will be kept in the event output in order to allow efficiency and resolution
 1413 studies, is the MC truth matching information, only available for simulated events.

1414 This algorithm structure allows for the development of a second reconstruction level, named in
 1415 the following *HighLevel*, in which the objects built from the different sub-detector units (e.g. the
 1416 beam monitor, the vertex detector, the tracking system, the scintillator wall and the calorimeter)
 1417 will be combined achieving a final global event reconstruction. The different fragments, together
 1418 with the incoming beam particle, will be identified and their track will be reconstructed, providing
 1419 all the necessary input for the cross section calculation. At this level, the inter-calibration of the
 1420 various detectors (positioning, energy and momentum measurement) will play a crucial role in
 1421 reducing the combinatorial background. The different input type (data or simulation events) will
 1422 be entirely transparent for the full event reconstruction algorithms development as they will have
 1423 exactly the same *Level0* input objects in both cases.

1424 By structuring the software reconstruction in two layers the computing resources will be han-
 1425 dled more efficiently as it will be possible to produce different re-processing of the same data or

1426 simulation sample in which the calibration constants or other detector-related quantities are going
1427 to change, without re-running each time the full-event (*Level0* plus *HighLevel*) reconstruction. The
1428 track reconstruction is based on a Kalman filter algorithm implemented in the external open source
1429 GENFIT library [99]. The FOOT code is fully interfaced with GENFIT and provide two different
1430 track reconstructions. A projectile reconstruction is performed using the Beam Monitor hits alone
1431 for beam monitor purpose (4.1). A global track reconstruction of fragments is done combining hits
1432 from Vertex, Inner Tracker and Micro Strip detectors detailed in Chapter 8.2. The matching with
1433 the hits detected in the scintillation wall and the clusters in the calorimeter will be made on the
1434 basis of the extrapolation performed using the track information at the exit point from the Micro
1435 Strip detector. The information about the incoming beam direction will be instead provided by
1436 the beam monitor detector and will be used for the inverse kinematic calculations.

1437 As an example of a *Level0* reconstruction implementation it is possible to follow the vertex
1438 pixel silicon detector processing. Starting from the decoding of the fired pixels, to provide a
1439 collection of Hits, Clusters of hits will be made and used to build track candidates using a Hough
1440 transform algorithm. Several tracks will be finally combined together to measure the position of
1441 a possible common production vertex. The *HighLevel* reconstruction starts from the track and
1442 vertex provided by the Vertex detector and proceeds, using a Kalman filtering algorithm, adding
1443 the hits detected by the Inner Tracker and the Micro Strip detectors.

Material	Density (g/cm ³)	Fragmentation percentage
1° Mylar (C ₁₀ H ₈ O ₄)	1.4	28%
Gas (Ar-CO ₂ 80% – 20%)	1.68 10 ⁻³	41%
Field wires (Al)	2.70	2%
Sense wires (W)	19.3	< 1%
2° Mylar (C ₁₀ H ₈ O ₄)	1.4	29%

Table 5 – Approximate percentages of fragmented primary particle in the BM reported for every BM component.

8. Expected Performances

In this section we summarize the main results emerging from the studies on the performances that FOOT experiment can achieve as far as the main physics items are concerned. These studies include considerations deriving from the experience gained in previous experiments, and the analysis of the new simulation studies. Also new experimental results from recent test beam activities are included. The Beam Monitor performance will be discussed, in Sec. 8.1, while in Sec. 8.2 the initial studies about the global tracking and momentum measurements will be introduced. The performances of Calorimeter are presented in Sec. 8.3. The FOOT capability in resolving Z and A is reported in Sec. 8.4. Finally, Sec. 8.5 is dedicated to the aspect of inverse kinematics reconstruction.

8.1. Study of the out of target fragmentation

The purpose of the Beam Monitor (BM) in the FOOT experiment is to measure the direction of the incident beam and reject the events in which the primary ion has fragmented before the target. The primary ion passes through different amounts of material which can lead to fragmentation processes before the target, mostly in the Start Counter (SC) and the BM material.

8.1.1. Expected fragmentation in Start Counter

From MC simulations, the estimated percentage of fragmentation events in the SC is $\sim 0.13\%$. As shown in Fig. 56, protons are the most abundant fragments, and, for increasing charge, particles are produced with a smaller angular deflection. Secondary particles produced in the SC can increase the number of hits in the BM and have an initial angular deflection that can be exploited to identify and reject such events. Problems arises for events in which only one fragment crosses the BM, since the particle track is in principle identical to the track of a primary ¹²C ion, leading to a misidentification that could not be solved. Typically these are the cases where there is the production of Boron and Carbon isotope nuclei, which in addition have a small angular deflection (Fig. 56) and give rise to an unrejectable background.

8.1.2. Expected fragmentation in Beam Monitor

In addition to the fragmentation in the SC, inelastic nuclear interactions of the projectile can occur in the BM material: mylar windows, gas or the wires. We can neglect, as a first approximation, surrounding air. The MC estimate for this contribution in the BM is $\sim 0.1\%$, similar to that of the SC. The fragmentation percentage for each BM component is reported in tab. 5.

If the projectile undergoes nuclear interactions on the first mylar window or before the last plane of cells in the BM, it is possible to reject the event since the produced particles can be detected. On the other hand, the events with the fragmentation of the projectile on the second mylar window cannot be rejected, since the primary particle leaves a signal in the BM identical to an event without nuclear interactions before the target. Therefore, it is expected at least a $\sim 30\%$ of the events fragmenting in the BM material (*i.e.* $0.3\% \times 0.1\% = 0.03\%$) will constitute a sort of unrejectable background, mainly due to primary fragmentation in the second mylar window. However, the vertex detector placed beyond the target could be useful in identifying these very few critical events.

1484 8.1.3. *BM and SC rejection performances*

1485 In spite of the estimated low level of background due to fragmentation events in SC and BM,
1486 a possible strategy has been envisaged to reject this background. Taking into account MC infor-
1487 mations, a tracking algorithm has been developed by means of the GENFIT software. Analyzing
1488 the parameters of the fitted tracks, different criteria have been defined in order to reject the events
1489 in which the primary ion undergoes fragmentation before the target (background) and accept the
1490 events without fragmentation (signal).

1491 • Number of hits.

1492 The first selection criterion is given by the number of hits read in the BM. A projectile that
1493 reaches the target crosses all the BM generating in most of the cases 12 hits in total (1 hit
1494 per plane). It has been found that an amount of 2% – 3% of events in which the projectile
1495 fragments in the target produces light particles that back-scatter towards the BM, generating
1496 a signal and increasing the total number of hits per event. On the contrary, the background
1497 events have a high hit multiplicity, since there are more particles that could enter in the BM.
1498 In particular, only 13% and 33% of the events with a fragmentation in the SC and in the
1499 BM respectively give rise to a number of hits equal to 12.

1501 • Fitted track direction

1502 Given the track direction, the angle of the track with respect to the beam incoming direction,
1503 can be exploited as a criterion of selection. If the projectile does not undergo fragmentation,
1504 it is subject to the multiple Coulomb scattering and nuclear elastic scattering leading to an
1505 average angular deviation $\theta < 0.4^\circ$. On the contrary, particles produced in a nuclear inelastic
1506 scattering are emitted with an average angular deviation $\theta \gg 0.4^\circ$, as shown in the Fig. 57.

1507 Applying a cut on the fitted track direction $\theta < 0.4^\circ$, it is possible to reject $\sim 96\%$ and 61%
1508 of the events with fragmentation in the SC and in the BM respectively, with a $\sim 1\%$ of loss
1509 of efficiency on the signal.

1510 • Reduced χ^2

1511 The reduced chi-squared statistic (χ^2_ν) is extensively used in testing the goodness of fit and it
1512 can be adopted as selection criterion. The χ^2_ν distributions for signal and background events
1513 are shown in Fig. 58. The main difference in the χ^2_ν distribution between the signal and the
1514 background datasets stays in the tails: 98% of signal events have $\chi^2_\nu < 3$, while the events
1515 with an inelastic interaction in the SC and BM have a longer tail reaching values of $\chi^2_\nu > 100$,
1516 respectively only 29% and 39% of the background events have a $\chi^2_\nu < 3$.

1517 By combining the selection criteria it is possible to reject the events with nuclear inelastic
1518 interactions in the SC and in the BM material, with a rejection power of 0.96 and 0.7 respectively,
1519 and with a reconstruction efficiency of 0.97. The unrejected SC-fragmentation background events
1520 are mostly given by the production of Boron and Carbon isotope nuclei, while the surviving BM-
1521 background events are those in which the projectile has fragmented after the last cell layer or on
1522 the second mylar window.

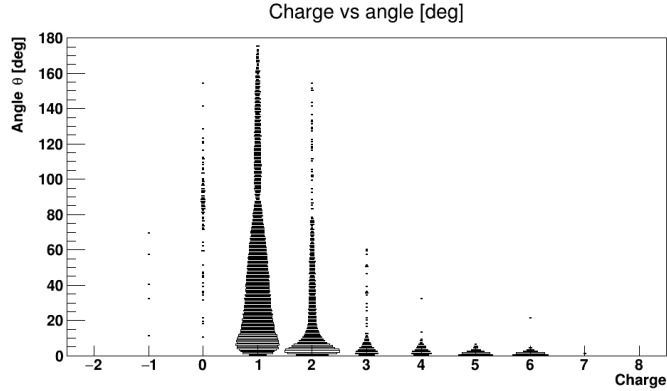


Figure 56 – Fragment production angle as a function of the charge produced in the SC.

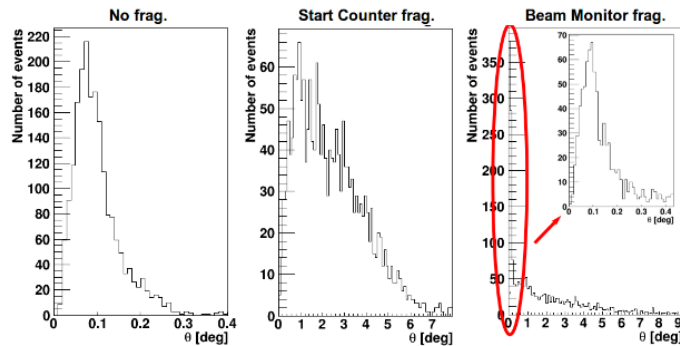


Figure 57 – Left panel: Angular distribution of non-interacting primaries entering BM. Center panel: Angular distribution of primaries entering BM after an interaction in the SC. Right panel: Angular distribution of primaries which interact in the BM material.

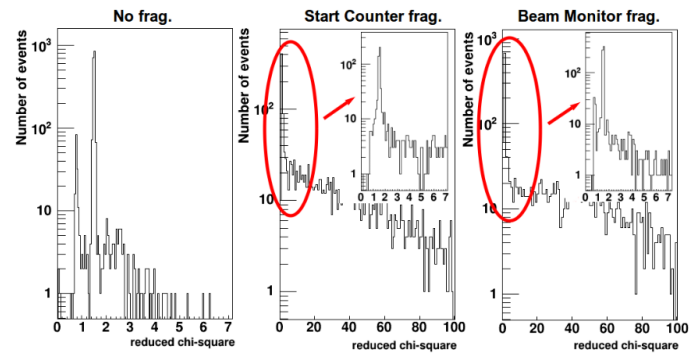


Figure 58 – Reduced χ^2 distribution from track fitting for non-interacting primaries entering BM (left panel), for primaries entering BM after an interaction in the SC (center panel) and for primaries which interact in the BM material.

1525 8.2. Global Tracking and Momentum Measurement

1526 FOOT adopts a global tracking reconstruction algorithm based on a Kalman filter procedure.
1527 The Kalman filtering is a well established method in particle physics that allows the highest per-
1528 formances in track reconstruction and momentum measurement. Moreover it can combine the
1529 information coming from different type of detectors taking full advantage of the FOOT specific
1530 design with three different detectors spaced out by magnets that maximize the momentum identi-
1531 fication performance.

1532 The use of a Kalman filter based tracking algorithm gives the best possible tracking perfor-
1533 mances. It should allows a momentum resolution $\sigma(p)/p$ at level of 5% enough to improve the
1534 isotope separation trough the A measurement and to fulfill the physics goals of the FOOT experi-
1535 ment.

1536 The extended Kalman filter is an efficient recursive algorithm that finds the best estimate for
1537 the state of dynamic systems (a parametric state equation) from a series of noisy measurements.
1538 It considers each detector surface with a possible measurement hit as a different equation state
1539 characterized by the set of parameters (state vector). These states are used to built up the the final
1540 track in two steps. First, the algorithm extrapolates a possible trajectory from a measurement
1541 point on a state to the next state, accounting for multiple scattering and energy loss through
1542 matter. Second, on the new state, it calculate a weighted average, via χ^2 minimization, between
1543 the extrapolation (prediction) and the detector measurement (hit).

1544 The Kalman filter implementation is based on the experiment-independent, open source GEN-
1545 FIT library [99]. GENFIT is designed to allows the simultaneous fit of measurements coming from
1546 different type of detectors. It also implements a variety of track-fitting algorithms among which
1547 the standard Kalman filter algorithm [14] and the deterministic annealing filter (DAF) [15, 16].
1548 The state-to-state extrapolation algorithm is based on the STEP code used by the ATLAS experi-
1549 ment [21, 22], an adaptive Runge-Kutta-Nystrom extrapolator of fourth order. It semi-analytically
1550 updates the transport Jacobians along with the numerical evaluation of the track parameters. Spe-
1551 cific features for the low-momentum environment has been developed by the Belle II collaboration,
1552 including a precise handling of energy loss and the calculation of flight-time estimates that take
1553 into account energy loss along the track as well as the effects of different mass hypotheses. GEN-
1554 FIT also interfaces with the RAVE library [23], a generic vertexing toolkit, helping in the vertex
1555 recognition.

1556 At present, the specific implementation in FOOT uses the standard Kalman filter algorithm
1557 but studies are ongoing on the use of the DAF that should be more robust in the presence of
1558 multiple background hits.

1559 The hits measured by the three FOOT tracking detectors are treated differently depending on
1560 the specific typology of the sub-detector itself. The hits from the two pixel detectors (Vertex and
1561 Inner Tracker) are considered as space point measurements. A significantly smaller uncertainty
1562 along the z direction, the direction perpendicular to the sensor surface, than along x and y axes is
1563 enough to maintain the reconstructed state vector inside the pixel itself, nonetheless maintaining
1564 a small freedom along z axis. A planar treatment, implying a rigid constraining on the z position,
1565 degrade significantly the reconstruction performances. Regarding the Micro Strip detector, the
1566 single strip hits coordinates, together with the strip layer, are combined by the reconstruction code
1567 to produce 3-dimensional hit points. These hits are then processed by GENFIT and considered
1568 likewise the pixel detectors hits.

1569 The total processing time is $3\mu\text{s}/\text{events}$ of which $1.8\mu\text{s}/\text{events}$ for the Kalman filter processing
1570 only.

1571 8.2.1. Momentum Performance

1572 The main goal of the FOOT experiment is the differential nuclear fragmentation cross at a
1573 precision level of 5% necessary for hadrotherapeutic purpose. To fulfill this competitive aim, the goal
1574 is to reach a momentum resolution at a level of at lest 5%. In order to test and optimize the
1575 FOOT momentum resolution performances, a set of simulated MC samples have been processed

1576 using a standard Kalman tracking algorithm. A not uniform magnetic field is approximated by
 1577 the convolution of two gaussian distributions each relative to a single magnet, on hold of a more
 1578 accurate field vectorial map made on real magnets. The simulation of the material has been care-
 1579 fully checked to be the same as in the simulation code for its role in the state-to-state propagation
 1580 of the track during the Kalman procedure.

1581 In each event, the reconstruction is performed separately on independent collections of hits
 1582 belonging to the same fragment and passing through all the 3 downstream tracking detectors. At
 1583 the moment, no background or mismatched hits are considered so far. Different hit collections are
 1584 processed with the correct charge and mass hypothesis to test the Kalman filter response on all
 1585 the produced ions and isotopes. Only the principal isotopes are considered: ^6Li , ^8Be , ^9Be , ^{10}Be ,
 1586 ^9B , ^{10}C , ^{11}C , ^{12}C and ^{12}N .

1587 The reconstruction algorithm present an efficiency $\geq 99\%$ for all the fragments of interest.

1588 The comparison between the initial generated momentum of the fragments (green) and the
 1589 corresponding reconstructed ones (red) is reported in Fig. 59 using a simulated sample of an ^{16}O
 1590 projectile of 200, 350 and 700 MeV/nucleon hitting a C_2H_4 target. The peaks of the distribution
 1591 corresponds to the different considered fragments. The distributions of the reconstructed momen-
 1592 tum are compatible with the generated one. The current resolution allows to disentangle only light
 1593 fragments but not the heavier ones. The situation slightly improves in the case of sample with the
 1594 ^{16}O projectile at 700 MeV/nucleon.

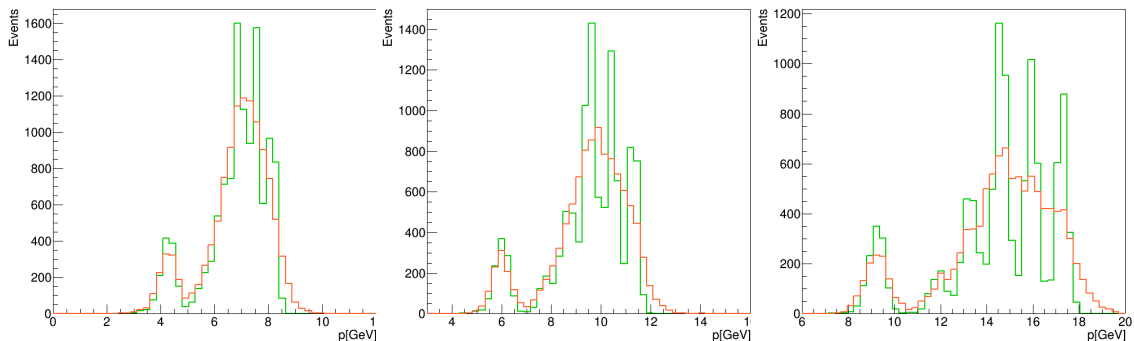


Figure 59 – Generated (green) and reconstructed (red) momentum distribution of the considered fragments in each event for an Oxygen projectile of 200MeV/nucleon (left), of 350MeV/nucleon (center) and of 700MeV/nucleon (right)

1595 In order to estimate the relative momentum resolution $\sigma(p)/p$, the quantity $(p_{gen} - p_{reco})/p_{gen}$
 1596 is plotted in 200 MeV wide bins of the fragment generated momentum and fitted using a Gaussian
 1597 function (no background expected). If the distribution has relative uncertainty greater than 10%,
 1598 the momentum bin is rejected. The momentum resolution as a function of the MC generated
 1599 momentum is presented in Fig. 60 for 200, 350 and 700 MeV/nucleon ^{16}O momentum, respectively.
 1600 This preliminary momentum resolution ranges from 4.5% to 5.5%, already not far from the goal
 1601 of the experiment. We point out that an almost flat resolution obtained in the 200-700 MeV/u
 1602 kinetic energy range. At the lower end the resolution is limited by the Multiple Scattering in the
 1603 detector materials, while seems to be driven by the tracking system resolutions at higher momenta.
 1604 At present, an optimization work is ongoing to further improve the obtained results.

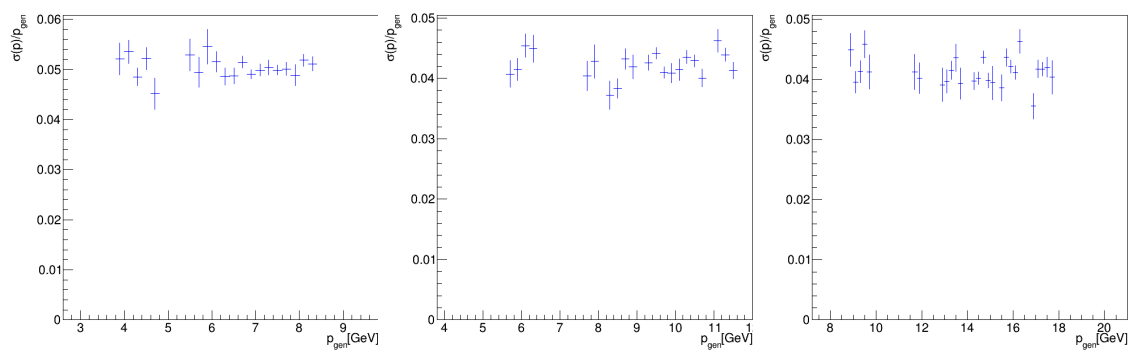


Figure 60 – Differential momentum resolution as a function of the generated momentum for an Oxygen projectile of 200MeV/nucleon (left), of 350Mev/nucleon (center) and 700MeV/nucleon (right)

1605 8.3. Calorimetric measurement

1606 The calorimeter performances have been studied with two different setup using the FLUKA
1607 package. The first one (section 8.3.1) is dedicated to the investigation of the impact of the calorime-
1608 ter length on the energy containment of the fragments. In parallel, the setup of the segmented
1609 calorimeter has been used to study the event characteristics and the calorimeter performances in
1610 a more general framework (section 8.3.2). The performed results obtained from both mono-block
1611 and full crystals simulation are preliminary.

1612 8.3.1. Calorimeter Length study

1613 To study how the calorimeter length impacts on the energy containment of the fragments a
1614 dedicated simulations has been performed using a single BGO scintillating crystal. In this case
1615 the calorimeter was simulated as a mono-block cylinder of 22 cm of diameter. The performances
1616 with three different lengths of BGO (7, 14 and 22 cm) were compared. Different ion fragments
1617 were shot in the center of the crystal block: Helium, Lithium, Beryllium, Boron, Carbon, Nitrogen
1618 and Oxygen. The studies were performed for several energies in a range of [100-350] MeV, but for
1619 brevity only one fragment results is reported as an example. Must be reminded that the calorimeter
1620 must be fully efficient for fragment with $Z \geq 3$.

1621 In Fig. 61 the energy deposited in the mono-block calorimeter for 200 MeV/u ^{12}C (Right) and
1622 300 MeV/u ^7Li (Left) fragments is shown. Up to now, no detector efficiency has been implemented
1623 in the simulation, energy resolution is assumed 100%. The deposit energy for the Carbon ion
1624 configuration with all the studied crystal lengths and for the Lithium in the 14 and 22 cm long
1625 crystals presents a narrow peak at the nominal kinetic energy of the fragment (respectively 2400
1626 MeV = 200 MeV/u, 2100 MeV = 300 MeV/u) and a tail distribution corresponding to those events
1627 where some energy escapes from the calorimeter. This lost of energy depends on the calorimeter
1628 containments thus on the crystal length, as it can be seen in comparing the 7 cm (magenta), 14
1629 cm (blue) and 21 cm (green) distributions. For what concerns the 7 cm crystal it is clear that for
1630 the Lithium, light fragment, a non-containment effect occurs. The non containment in the shortest
1631 crystals has been observed for most of light fragments. Therefore, a configuration with crystals of
1632 a minimum length of 14 cm is preferable.

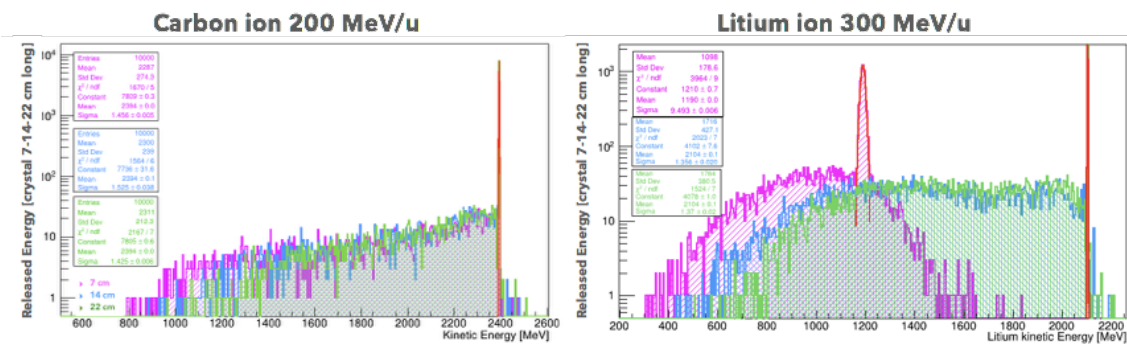


Figure 61 – Total energy deposited in the calorimeter for three different crystal lengths 7 cm (magenta), 14 cm (blue) and 21 cm (green). Simulation performed with 200 MeV/u monochromatic ^{12}C fragments.

1633 Then the kinetic energy escaping form the calorimeter was studied for different fragments. For
1634 the same sample (200 MeV/u ^{12}C fragment), the contribution of the neutrons (left) and protons
1635 (right) for the three different crystal lengths is shown in Fig. 62. It can be noticed that the main
1636 contribution is due to the neutron component; however the length of the crystal does not seem
1637 to be relevant for neutrons, while for the charged component the crystal of 14 cm performs much
1638 better than the 7 cm one.

1639 In order to easily compare the performances for the different length setups, a cumulative energy
1640 distribution has been introduced. In Fig. 63 the energy released in the crystal normalized to the

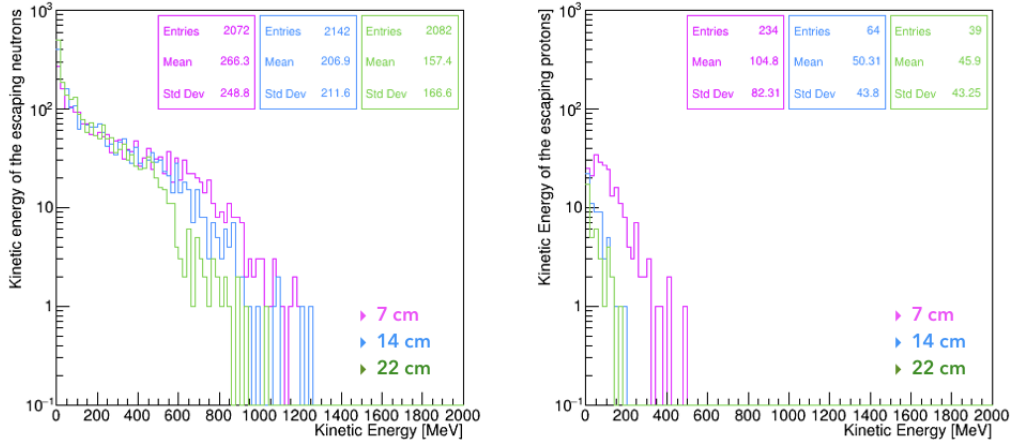


Figure 62 – Kinetic energy of escaping neutrons (Left) and protons (Right) for 200 MeV/u monochromatric ¹²C fragments. Crystal lengths 7 cm (magenta), 14 cm (blue) and 21 cm (green).

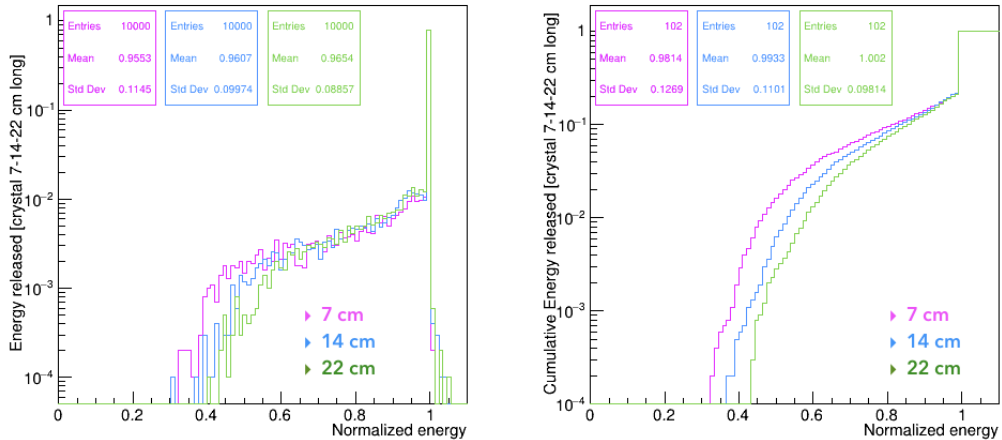


Figure 63 – Normalized (Left) and cumulative (Right) energy released in the crystal for ¹²C fragment at 200 MeV/u. Crystal lengths 7 cm (magenta), 14 cm (blue) and 21 cm (green)

¹⁶⁴¹ ¹²C nominal energy (left) and the cumulative energy distribution (right) are shown.

¹⁶⁴² Despite the absence of detector efficiency does not allow to observe any length effect in the
¹⁶⁴³ main peak the containment for the 7 cm BGO crystal is not adequate. From these studies, and
¹⁶⁴⁴ the comparison with other fragments results, we can conclude that the use of a 14 cm BGO has
¹⁶⁴⁵ to be favored.

¹⁶⁴⁶ 8.3.2. Calorimeter fragments study

¹⁶⁴⁷ The full simulation of the FOOT experiment has been used to characterize the events expected
¹⁶⁴⁸ to reach the calorimeter (see section 4.5 for the calorimeter detailed description) performing in
¹⁶⁴⁹ particular single and multiple-fragments events produced in ¹²C 200 MeV/u beam on the C₂H₄
¹⁶⁵⁰ target.

¹⁶⁵¹ The probability of multiple-fragments is crucial for a proper reconstruction of the energy deposit
¹⁶⁵² and to define the segmentation needed in the calorimeter.

¹⁶⁵³ For multiple-fragments events, in Fig. 64 it is shown the distance between two fragments at
¹⁶⁵⁴ the entrance face of the calorimeter. The mean distance is about 12 cm. Given the size of a
¹⁶⁵⁵ single BGO crystal (2 cm), we can also assume that only ~3% of the events will present multiple-

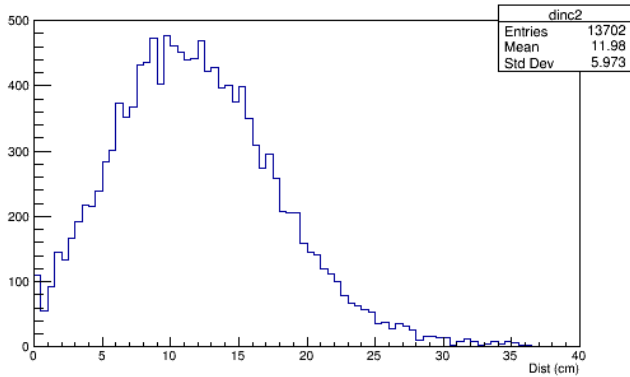


Figure 64 – Mean distance between fragments at calorimeter entrance face.

fragments impinging on two adjacent crystals. The number of crystals involved in the detection of the produced fragments is shown in Fig. 65. It can be noticed that only a very small fraction of events occurs in a single crystal, while most of the events with multiple fragments implies at least two crystals.

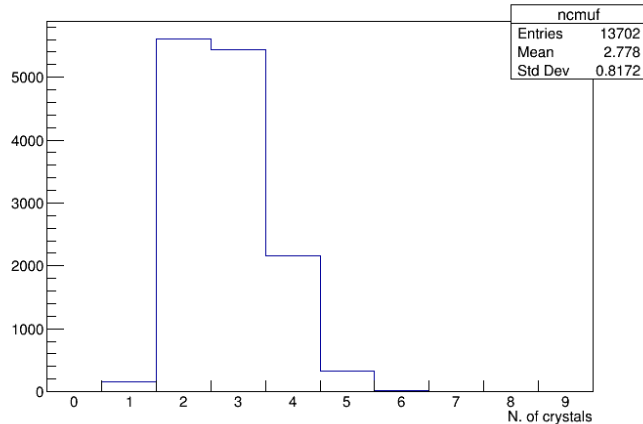


Figure 65 – Number of crystals hit by more than one fragment in multi-fragments events.

A fragment species study has been performed for single fragment events in order to characterize the topology of the expected events. As an example, in Fig. 66 it is plotted the energy deposition for fragments of different A. As it is clear the only A information (mass) is not unique in identifying the fragment: i.e. for A=4 (green line) we can observe two populations, the first with a peak at 0.1 GeV and a second one peaking at 0.4 GeV, corresponding respectively to ^3H ($Z=1$) and ^3He ($Z=2$) fragments.

The most abundant components are hydrogen (1H, black line), helium (4He, blue line) and carbon (^{11}C , brown line) fragments. The typical deposit energy for the different fragment species ranges from few MeV up to 2 GeV. This dynamic range has to be taken into account in the definition of the optimal size and segmentation parameter.

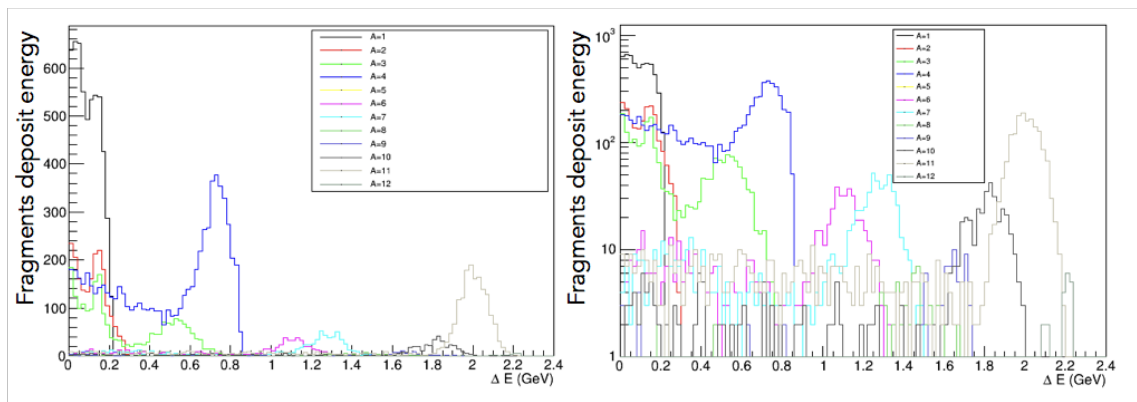


Figure 66 – Fragment species study. For each fragment the deposit energy is shown in a different color in linear (Left) and in log (Right) scale.

Fragment	^1H	^4He	^7Li	^9Be	^{11}B	^{12}C	^{14}N	^{16}O
Z	1	2	3	4	5	6	7	8
A	1	4	7	9	11	12	14	16

Table 6 – List of the considered secondary fragments

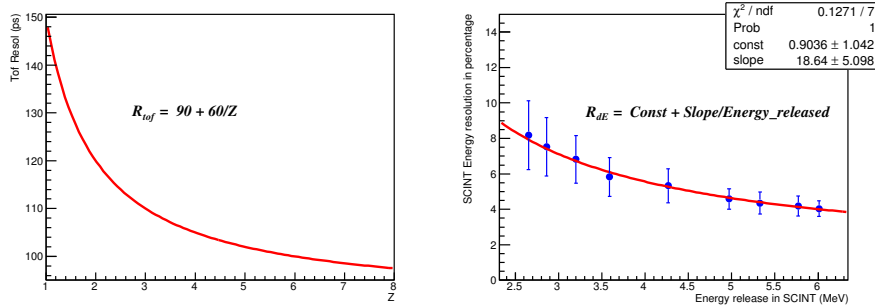


Figure 67 – TOF (Left) and ΔE (Right) resolutions applied to the simulated data.

8.4. Particle identification

The first goal for the cross section measurement of the produced fragments is their correct identification through the determination of its atomic (Z) and mass number (A). The performances have been obtained from simulated events with the detector geometry described in section 3, analyzing 2.3×10^5 events (corresponding to 20 millions of incident particles) coming from the interaction of ^{16}O with 200 MeV/u on a C_2H_4 target. The analysis has been finalized on the study of the most frequent produced fragments listed in Tab. 6.

All the quantities necessary for the $Z - A$ fragment identification derive from the time of flight (TOF), the momentum (p), the energy release (ΔE) and the kinetic energy (E_k).

The time of flight TOF is the interval time between the signal from the Start Counter and the one from the plastic scintillator after the subtraction of the time necessary to the beam to cover the distance between the Start Counter and the target.

8.4.1. Charge identification

The TOF resolution has been obtained by the performance measured during a test beam; it has been parametrized as a function of Z as shown in Fig. 67 and it corresponds to a percentage resolution in the range [1.8,2.4]%. The $\beta (= v/c)$ of the fragment is derived from TOF and the trajectory length of the track.

The momentum reconstruction p has been determined by applying a gaussian smearing of 5% to the one generated independent on the momentum and types of fragments, as suggested by the results of Sec. 8.2.1

The energy release ΔE crossing a material has been reconstructed by the energy deposited in the plastic scintillator; the ΔE resolution has been parametrized as a function on the deposited energy (see Fig. 67) and limited to the range [3 – 10]% as obtained at the already cited test beam.

The kinetic energy E_k has been reconstructed by adding the energy deposition in the plastic scintillator and in the calorimeter. The resolution on the deposited energy in the calorimeter has been obtained by a fixed gaussian smearing of 1.5% independent on the energy deposition. At the moment, it has been considered only the deposited energy of the primary fragment.

The resolution on the $Z - A$ identification is strongly dependent both on the energy loss by fragments due to ionization processes before reaching the calorimeter and the leakage inside it mostly due to neutron emission. The percentage of events with energy loss is reported in Fig. 68 showing, for each kind of fragment, the distribution of the ratio between the deposited energy with

Fragment	^1H	^4He	^7Li	^9Be	^{11}B	^{12}C	^{14}N	^{16}O
Peak position	0.988	0.991	0.989	0.986	0.983	0.978	0.975	0.972

Table 7 – Ratio between the deposited energy in the plastic scintillator and in the calorimeter to the generated kinetic energy of the simulated fragments. The error associated to the value is one on the least significant digit.

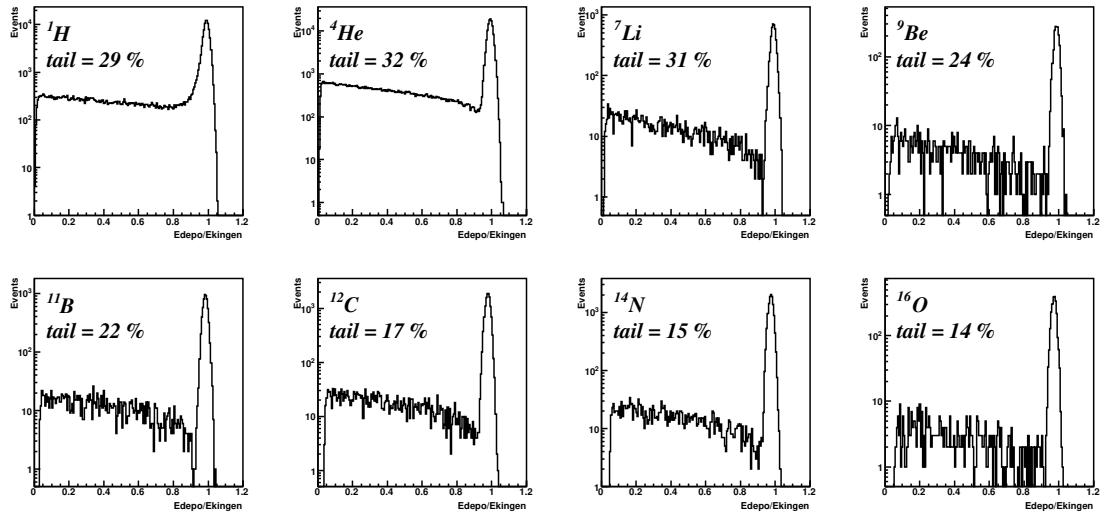


Figure 68 – Ratio between the sum of the deposited energy in the plastic scintillator and in the calorimeter with respect to the generated kinetic energy of the simulated fragments.

respect to the generated kinetic energy: an event is defined to belong to the tail if the deposited energy is less than 90% of the generated kinetic energy. The final resolution on the A determination is also affected by the shift of the peak position also reported in Tab. 7, where the uncertainty is on the least significant digit. This shift is due to the overall energy loss in the detector materials and is fragment dependent. In the final configuration, the problem will be fixed with an appropriate energy calibration of both the plastic scintillator and the calorimeter, at the moment not yet applied.

For all these reasons it is necessary to have a redundant detector capable to reconstruct and to identify those events where the final state has undergone an interaction before reaching the calorimeter, or when part of the energy has not been recovered because of neutrons emission or other mechanisms leading to invisible energy release.

The performances have been obtained by selecting only tracks travelling all the detector length. In the energy range of the produced fragments, the Z determination is obtained by the mean energy loss ΔE of charged particle when travelling a distance dx in a medium, expressed by the Bethe formula:

$$-\frac{dE}{dx} = \frac{\rho \cdot Z}{A} \frac{4\pi N_A m_e c^2}{M_U} \left(\frac{e^2}{4\pi\epsilon_0 m_e c^2} \right)^2 \frac{z^2}{\beta^2} \left[\ln \left(\frac{2m_e c^2 \beta^2}{I \cdot (1 - \beta^2)} \right) - \beta^2 \right] \quad (5)$$

where

- ρ , Z , A and I are respectively the density, the atomic number, the mass number and the mean excitation potential of the crossed medium;
- N_A , M_U , m_e and c are respectively the Avogadro number, the molar mass constant, the electron mass and the speed of light;

- 1721 • $\frac{e^2}{4\pi\epsilon_0 m_e c^2}$ is the classical electron radius ($\simeq 2.818 \text{ fm}$) ;
- 1722 • Z , β are respectively the atomic number (or more simply the charge) and the velocity of the
1723 fragment divided by the speed light.

1724 The main detector dedicated to the Z determination is the plastic scintillator described in section
1725 focused on the measurement of the energy deposit and the TOF for the β determination.
1726 The Z determination is presented in Fig. 69 for all the studied fragments; the peaks result well
1727 distinguished from each other, allowing a clear charge identification. The Z resolution improves
1728 with increasing fragment charge, passing from 6% for ${}^1\text{H}$ to 2% for ${}^{16}\text{O}$. A shift with respect the
1729 expected position is present (see Tab. 8 and 9). A possible explanation is the lack of energy due to
1730 neutron emission (see Tab. 7). At the moment this is under further investigation. An improvement
1731 of the Z identification performances will be obtained combining the ΔE measurement of the plastic
1732 scintillators with the ΔE information from the Micro Strip Detector (see Fig. 28). However we
1733 do not add this information in the Z analysis without a reliable estimate of the ΔE resolution of
1734 the MSD. As a consequence the estimated Z resolutions could be an lower bound to the achievable
1735 resolutions.

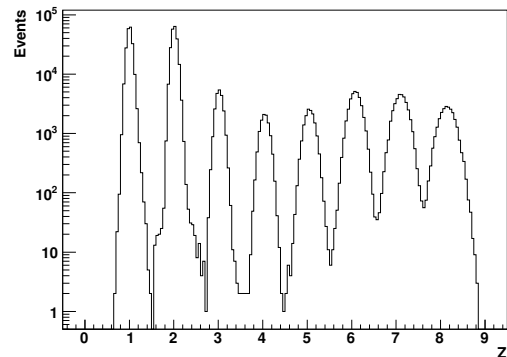


Figure 69 – Determination of charge number Z for all the studied fragments.

Fragment	${}^1\text{H}$	${}^4\text{He}$	${}^7\text{Li}$	${}^9\text{Be}$	${}^{11}\text{B}$
z	1	2	3	4	5
Reconstructed z	1.01 ± 0.06	2.01 ± 0.07	3.02 ± 0.08	4.05 ± 0.10	5.06 ± 0.12

Table 8 – Reconstructed Z for the studied fragments with $Z < 6$: the error associated to the mean value is the σ of the gaussian fit.

Fragment	${}^{12}\text{C}$	${}^{14}\text{N}$	${}^{16}\text{O}$
z	6	7	8
Reconstructed z	6.08 ± 0.14	7.11 ± 0.16	8.15 ± 0.18

Table 9 – Reconstructed Z for the studied fragments with $Z > 5$: the error associated to the mean value is the σ of the gaussian fit.

1736 8.4.2. Mass identification

1737 The redundancy of sub-detectors in FOOT is crucial because it allows to determine the mass
1738 number A in different ways. In particular:

- 1739 • through the simultaneous determination of β and p respectively from the TOF and the
 1740 tracking system:

$$A_1 = \frac{p}{U \beta c\gamma} \quad (6)$$

1741 where $\gamma = 1/\sqrt{1-\beta^2}$ and U is the Unified Atomic Mass (≈ 931.5 MeV).

- 1742 • through the simultaneous determination of β and E_k respectively from the TOF and the
 1743 calorimeter:

$$A_2 = \frac{E_k}{U \cdot c^2 (\gamma - 1)} \quad (7)$$

- 1744 • through the simultaneous determination of p and E_k respectively from the tracking system
 1745 and the calorimeter:

$$A_3 = \frac{p^2 c^2 - E_k^2}{2 \cdot U \cdot c^2 E_k} \quad (8)$$

1746 The three different A determinations exhibit an obvious correlation because of the presence
 1747 of a common sub-detector for each couple of A definition. The distributions of the reconstructed
 1748 mass number using the three different modes A_1 , A_2 and A_3 are respectively presented in Fig. 70,
 1749 71 and 72.

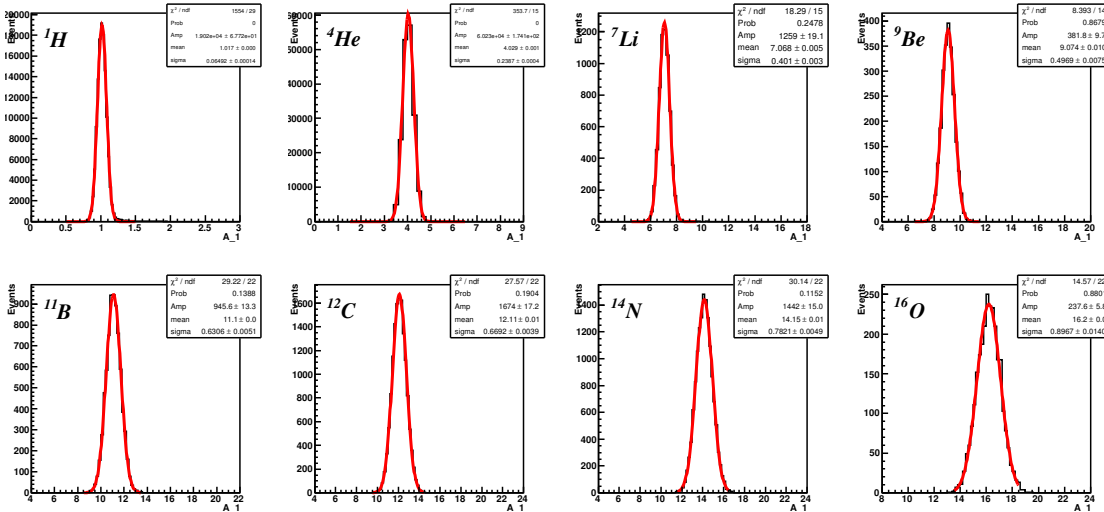


Figure 70 – Determination of mass number A by means of the only information from TOF and tracking system.

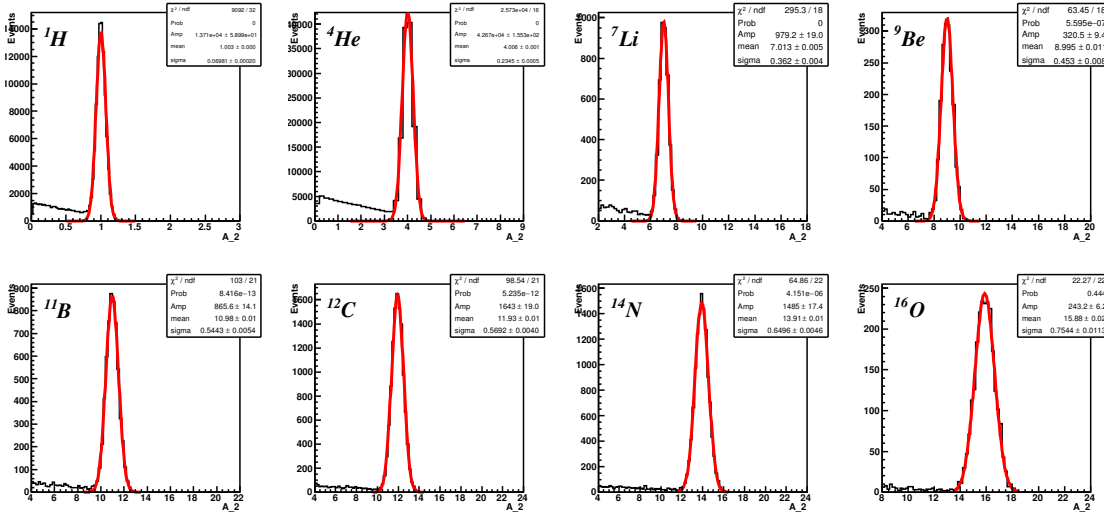


Figure 71 – Determination of mass number A by means of the only information from TOF and calorimeter.

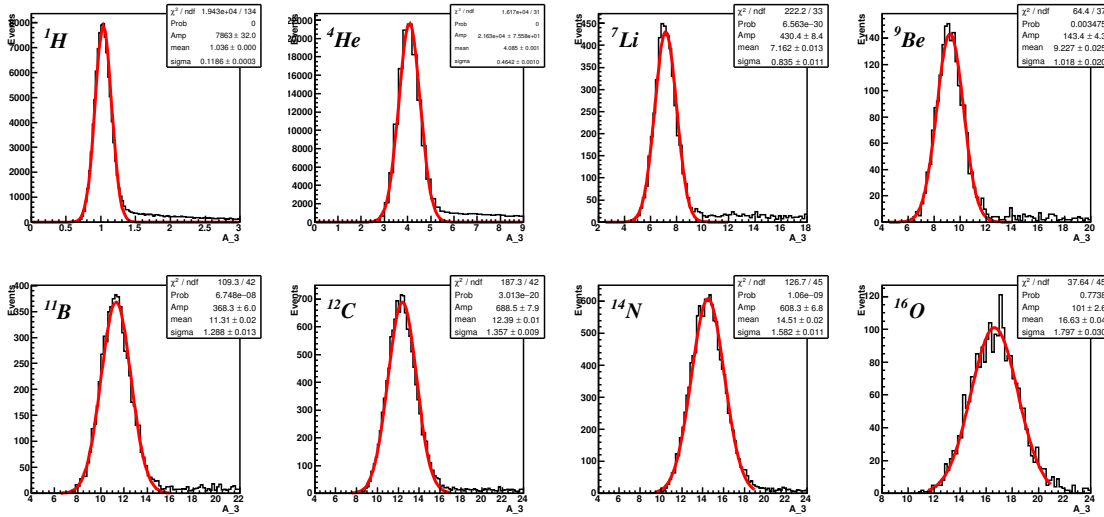


Figure 72 – Determination of mass number A by means of the only information from tracking system and calorimeter.

The peak position and the resolution of the A_1 , A_2 and A_3 quantities (respectively the μ and the σ of the gaussian fit) are given in Tab. 10 and 11). Some general remarks can be summarized as follows:

- the peak position is centered around the expected values with in some cases a shift completely included in the resolution;
- the resolution is $\approx 5\%$ for A_2 and slightly worst for A_1 reconstruction modes, while it is a bit larger than 10% in the A_3 case. These resolutions depend on the input smearing applied to the time of flight, momentum and kinetic energy reconstruction. The calorimeter is the detector that suffers for the energy leakage.
- A_2 and A_3 present a correlated tail at low and high values respectively, dependent on the energy leakage especially from neutron emission inside the calorimeter.

Fragment	^1H	^4He	^7Li	^9Be	^{11}B
A_1	1.02 ± 0.06	4.03 ± 0.24	7.07 ± 0.40	9.07 ± 0.50	11.10 ± 0.63
A_2	1.00 ± 0.07	4.01 ± 0.23	7.01 ± 0.36	8.99 ± 0.45	10.98 ± 0.54
A_3	1.0 ± 0.1	4.1 ± 0.5	7.2 ± 0.8	9.2 ± 1.0	11.3 ± 1.3

Table 10 – Peak value and resolution of the A_1 , A_2 and A_3 mass number for the studied fragments with $Z < 6$.

Fragment	^{12}C	^{14}N	^{16}O
A_1	12.11 ± 0.67	14.15 ± 0.78	16.20 ± 0.90
A_2	11.93 ± 0.57	13.91 ± 0.65	15.88 ± 0.75
A_3	12.4 ± 1.4	14.5 ± 1.6	16.6 ± 1.8

Table 11 – Peak value and resolution of the A_1 , A_2 and A_3 mass number for the studied fragments with $Z > 5$.

The strategy used for the best determination of A considers two different fit procedures:

- a standard χ^2 minimization approach;
- An Augmented Lagrangian method (*ALM*) approach.

The standard approach uses a χ^2 minimization method based on a function f defined as:

$$f = \left(\frac{\text{TOF} - T}{\sigma_{\text{TOF}}} \right)^2 + \left(\frac{p - P}{\sigma_p} \right)^2 + \left(\frac{E_k - K}{\sigma_{E_k}} \right)^2 + \\ (A_1 - A, \quad A_2 - A, \quad A_3 - A) \begin{pmatrix} B_{00} & B_{01} & B_{02} \\ B_{10} & B_{11} & B_{12} \\ B_{20} & B_{21} & B_{22} \end{pmatrix} \begin{pmatrix} A_1 - A \\ A_2 - A \\ A_3 - A \end{pmatrix} \quad (9)$$

where TOF , p , E_k , A_1 , A_2 and A_3 are the reconstructed quantities, σ_{TOF} , σ_p , σ_{E_k} are the uncertainties, T , P , K and A are the fit output parameters. The evaluation of the uncertainties associated to A_1 , A_2 and A_3 has to take into account their correlation which is generically expressed by the matrix B , related to the correlation matrix C by the function $B = (C \cdot C^T)^{-1}$. The correlation matrix C is expressed as:

$$C = \begin{pmatrix} \frac{\partial A_1}{\partial T} dT & \frac{\partial A_1}{\partial P} dP & 0 \\ \frac{\partial A_2}{\partial T} dT & 0 & \frac{\partial A_2}{\partial K} dK \\ 0 & \frac{\partial A_3}{\partial P} dP & \frac{\partial A_3}{\partial K} dK \end{pmatrix} \quad (10)$$

The ALM approach performs a constrained minimization in a large parameter space. All the details of the method can be find in [100]. Here only the basilar points are recalled, to allow a better comprehension of the text. The method minimizes a Lagrangian function L expressed by:

$$L(\vec{x}, \lambda, \mu) \equiv f(\vec{x}) - \sum_a \lambda_a c_a(\vec{x}) + \frac{1}{2\mu} \sum_a c_a^2(\vec{x}) \quad (11)$$

where f , in analogy with the standard χ^2 method, is defined as:

$$f(\vec{x}) = \left(\frac{\text{TOF} - T}{\sigma_{\text{TOF}}} \right)^2 + \left(\frac{p - P}{\sigma_p} \right)^2 + \left(\frac{E_k - K}{\sigma_{E_k}} \right)^2 \quad (12)$$

both the summation runs over the three constraints (A_1 , A_2 and A_3) with the relation:

$$\sum_a \lambda_a c_a(\vec{x}) + \frac{1}{2\mu} \sum_a c_a^2(\vec{x}) = \lambda_1 (A_1 - A) + \lambda_2 (A_2 - A) + \lambda_3 (A_3 - A) + \frac{1}{2\mu} ((A_1 - A)^2 + (A_2 - A)^2 + (A_3 - A)^2) \quad (13)$$

where λ are variable Lagrange multiplier parameters, while μ is the penalty term fixed to 0.1. The use of a penalty term forces the fit to give more strength to the constraints: the lower is μ the greater is the effect of the constraints.

The results on the mass number determination A , as obtained by the standard χ^2 and *ALM* methods, are presented in Fig. 73 and 74 respectively. The two methods give similar results: the peak positions are centered around the expected values without significant shifts and the resolution improves for increasing fragment mass, passing from 6% for 1H to 4.2% for ^{16}O . Such resolution values are comparable to the best results obtained with the direct measurements of A , but at the moment no cut on χ^2 has been requested. Obviously, a significant tail of badly reconstructed mass number A is visible also in these fit procedures, due to the already mentioned energy leakage.

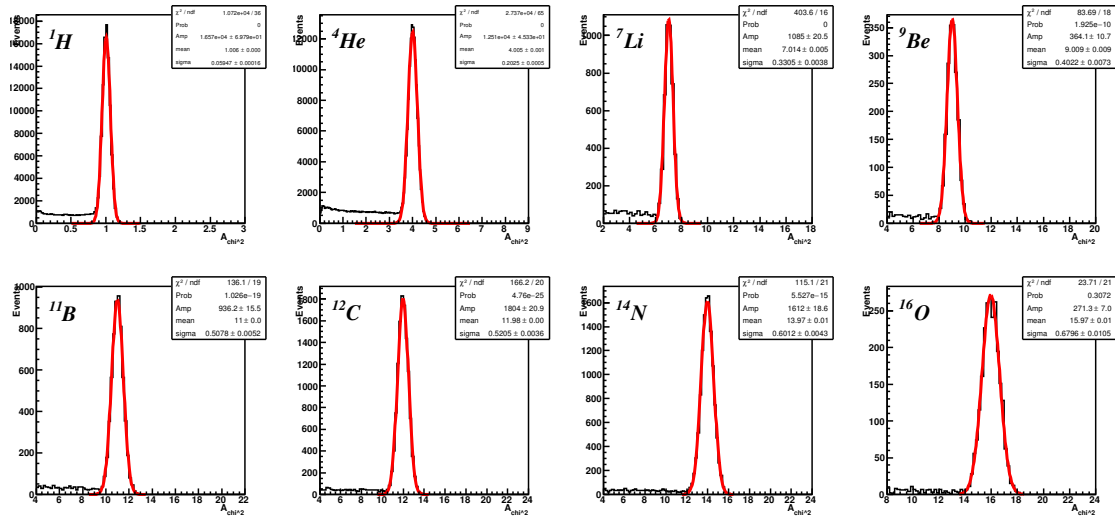


Figure 73 – Determination of mass number A with the standard χ^2 method fit.

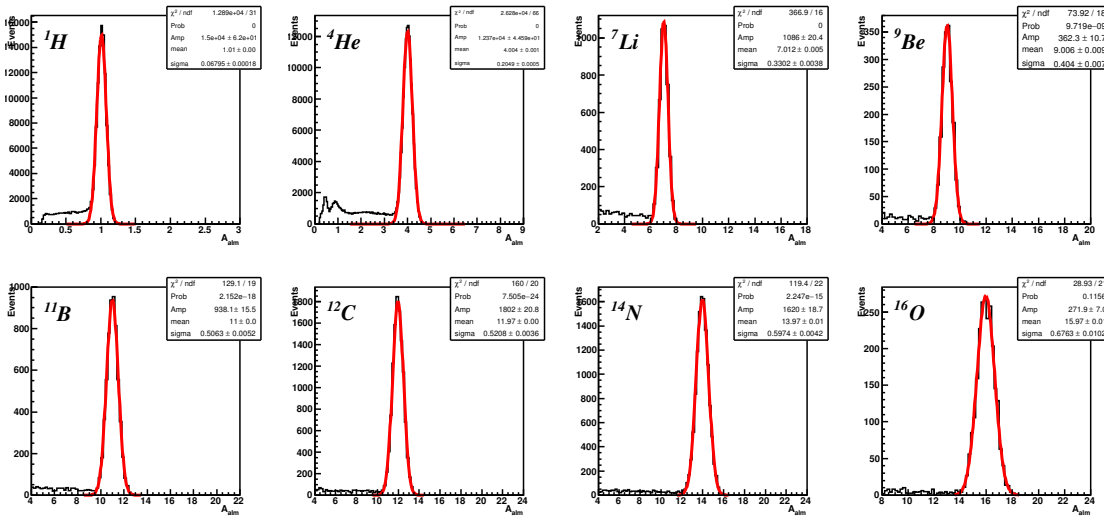


Figure 74 – Determination of mass number A by means of the Augmented Lagrangian Method fit.

Fragment	^1H	^4He	^7Li	^9Be	^{11}B
A_{χ^2}	1.01 ± 0.06	4.00 ± 0.20	7.01 ± 0.33	9.01 ± 0.40	11.00 ± 0.51
A_{alm}	1.01 ± 0.07	4.00 ± 0.20	7.01 ± 0.33	9.01 ± 0.40	11.00 ± 0.51

Table 12 – Peak value and resolution of the A_{χ^2} and A_{alm} mass number for the studied fragments with $Z < 6$.

Fragment	^{12}C	^{14}N	^{16}O
A_{χ^2}	11.98 ± 0.52	13.97 ± 0.60	15.97 ± 0.68
A_{alm}	11.97 ± 0.52	13.97 ± 0.60	15.97 ± 0.68

Table 13 – Peak value and resolution of the A_{χ^2} and A_{alm} mass for the studied fragments with $Z > 5$.

1788 The average number of mass A and its resolution (peak position and σ of a gaussian fit) are
1789 listed in Tab. 12 and Tab. 13 for the two fit methods.

1790 The χ^2 distributions of the two fit methods are very close one to each other and only the one
1791 referred to the ALM fit is reported in Fig. 75.

1792 The correlation between the badly reconstructed A , belonging to the tail, and the χ^2 value of
1793 the fits is clearly demonstrated in Fig. 76 and 77 for the standard χ^2 and the ALM fit procedures
1794 respectively.

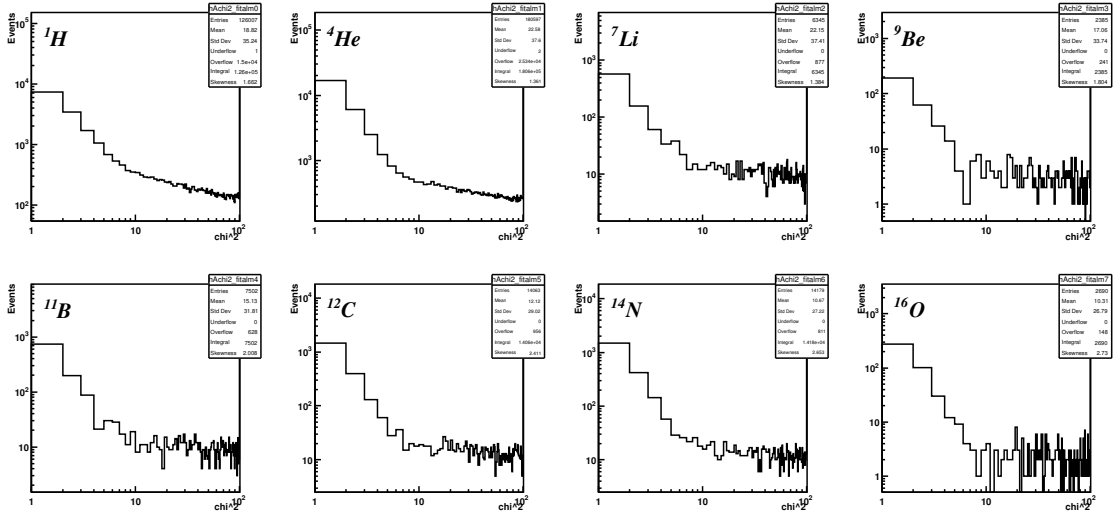


Figure 75 – χ^2 distributions of the ALM fit.

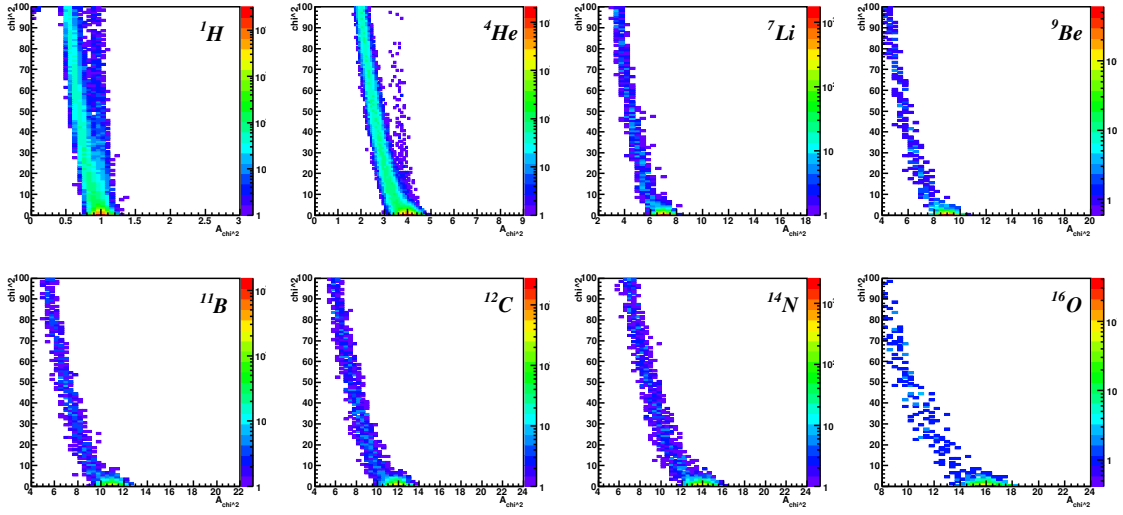


Figure 76 – χ^2 value as a function of the determined mass number A with the standard χ^2 minimization.

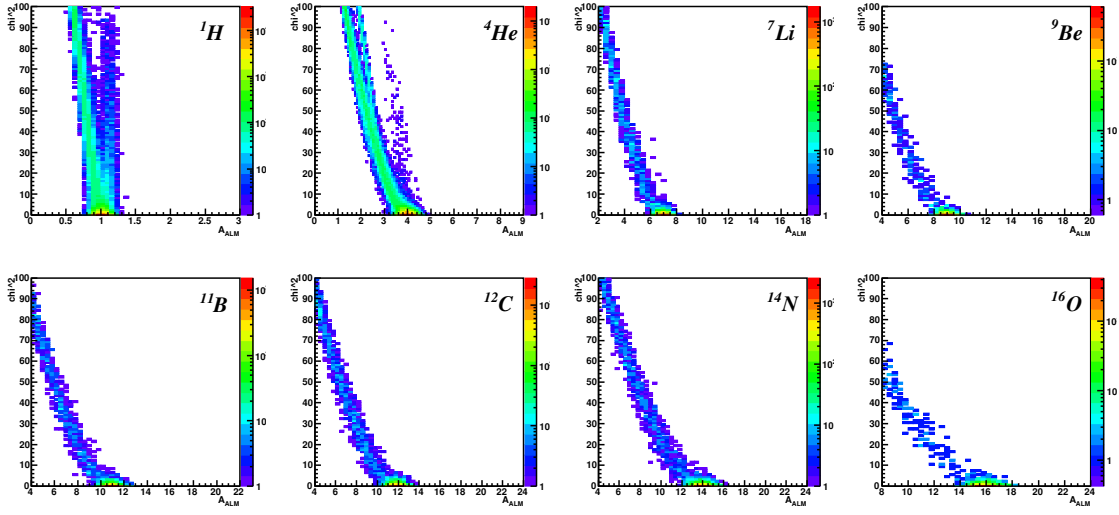


Figure 77 – χ^2 value as a function of the determined mass number A with the Augmented Lagrangian Method fit.

1795 The events having a badly reconstructed mass number A can be identified and excluded by
 1796 requiring a χ^2 cut: in Fig. 78 and 79 the A distributions are reported after the application of a
 1797 $\chi^2 < 5$ cut for both fit methods. The value of the χ^2 cut has been chosen in order to have an
 1798 average decrease of the initial statistics by $\approx 20\%$ for the heavier fragments ($Z > 3$).

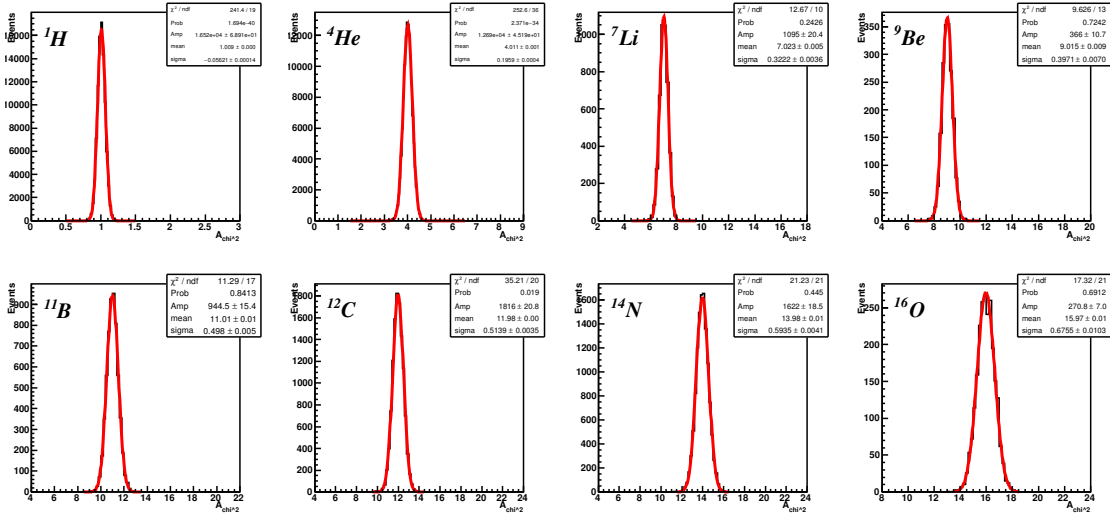


Figure 78 – A determination with the standard χ^2 method fit applying a $\chi^2 < 5$ cut.

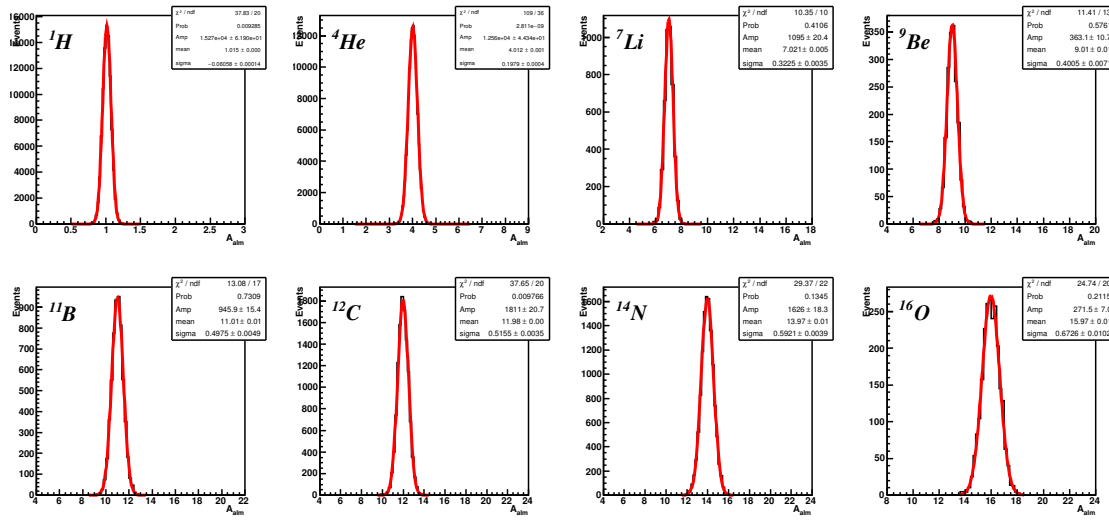


Figure 79 – A determination with the Augmented Lagrangian Method fit applying a $\chi^2 < 5$ cut.

The average A values and their resolutions are reported in Tab. 14 and Tab. 15.

Fragment	^1H	^4He	^7Li	^9Be	^{11}B
A_{χ^2}	1.01 ± 0.06	4.01 ± 0.20	7.02 ± 0.32	9.02 ± 0.40	11.01 ± 0.50
A_{alm}	1.02 ± 0.06	4.01 ± 0.20	7.02 ± 0.32	9.01 ± 0.40	11.01 ± 0.50

Table 14 – Peak value and resolution of the A_{χ^2} and A_{alm} mass number for the studied fragments with $Z < 6$ and applying a $\chi^2 < 5$ cut.

Fragment	^{12}C	^{14}N	^{16}O
A_{χ^2}	11.98 ± 0.51	13.98 ± 0.59	15.97 ± 0.68
A_{alm}	11.98 ± 0.52	13.98 ± 0.59	15.97 ± 0.67

Table 15 – Peak value and resolution of the A_{χ^2} and A_{alm} mass number for the studied fragments with $Z > 5$, applying a $\chi^2 < 5$ cut.

In order to summarize the results on the performances of the all methods for the A determination of each fragment, the percentage of the relative deviation of the measured quantity with respect the reconstructed one has been evaluated by analysing the distribution of the variable $(A_{meas} - A_{gen})/A_{meas} * 100$. Fitting these distributions with a gaussian function it is possible to appreciate a shift with respect to the correct value and to determine the resolution for each adopted method. Fig. 80 shows the percentage of the relative deviation and the resolution of all the methods: the first three colours, black, light blue and violet, correspond respectively to the A_1 , A_2 and A_3 reconstruction methods. The remaining colours refer to the two fit procedures. In particular: green and magenta correspond respectively for the standard χ^2 and ALM fit methods without any cuts, while dark blue and red correspond respectively to the standard χ^2 and ALM fit methods with the additional request of $\chi^2 < 5$. The two fit methods give similar results. The additional request of a χ^2 cut (the dark blue and the red points) allows to exclude the events with a bad A determination and provides the most precise results. The percentage shift on the A determination is $\approx 0.5\%$. The resolution is $\approx 4\%$ for the heavier fragments and close to 5% for the lighter ones. These results, together with the one on Z determination (see Fig. 69), assure a

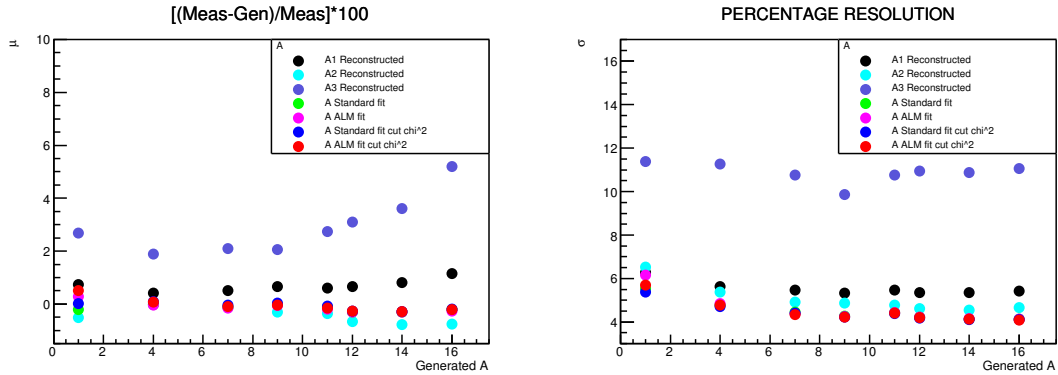


Figure 80 – Percentage deviation $(A_{meas} - A_{gen})/A_{meas}$ and resolution of A for each fragment with respect the generated A . Black, light blue and violet colours are respectively used for the A_1 , A_2 and A_3 reconstruction methods. The other colours are related to the two fit procedures, in particular: green and magenta represent respectively the standard χ^2 and ALM fit methods without any cuts, while dark blue and red are respectively used for the standard χ^2 and ALM fit methods adding the request $\chi^2 < 5$.

complete isotopic identification of these selected fragments.

The fit procedure provides also the best determination of the kinematic quantities of the fragments necessary for the differential cross section determination. In Fig. 81 and 82 are respectively represented the percentage deviation and the resolution of the output fit parameters time of flight (T), the momentum (P) and the kinetic energy (K). As in the previous case, the two fit methods provide similar results and the best performances are obtained with the additional cut on the χ^2 (the dark blue and red points). The resolution improvement, with respect to the one on the fixed reconstructed quantities, is significant (see Fig.82). In particular:

- the input resolution on TOF was in the range [1.8,2.4]%, while, after the fit procedure, an improvement by about 10% is achieved for each fragment;
- the input resolution on the momentum (p) was fixed at 5%, while, after the fit procedure, there is an average improvement of about 40% for each fragment;
- the input resolution on the kinetic energy (E_k) was fixed at 1.5% for the energy deposited in the calorimeter and was in the range [3,10]% for the one deposited in the scintillator. After the fit procedure it improves of about 5% for each fragment.

The percentage deviation of the measured momentum and kinetic energy exhibits a shift, in particular for the heavier fragments (see Fig. 81). This is probably due to the already cited neutron emission (see Fig.. 68 and Tab. 7) and at the moment is under investigation.

The A reconstruction efficiency of the different methods has been evaluated for each fragment by counting the events under the gaussian peak (see Figs. 70, 71, 72, 73, 74, 78 and 79) with respect to the total number of fragments that reach the calorimeter. Fig. 83 shows the results: as expected, the efficiency with the reconstructed method A_1 results the higher one, because it is not affected by the energy leakage in the calorimeter and the momentum reconstruction only includes a smearing of its value. The other methods are more realistic and have similar efficiency, which results about 80% for the heavier fragments and has an average of 70% for the lighter ones.

8.4.3. Systematic study on the resolution of the atomic mass number A

The atomic mass number A , as output of the fit procedure, depends on the resolutions achieved on the measurements of the time of flight TOF , the momentum p and the kinetic energy (E_k). To understand which detectors mostly affect the precision on the A determination, a systematic study

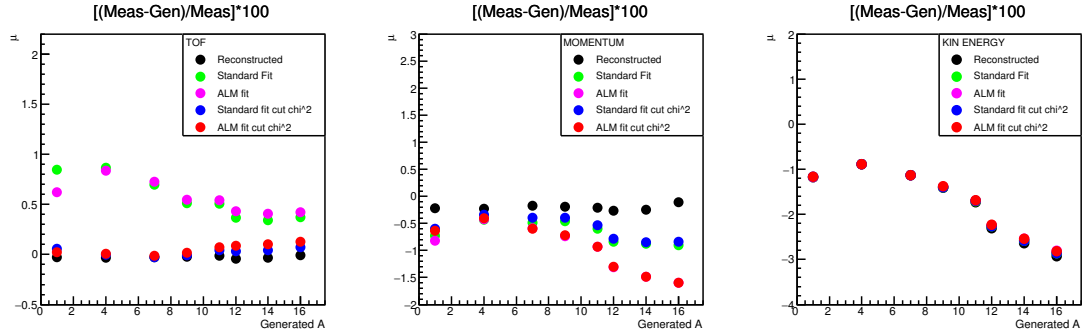


Figure 81 – Percentage deviation $(X_{meas} - X_{gen})/X_{meas}$ of TOF, momentum and kinetic energy for each fragment with respect the generated A . Black colour refers to the reconstructed quantity, while the other colours are related to the two different fit procedures. In particular: green and magenta are respectively used for the standard χ^2 and ALM fit methods without any cut, while dark blue and red are respectively used for the standard χ^2 and ALM fit methods with the additional $\chi^2 < 5$ request.

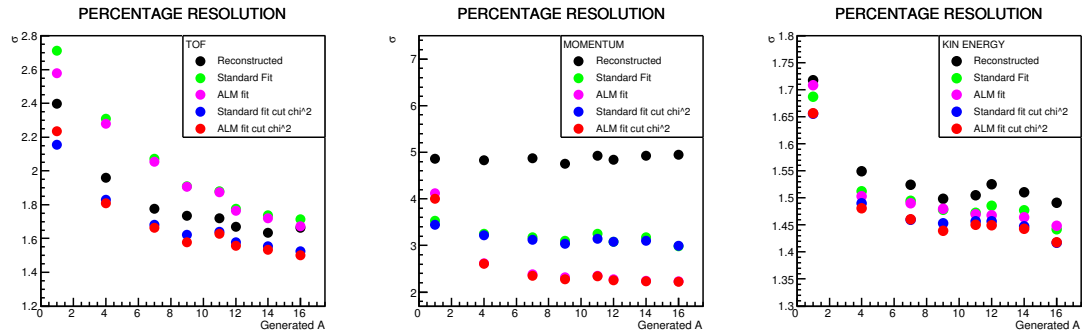


Figure 82 – Percentage resolution of TOF, momentum and kinetic energy for each fragment with respect the generated A . Black colour refers to the reconstructed quantity, while the other colours are related to the two fit procedures, in particular: green and magenta are respectively used for the standard χ^2 and ALM fit methods without any cut, while dark blue and red are respectively used for the standard χ^2 and ALM fit methods with the additional $\chi^2 < 5$ request.

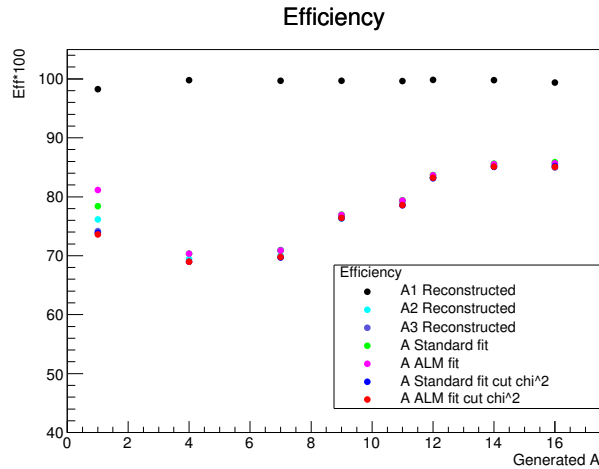


Figure 83 – Percentage reconstruction efficiency for each method and for each fragment. Black, light blue and violet colours are respectively used for the A_1 , A_2 and A_3 reconstruction. The other colours are related to the two fit procedures, in particular: green and magenta correspond respectively to the standard χ^2 and ALM fit methods without any cuts, while dark blue and red correspond respectively to the standard χ^2 and ALM fit methods with the additional $\chi^2 < 5$ request.

σ_{TOF} ps	σ_p %	σ_{E_k} %
80	3.5	1.0
100	4.0	1.5
120	5.0	2.0
150	6.0	2.5

Table 16 – Tested resolution values on TOF , p and E_k used to determine the precision on A .

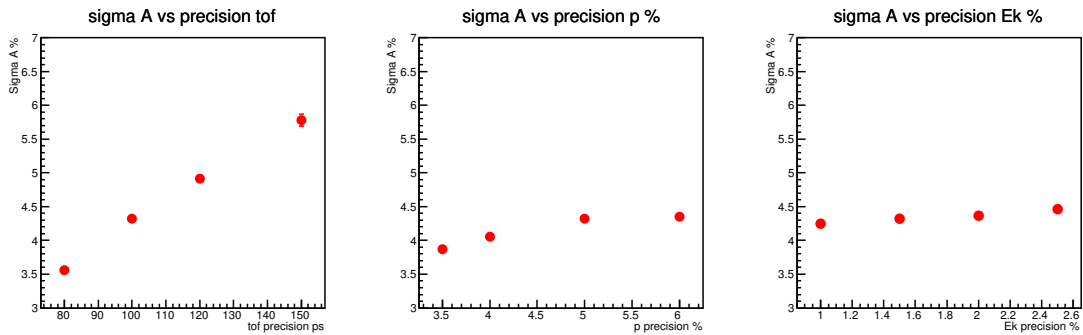


Figure 84 – Resulting percentage precision on the determination of A for the ^{12}C fragment as obtained with the Augmented Lagrangian method approach after the application of a $\chi^2 < 5$ cut. The left plot shows the dependence of σ_A with respect to the TOF resolution, keeping p and E_k at their standard precision (5% and 1.5% respectively). The central plot shows the dependence of σ_A with respect to the p resolution, keeping TOF and E_k at their standard precision (100 ps and 1.5% respectively). The right plot shows the dependence of σ_A with respect to the E_k resolution, keeping TOF and p at their standard precision (100 ps and 5% respectively).

varying the resolution on the TOF , p and E_k has been performed. Also the energy release ΔE in the scintillator enters in the A determination, but it has not been considered, due to the negligible value of the energy released in the plastic scintillator with respect to the one in the calorimeter. To simplify the discussion, we shall present only the results concerning the A determination obtained with the Augmented Lagrangian method approach after the application of a $\chi^2 < 5$ cut and for the only case of ^{12}C fragments. All the results from the other fragments and obtained with different methods scale in the same way. The resolutions tested for the TOF , p and E_k are included in a reasonable range and are reported in Tab. 16. The precision on A has been estimated using a sub-sample (46 k events) of the same simulated data (^{16}O with 200 MeV/u on a C_2H_4 target), anyway sufficient to achieve the necessary accuracy.

All the results from the systematic studies are reported on Tab. 17.

To facilitate the interpretation of the results, in Fig. 84 is reported the dependence of the precision on A separately from the TOF , or p or E_k , keeping the other two variables at the standard precision (respectively 100 ps, 5% and 1.5%). Some general remarks can be underlined:

- the range of resolution on the A determination is [3.3,6.2]%;
- the variation on σ_A as a function of TOF is the steepest one, worsening by about 70% when moving the TOF resolution from 80 to 150 ps.
- the resolution on A depending on the p worsens by about 10% when moving the p precision from 3.5% to 6%.
- the variation on σ_A as a function of E_k is the smallest one, worsening by about 5% when moving the E_k resolution from 1% to 2.5%.

All the results on the systematic studies are also reported in Fig. 85, where the dependences are visualized in three different modes: each one of the three columns of plots corresponds to the

σ_{TOF} ps	σ_p %	σ_{E_k} %	σ_A %	σ_{TOF} ps	σ_p %	σ_{E_k} %	σ_A %
80	3.5	1.0	3.30 ± 0.05	120	3.5	1.0	4.38 ± 0.06
80	3.5	1.5	3.37 ± 0.05	120	3.5	1.5	4.43 ± 0.07
80	3.5	2.0	3.41 ± 0.05	120	3.5	2.0	4.41 ± 0.06
80	3.5	2.5	3.53 ± 0.05	120	3.5	2.5	4.42 ± 0.06
80	4.0	1.0	3.34 ± 0.05	120	4.0	1.0	4.45 ± 0.06
80	4.0	1.5	3.47 ± 0.05	120	4.0	1.5	4.47 ± 0.06
80	4.0	2.0	3.54 ± 0.05	120	4.0	2.0	4.57 ± 0.06
80	4.0	2.5	3.68 ± 0.05	120	4.0	2.5	4.64 ± 0.07
80	5.0	1.0	3.51 ± 0.05	120	5.0	1.0	4.80 ± 0.07
80	5.0	1.5	3.56 ± 0.05	120	5.0	1.5	4.91 ± 0.07
80	5.0	2.0	3.73 ± 0.05	120	5.0	2.0	4.99 ± 0.07
80	5.0	2.5	3.89 ± 0.06	120	5.0	2.5	5.04 ± 0.07
80	6.0	1.0	3.58 ± 0.05	120	6.0	1.0	5.08 ± 0.07
80	6.0	1.5	3.68 ± 0.05	120	6.0	1.5	5.09 ± 0.07
80	6.0	2.0	3.82 ± 0.05	120	6.0	2.0	5.18 ± 0.08
80	6.0	2.5	4.06 ± 0.06	120	6.0	2.5	5.28 ± 0.08
100	3.5	1.0	3.78 ± 0.05	150	3.5	1.0	5.00 ± 0.07
100	3.5	1.5	3.87 ± 0.05	150	3.5	1.5	5.00 ± 0.07
100	3.5	2.0	3.90 ± 0.05	150	3.5	2.0	5.00 ± 0.07
100	3.5	2.5	3.92 ± 0.05	150	3.5	2.5	5.01 ± 0.07
100	4.0	1.0	4.03 ± 0.06	150	4.0	1.0	5.29 ± 0.08
100	4.0	1.5	4.06 ± 0.06	150	4.0	1.5	5.29 ± 0.08
100	4.0	2.0	4.13 ± 0.06	150	4.0	2.0	5.33 ± 0.08
100	4.0	2.5	4.19 ± 0.06	150	4.0	2.5	5.30 ± 0.08
100	5.0	1.0	4.25 ± 0.06	150	5.0	1.0	5.66 ± 0.08
100	5.0	1.5	4.32 ± 0.06	150	5.0	1.5	5.78 ± 0.09
100	5.0	2.0	4.37 ± 0.06	150	5.0	2.0	5.82 ± 0.09
100	5.0	2.5	4.46 ± 0.06	150	5.0	2.5	5.84 ± 0.09
100	6.0	1.0	4.32 ± 0.06	150	6.0	1.0	6.08 ± 0.09
100	6.0	1.5	4.35 ± 0.06	150	6.0	1.5	6.08 ± 0.09
100	6.0	2.0	4.55 ± 0.07	150	6.0	2.0	6.11 ± 0.09
100	6.0	2.5	4.70 ± 0.07	150	6.0	2.5	6.24 ± 0.09

Table 17 – Obtained precision on A as a function of the different resolution on TOF , p and E_k .

1868 resolution when one of the three quantities TOF , p or E_k is maintained constant while the other
1869 two are varied (see the caption for all the details).

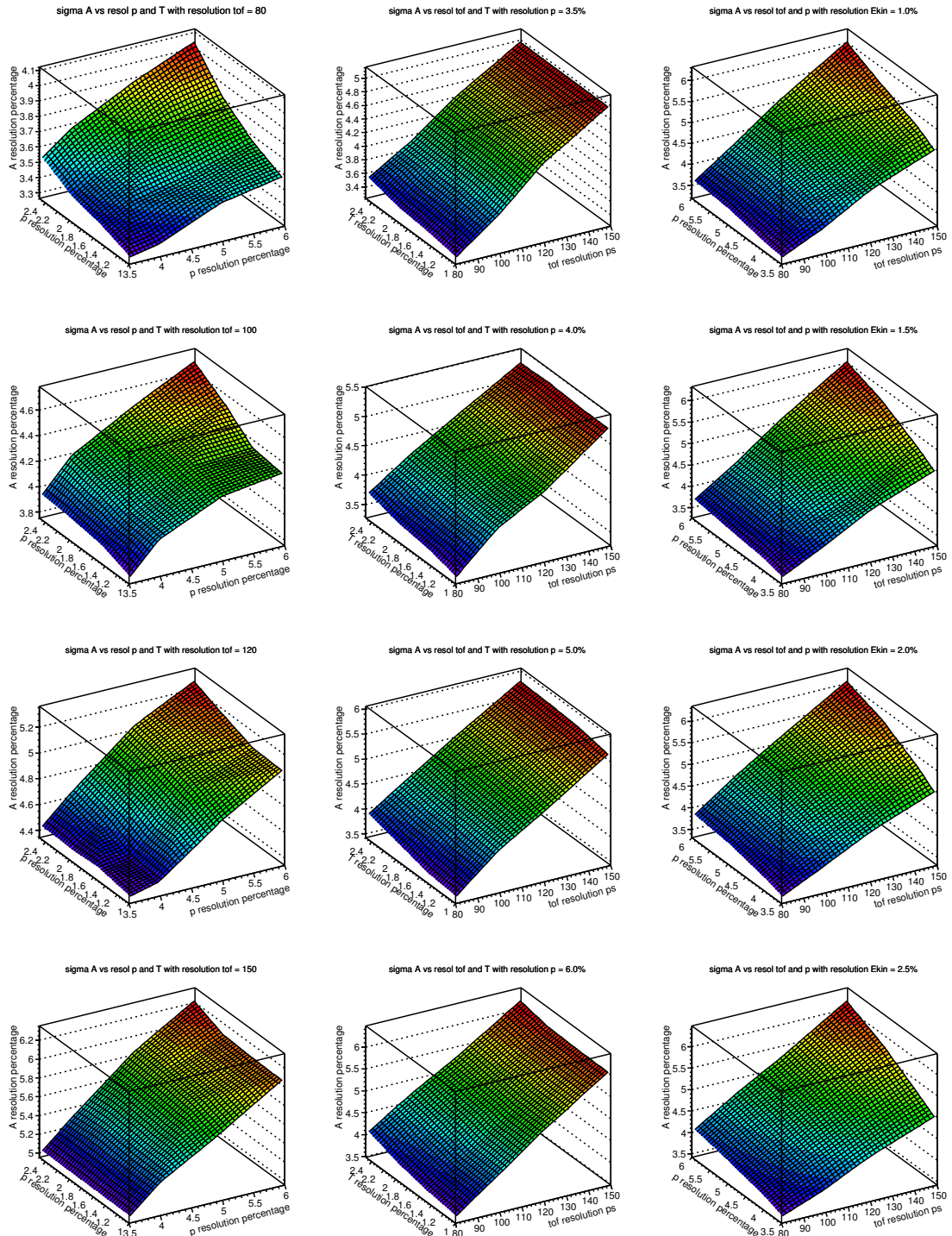


Figure 85 – Percentage precision on the determination of A for the ^{12}C fragment as obtained with the Augmented Lagrangian method approach after the application of a $\chi^2 < 5$ cut. The four plots on the left column concern the A resolution as a function of p (X axis) and E_k (Y axis) accuracies for four different values of the TOF resolution. The four plots in the central columns concern the A resolution as a function of the TOF (X axis) and E_k (Y axis) accuracies for four different values of the p resolution. The four plots in the right column concern the A resolution as a function of the TOF (X axis) and p (Y axis) accuracies for four different values of the E_k resolution.

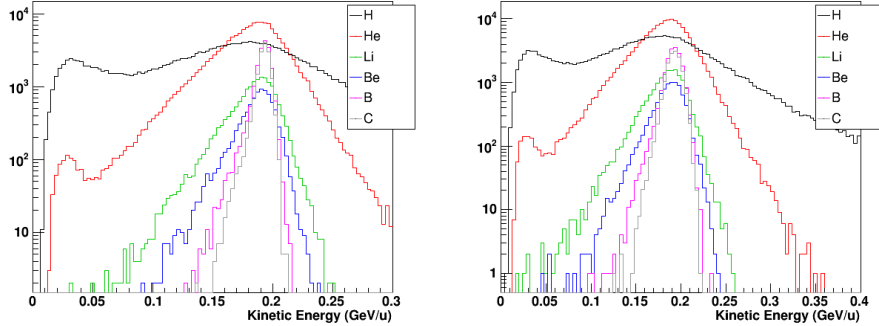


Figure 86 – Kinetic energy distribution for fragments produced in inelastic interactions of a 200 MeV/u ^{12}C beam with C target.

8.5. Inverse Kinematics

The idea of obtaining proton cross sections by using an inverse kinematic approach was adopted in several studies since the 1990s. Webber *et al.* [101] calculated the fragment production cross section on hydrogen using ^{12}C and ^{16}O beams with energy 300 MeV/u and above. Charge-changing and fragment production cross sections on hydrogen at 0° were measured by Zeitlin [102]: cross sections were calculated by subtracting data obtained for interactions of 290 MeV/u and 400 MeV/u ^{12}C beams with a carbon and a polyethylene target. The results were compared with PHITS [103] simulations, but the agreement appeared to be poor. Dudouet *et al.* [5] measured the double differential cross sections for hydrogen by combining the data obtained in carbon and CH_2 targets with a ^{12}C beam at 95 MeV/u.

The FOOT performances in terms of cross-section measurement were evaluated using simulated data of ^{12}C at 200 MeV/u. In order to obtain the differential cross sections for hydrogen, 2 mm-thick C_2H_4 and C targets were used. The detector response was implemented by applying the following smearing effects to the kinematical variables predicted by the simulation:

- gaussian smearing on the incident ^{12}C beam, $\sigma_\theta^{beam} = 3$ mrad
- gaussian smearing on the fragment, $\sigma_\theta^{frag} = 3$ mrad
- resolution on the total kinetic energy of the fragment, $\sigma_E/E = 3\%$
- resolution on the momentum of the fragment, $\sigma_p/p = 4\%$.

The finite angular acceptance of the experimental setup was reproduced by selecting only fragments that reach the calorimeter. This selection does not affect heavy nuclei such as Li, Be, B and C, but introduces an inefficiency for light nuclei amounting to $\sim 25\%$ for He and $\sim 70\%$ for H.

The kinetic energy distribution before and after the smearing is reported in Fig. 86 for different fragments (H, He, Li, Be, B, C) produced in a carbon target. Figure 87 shows the kinetic energy distribution for the same fragments in inverse kinematics.

The residuals between the generated and smeared kinetic energies ($\Delta E = E_{kin,gen} - E_{kin,smeared}$) show a gaussian behavior if evaluated in direct kinematics, while an asymmetric distribution with non-gaussian tails is obtained if inverse kinematics is considered. Figure 88 show ΔE for He fragments produced in 200 MeV/u C interactions with a carbon target, evaluated in direct (left panel) and inverse (right panel) kinematics. Table 18 reports the mean values and standard deviations of ΔE distributions for different fragments.

The energy differential cross-sections of different fragments obtained in inverse kinematics for C_2H_4 and C targets are reported in Fig. 89.

The hydrogen cross section has been obtained by combining the cross sections on C_2H_4 and C targets as follows:

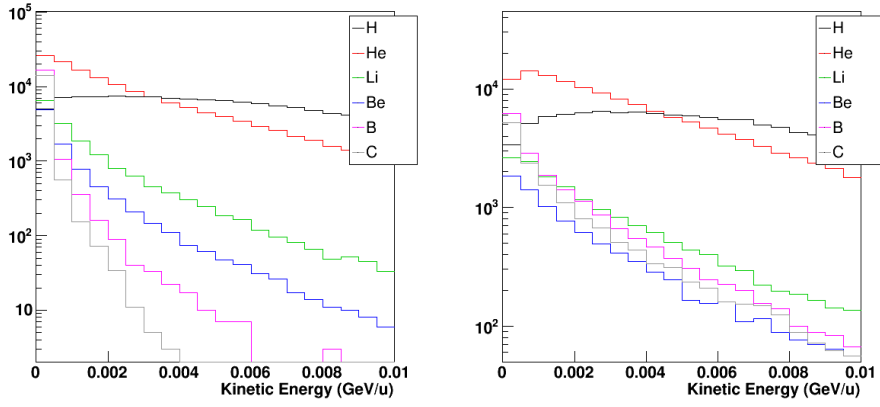


Figure 87 – Kinetic energy distribution in inverse kinematics for fragments produced in inelastic interactions of a 200 MeV/u ^{12}C beam with a C target.

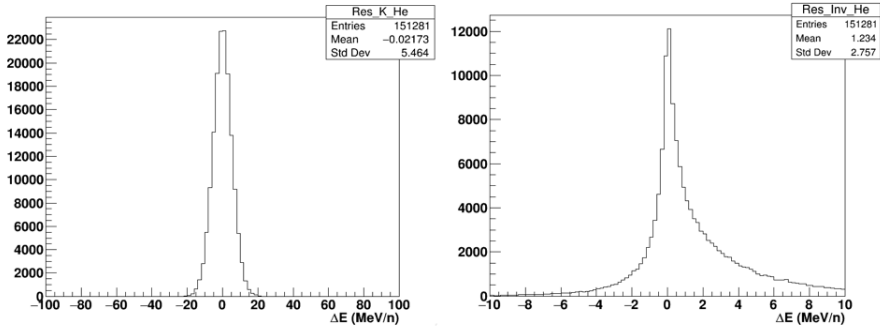


Figure 88 – ΔE for He fragments produced in 200 MeV/u C interactions with a carbon target, evaluated in direct (left) and inverse (right) kinematics.

$E_{rec} - E_{true}$ (Mev/u)	H		He		Li		Be		B		C	
	μ	σ										
Direct Kin	0.04	5.4	0.02	5.6	-0.07	5.7	-0.07	5.7	0.10	5.8	0.06	5.8
Inverse Kin	0.71	3.7	1.32	2.6	1.43	2.3	1.49	2.2	1.60	2.1	1.60	2.1

Table 18 – Mean value (μ) and standard deviation (σ) of ΔE distributions evaluated for different fragments in direct and inverse kinematics.

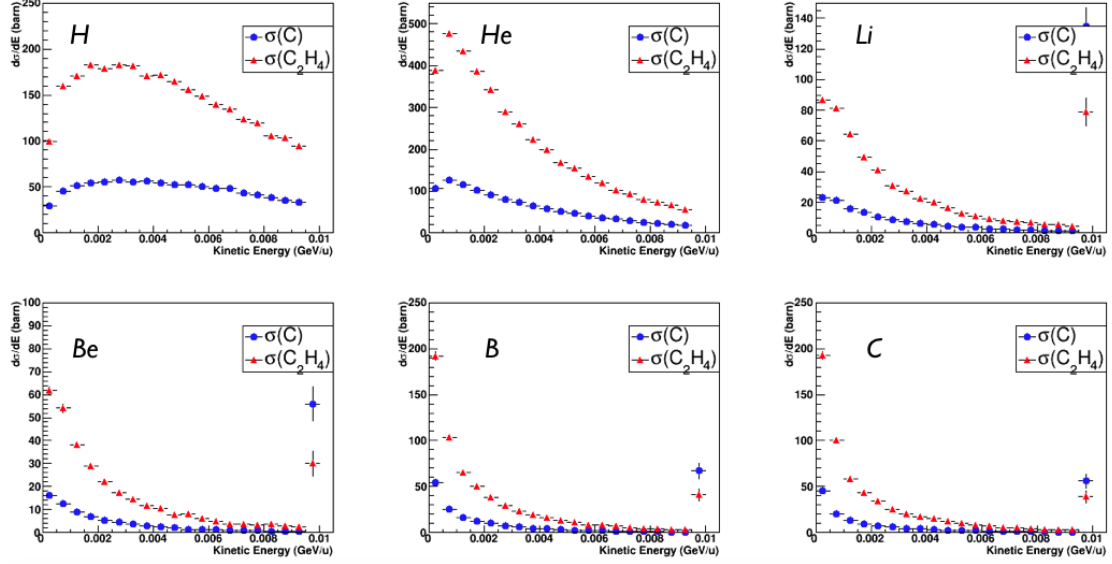


Figure 89 – Energy differential cross-sections of different fragments in inverse kinematics. Results obtained for C and C_2H_4 targets are reported as blue dots and red triangles, respectively.

$$\frac{d\sigma}{dE_{kin}}(H) = \frac{1}{4} \left(\frac{d\sigma}{dE_{kin}}(C_2H_4) - 2 \frac{d\sigma}{dE_{kin}}(C) \right) \quad (14)$$

1904 To check the validity of the target cross sections combination method we evaluated from the
 1905 simulated data both the cross section on hydrogen target and the cross section obtained from the
 1906 difference method. The comparison is reported in Fig. 90, that shows the energy differential cross
 1907 section of a 200 MeV/u ^{12}C beam on hydrogen target in inverse kinematics obtained with the
 1908 two methods. The results from the two estimations are in good agreements, thus validating the
 1909 combination method.

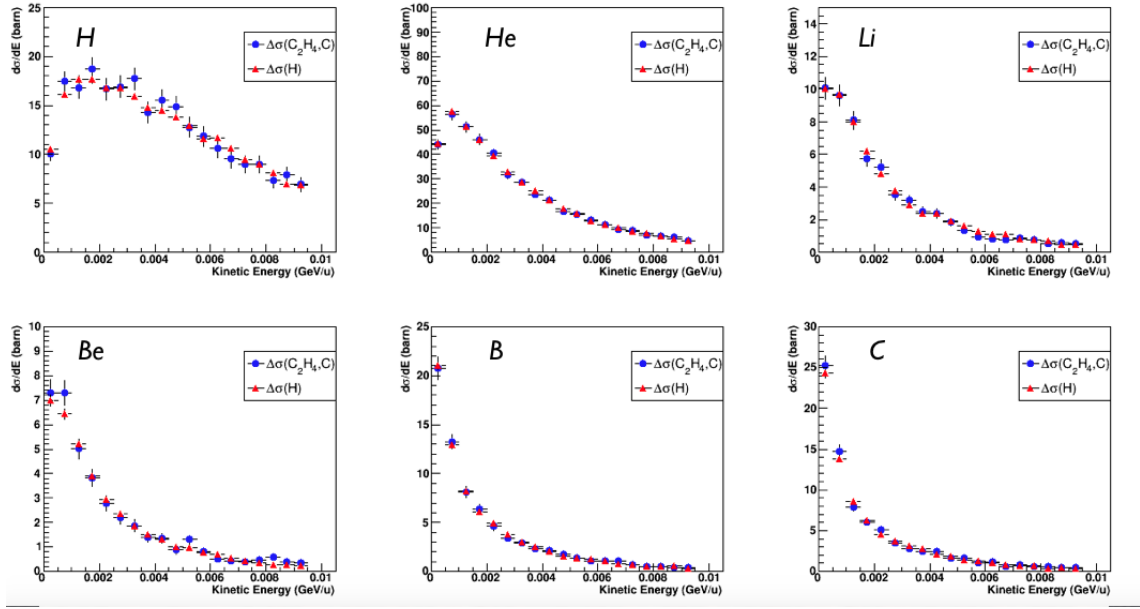


Figure 90 – Energy differential cross-section of a 200 MeV/u ^{12}C beam on hydrogen target in inverse kinematics. The estimations performed with the $\Delta\sigma(\text{C}_2\text{H}_4, \text{C})$ and $\sigma(\text{H})$ methods are reported as blue dots and red triangles, respectively.

1910 9. Logistics and Timescale

1911 The timescale of the experiment is dictated by the time needed to build the detector. In
1912 particular there are separate timescales for the emulsion setup and the electronic setup. The
1913 emulsion setup will be completed in the second part of 2018 and the corresponding data taking
1914 can be foreseen by the end of 2018 or early 2019. The electronic setup requires more time to
1915 be completed. In particular the assembling and calibration of the calorimeter push the end of
1916 construction phase up to late 2019/ early 2010. Of course this time schedule can also suffer from
1917 possible unavailability of beam for prototype tests and mission funding shortage.

1918 The priority needs of beam types for the FOOT data taking are ^{12}C and ^{16}O , with energies
1919 in the range 200-400 MeV/u for the study of the fragmentation in particle therapy. Additional
1920 research programs can be pursued with ^4He , ^{12}C and ^{16}O with energies up to 800 MeV/u for
1921 radioprotection in space.

1922 The European facilities with such beams expected to be operational in 2020 are few:

- 1923** • the CNAO experimental hall, with carbon (and maybe other ion species) beams with energy
1924 up to 400 MeV/u. The experimental hall at the moment in construction but it will be
1925 large enough to host the FOOT setup. Some uncertainties concern the possibility to have
1926 helium and oxygen beam within 2020 due to authorization issues.
- 1927** • The Heidelberg experimental room with ^4He , ^{12}C and ^{16}O beams up to 400 MeV/u. The
1928 HIT facility seems to be quite a safe choice at the moment, since the experimental hall has
1929 been routinely used for research for years (also by some of FOOT collaborators). The size
1930 of the experimental room puts a limit on the detector size due to the $\simeq 2.5$ m of distance
1931 between the beam exit window and the beam dump.
- 1932** • The cave A of GSI, where all the ^4He , ^{12}C and ^{16}O beams are present with the needed energy
1933 range. The experimental cave in GSI is large enough to host without problems our setup.
1934 On the other hand the amount of requests for beam time during 2020 is foreseen to be huge
1935 and could be a serious problem to get the required beam time

1936 The possibility to take data at BNL Laboratory (USA) or at HIMAC (Japan) is at present ruled
1937 out for cost reasons.

1938 The FOOT detector has been designed to be movable and of maximum size of the order of 2
1939 meters (length) times 1 meter (transverse dimension), and this feature allows us to pick any choice
1940 among the possible experimental sites listed above.

1941 A crucial parameter will be also the amount of required beam time. This is driven by the
1942 maximum acquisition rate sustainable by the FOOT system (order of 1 kHz) and the amount
1943 of statistics necessary to accomplish the experimental goals, which are different for the different
1944 types of measurements. For instance, if we stick to your main aim, the target fragmentation
1945 measurement, we can estimate the needed statistics asking that the statistical fluctuation of the
1946 energy fluctuation of the energy distribution in the patient frame of the less frequent isotope of
1947 interest is below the 10% level, as requested by the radiobiology model computation. Such an
1948 approach has intrinsic uncertainty due to:

- 1949** • the nuclear fragmentation model used for the computation (can be easily off also by a factor
1950 2-3 depending on specific isotopes production)
- 1951** • lack of precise knowledge of the detector, reconstruction and, even more important, the
1952 analysis cut efficiencies. A coarse evaluation of 50% could be a rough estimate
- 1953** • additive statistic needed for detector calibration and as control sample to check systematic.

1954 All these sources of uncertainty force us to adopt a safety factor of 10 with respect to the minimum
1955 amount of events computed only on the basis of the minimum desired statistical significance on

Measurement	beam	target	E_{kin} MeV/u	N_{prim}	N_{prim}^{tot}	T(s)
Target Frag.	C, O, He	C, C_2H_4 , PMMA	200, 150	8×10^7	9.6×10^8	4.8×10^5
Project. Frag.	C, O, He	C, C_2H_4 , PMMA	350, 400	3.2×10^7	3.8×10^8	2.0×10^5
Space	C, O, He	C_2H_4	600, 800	1.0×10^7	4×10^7	2.0×10^4

Table 19 – Table of the beam time needed for each FOOT measurements. A 2 mm thickness of the target and a acquisition rate of 2 kHz are assumed

1956 the fragment energy distributions, considering a proper binning comparable to the needed energy
 1957 resolution.

1958 Of course there is a last factor to be taken into account: the target thickness. The thicker
 1959 the target, the higher the fragmentation probability and then the fragmentation events yield for
 1960 each primary. Unfortunately a too thick target may induce too much multiple scattering of the
 1961 produced fragments thus spoiling the energy measurement in the patient frame, as shown by the
 1962 inverse kinematic studies reported in Sec 8.5. A good compromise is a target with a thickness
 1963 of the order of $2 \div 4$ g/cm² (2 mm of polyethylene or graphite). For instance, a ^{12}C beam at 200
 1964 MeV/u kinetic energy impinging on 2 mm of graphite will provide the necessary statistics after
 1965 $\simeq 8 \times 10^7$ primaries. Note that the same number of primaries are needed for each set of desired
 1966 beam/target/energy.

1967 As far as the projectile fragmentation measurement is concerned, there is no need to apply a
 1968 Lorentz boost to the fragments so that the constraint on the induced multiple scattering can be
 1969 relaxed. Attention must be paid only to the re-fragmentation probability of the produced fragments
 1970 in the target, thus allowing to increase to 5 mm the thickness of the target, with corresponding
 1971 reduction of the primaries needed for the measurements. Assuming approximatively the same
 1972 efficiency at 350-400 MeV/u of beam energy required for the study of projectile fragmentation, we
 1973 can estimate $\simeq 3.2 \times 10^7$ primaries per measurement.

1974 The statistics needed by the measurements devoted to radioprotection in space (namely with
 1975 beams of 700-800 MeV/u) is reduced with respect to the other cases discussed above. During the
 1976 first data taking season of FOOT we will primarily focus on the charge-changing cross section,
 1977 without the need of the mass identification. For this measurement we will need at least an order
 1978 of magnitude less event than in the corresponding projectile fragmentation measurement. Taking
 1979 into account an overall efficiency drop of 50% with respect to the measurements designed at 200
 1980 MeV/u, we can estimate a number of primaries of the order of $\simeq 5 \times 10^6$.

1981 The measurements performed with the emulsion setup generally do not need a large amount
 1982 of beam time, due to the focus on the most abundant, low A and Z fragment production. On the
 1983 contrary, as we already reported, care will be needed to keep the beam intensity at such a low level
 1984 to avoid the geometrical pile-up of the fragments tracks in the ES.

1985 In the table 19 we summarise the beam requests to perform the most demanding (from the
 1986 beam time point of view) measurements of the FOOT physics program.

1987 References

- 1988** [1] M. Jermann, "Particle therapy statistics in 2014," *Int. J. Part. Ther.*, vol. 2, no. 1, pp. 50–54, 2015.
- 1989** [2] M. Durante and J. Loeffler, "Charged particles in radiation oncology," *Nat. Rev. Clin. Onc.*, vol. 7, no. 1, pp. 37–43, 2010.
- 1990**
- 1991** [3] J. Tang *et al.*, "Comparison of radiobiological effective depths in 65-MeV modulated proton beams," *Brit. J. Cancer*, vol. 76, no. 2, p. 220, 1997.
- 1992**
- 1993** [4] F. Tommasino and M. Durante, "Proton radiobiology," *Cancers*, vol. 7, no. 1, pp. 353–381, 2015.
- 1994** [5] J. Dudouet *et al.*, "Double-differential fragmentation cross-sections measurements of 95 MeV/u ^{12}C beams on thin targets for hadrontherapy," *Phys. Rev. C*, vol. 88, no. 2, p. 024606, 2013.
- 1995**
- 1996** [6] M. Toppi *et al.*, "Measurement of fragmentation cross sections of ^{12}C ions on a thin gold target with the FIRST apparatus," *Phys. Rev. C*, vol. 93, no. 6, p. 064601, 2016.
- 1997**
- 1998** [7] W. Webber *et al.*, "Total charge and mass changing cross sections of relativistic nuclei in hydrogen, helium, and carbon targets," *Phys. Rev. C*, vol. 41, no. 2, p. 520, 1990.
- 1999**
- 2000** [8] A. Ferrari *et al.*, "FLUKA: a multi-particle transport code," 2005. CERN-2005-10, INFN TC_05/11, SLAC-R-773.
- 2001**
- 2002** [9] T. Böhlen *et al.*, "The FLUKA code: developments and challenges for high energy and medical applications," *Nucl. Data Sheets*, vol. 120, pp. 211–214, 2014.
- 2003**
- 2004** [10] J. Norbury *et al.*, "Review of nuclear physics experiments for space radiation," 2011. NASA/TP-2011-217179.
- 2005**
- 2006** [11] F. Tommasino *et al.*, "New ions for therapy," *Int. J. Part. Ther.*, vol. 2, no. 3, pp. 428–438, 2015.
- 2007** [12] "Prescribing Recording and Reporting Proton-beam Therapy," 2007. ICRU Report 78.
- 2008** [13] J. Guelette *et al.*, "RBE variation as a function of depth in the 200-MeV proton beam produced at the National Accelerator Centre in Faure (South Africa)," *Radiother. Oncol.*, vol. 42, no. 3, pp. 303–309, 1997.
- 2009**
- 2010**
- 2011** [14] H. Paganetti, "Relative biological effectiveness (RBE) values for proton beam therapy. Variations as a function of biological endpoint, dose, and linear energy transfer," *Phys. Med. Biol.*, vol. 59, no. 22, p. R419, 2014.
- 2012**
- 2013**
- 2014** [15] M. Durante and H. Paganetti, "Nuclear physics in particle therapy: a review," *Rep. Prog. Phys.*, vol. 79, no. 9, p. 096702, 2016.
- 2015**
- 2016** [16] D. Schardt *et al.*, "Heavy-ion tumor therapy: physical and radiobiological benefits," *Rev. Mod. Phys.*, vol. 82, no. 1, p. 383, 2010.
- 2017**
- 2018** [17] A. Lühr *et al.*, "The impact of modeling nuclear fragmentation on delivered dose and radiobiology in ion therapy," *Phys. Med. Biol.*, vol. 57, no. 16, p. 5169, 2012.
- 2019**
- 2020** [18] O. Steinsträter *et al.*, "Integration of a model-independent interface for RBE predictions in a treatment planning system for active particle beam scanning," *Phys. Med. Biol.*, vol. 60, no. 17, p. 6811, 2015.
- 2021**
- 2022** [19] M. Krämer *et al.*, "Treatment planning for heavy-ion radiotherapy: physical beam model and dose optimization," *Phys. Med. Biol.*, vol. 45, no. 11, p. 3299, 2000.
- 2023**
- 2024** [20] M. Krämer *et al.*, "Overview of recent advances in treatment planning for ion beam radiotherapy," *Eur. Phys. J. D*, vol. 68, no. 10, p. 306, 2014.
- 2025**
- 2026** [21] M. Krämer and M. Scholz, "Rapid calculation of biological effects in ion radiotherapy," *Phys. Med. Biol.*, vol. 51, no. 8, p. 1959, 2006.
- 2027**

- 2028 [22] E. Scifoni *et al.*, “Including oxygen enhancement ratio in ion beam treatment planning: model imple-
2029 mentation and experimental verification,” *Phys. Med. Biol.*, vol. 58, no. 11, p. 3871, 2013.
- 2030 [23] N. Bassler *et al.*, “LET-painting increases tumour control probability in hypoxic tumours,” *Acta
2031 Oncol.*, vol. 53, no. 1, pp. 25–32, 2014.
- 2032 [24] Elsässer T, Weyrather W, Friedrich T, Durante M, Iancu G, Kraßmer M, et al. “ Quantification
2033 of the relative biological effectiveness for Ion beam radiotherapy: direct experimental comparison of
2034 proton and carbon Ion beams and a novel approach for treatment planning.” *Int J Radiat Oncol Biol
2035 Phys.*;78(4):1177–83, 2010
- 2036 [25] Friedrich T, Scholz U, Elsässer T, Durante M, Scholz M. “ Calculation of the biological effects
2037 of ion beams based on the microscopic spatial damage distribution pattern.” *Int J Radiat Biol.*
2038 ;88(1–2):103–7, 2012
- 2039 [26] C. Grassberger and H. Paganetti, “Elevated let components in clinical proton beams,” *Phys. Med.
2040 Biol.*, vol. 56, pp. 6677–6691, 2011.
- 2041 [27] R. Grün *et al.*, “Assessment of potential advantages of relevant ions for particle therapy: A model
2042 based study,” *Med. Phys.*, vol. 42, no. 2, pp. 1037–1047, 2015.
- 2043 [28] D. Indelicato *et al.*, “Consensus Report From the Stockholm Pediatric Proton Therapy Conference,”
2044 *Int. J. Radiat. Oncol.*, vol. 96, no. 2, pp. 387–392, 2016.
- 2045 [29] B. Knäusl *et al.*, “Can particle beam therapy be improved using helium ions? - a planning study
2046 focusing on pediatric patients,” *Acta Oncol.*, vol. 55, no. 6, pp. 751–759, 2016.
- 2047 [30] M. Rovituso *et al.*, “Fragmentation of 120 and 200 MeV/u ^4He ions in water and PMMA targets,”
2048 *Phys. Med. Biol.*, vol. 62, no. 4, p. 1310, 2017.
- 2049 [31] M. Krämer *et al.*, “Helium ions for radiotherapy? Physical and biological verifications of a novel
2050 treatment modality,” *Med. Phys.*, vol. 43, no. 4, pp. 1995–2004, 2016.
- 2051 [32] M. Marafini *et al.*, “Secondary radiation measurements for particle therapy applications: nuclear
2052 fragmentation produced by ^4He ion beams in a PMMA target,” *Phys. Med. Biol.*, vol. 62, no. 4,
2053 p. 1291, 2017.
- 2054 [33] M. Durante and F. Cucinotta, “Physical basis of radiation protection in space travel,” *Rev. Mod.
2055 Phys.*, vol. 83, no. 4, p. 1245, 2011.
- 2056 [34] J. Norbury *et al.*, “Nuclear data for space radiation,” *Radiat. Meas.*, vol. 47, no. 5, pp. 315–363, 2012.
- 2057 [35] Z. Abou-Haidar *et al.*, “Performance of upstream interaction region detectors for the FIRST experi-
2058 ment at GSI,” *J. Instrum.*, vol. 7, no. 02, p. P02006, 2012.
- 2059 [36] A. Paoloni *et al.*, “The Upstream Detectors of the FIRST Experiment at GSI,” *Physics Proc.*, vol. 37,
2060 pp. 1466–1472, 2012.
- 2061 [37] M. Anelli *et al.*, “FIRST experiment upstream detectors performance on GSI 400 MeV/u ^{12}C beam,”
2062 in *Nuclear Science Symposium and Medical Imaging Conference*, pp. 2800–2804, IEEE, 2011.
- 2063 [38] C. Sanelli, “Studio di fattibilità dei magneti in configurazione Hallbach dello spettrometro
2064 dell’esperimento FOOT.” INFN-17-10/LNF internal note, May 22 2017.
- 2065 [39] S. I. P. group. www.iphc.cnrs.fr/PICSEL.html.
- 2066 [40] L. Greiner *et al.*, “A MAPS based vertex detector for the STAR experiment at RHIC,” *Nucl. Instrum.
2067 Meth. A*, vol. 650, no. 1, pp. 68–72, 2011.
- 2068 [41] I. Valin *et al.*, “A reticle size CMOS pixel sensor dedicated to the STAR HFT,” *J. Instrum.*, vol. 7,
2069 no. 01, p. C01102, 2012.

- 2070 [42] W. de Boer *et al.*, “Measurements with a CMOS pixel sensor in magnetic fields,” *Nucl. Instrum. Meth. A*, vol. 487, no. 1, pp. 163–169, 2002.
- 2071
- 2072 [43] “PLUME website: www.iphc.cnrs.fr/PLUME.html.”
- 2073 [44] “ERG Aerospace Corporation website: www.ergaerospace.com/SiC-properties.htm.”
- 2074 [45] “G&A Engineering company website: www.gaengineering.com.”
- 2075 [46] P. Fernández-Martínez *et al.*, “Simulation of new p-type strip detectors with trench to enhance the charge multiplication effect in the n-type electrodes,” *Nucl. Instrum. Meth. A*, vol. 658, no. 1, pp. 98–102, 2011.
- 2076
- 2077
- 2078 [47] H.-W. Sadrozinski *et al.*, “Sensors for ultra-fast silicon detectors,” *Nucl. Instrum. Meth. A*, vol. 765, pp. 7–11, 2014.
- 2079
- 2080 [48] G. Pellegrini *et al.*, “Technology developments and first measurements of Low Gain Avalanche Detectors (LGAD) for high energy physics applications,” *Nucl. Instrum. Meth. A*, vol. 765, pp. 12–16, 2014.
- 2081
- 2082
- 2083 [49] M. Garcia-Sciveres and N. Wermes, “Advances in pixel detectors for experiments with high rate and radiation,” arXiv preprint [arXiv:1705.10150](https://arxiv.org/abs/1705.10150), 2017.
- 2084
- 2085 [50] S. Meroli *et al.*, “Energy loss measurement for charged particles in very thin silicon layers,” *J. Instrum.*, vol. 6, no. 06, p. P06013, 2011.
- 2086
- 2087 [51] O. Adriani *et al.*, “Beam test results for single- and double-sided silicon detector prototypes of the CMS central detector,” *Nucl. Instrum. Meth. A*, vol. 396, no. 1–2, pp. 76–92, 1997.
- 2088
- 2089 [52] B. Alpat *et al.*, “The internal alignment and position resolution of the AMS-02 silicon tracker determined with cosmic-ray muons,” *Nucl. Instrum. Meth. A*, vol. 613, no. 2, pp. 207–217, 2010.
- 2090
- 2091 [53] B. Alpat *et al.*, “High-precision tracking and charge selection with silicon strip detectors for relativistic ions,” *Nucl. Instrum. Meth. A*, vol. 446, no. 3, pp. 522–535, 2000.
- 2092
- 2093 [54] P. Zuccon *et al.*, “The AMS silicon tracker: Construction and performance,” *Nucl. Instrum. Meth. A*, vol. 596, no. 1, pp. 74–78, 2008.
- 2094
- 2095 [55] T. Ohsugi *et al.*, “Design and properties of the GLAST flight silicon micro-strip sensors,” *Nucl. Instrum. Meth. A*, vol. 541, no. 1, pp. 29–39, 2005.
- 2096
- 2097 [56] H. Moser *et al.*, “Thinned Silicon Detectors,” in *International Workshop on Vertex Detectors*, PoS (Vertex 2007) 013, 2007.
- 2098
- 2099 [57] R. Arcidiacono *et al.*, “Test of UFSD Silicon Detectors for the TOTEM Upgrade Project,” arXiv preprint [arXiv:1702.05180](https://arxiv.org/abs/1702.05180), 2017.
- 2100
- 2101 [58] N. Minafra *et al.*, “Test of Ultra Fast Silicon Detectors for Picosecond Time Measurements with a New Multipurpose Read-Out Board,” *Nucl. Instrum. Meth. A*, 2017.
- 2102
- 2103 [59] F. Zhang *et al.*, “Design of the readout electronics for the DAMPE Silicon Tracker detector,” *Chinese Phys. C*, vol. 40, no. 11, p. 116101, 2016.
- 2104
- 2105 [60] “Gamma Medical Ideas VA140 Document datasheet (V0R1),” 2011.
- 2106
- 2107 [61] F. Zhang *et al.*, “A prototype silicon detector system for space cosmic-ray charge measurement,” *Chinese Phys. C*, vol. 38, no. 6, p. 066101, 2014.
- 2108
- 2109 [62] P. Marrocchesi *et al.*, “Beam test performance of a scintillator-based detector for the charge identification of relativistic ions,” *Nucl. Instrum. Meth. A*, vol. 659, no. 1, pp. 477–483, 2011.
- 2110
- 2111 [63] “www.epic-crystal.com/shop_reviews/plastic-scintillator.”
- 2112
- 2113 [64] “advansid.com/products/product-detail/asd-rgb-nuv-3s-p.”

- ²¹¹² [65] F. Acerbi *et al.*, “Characterization of single-photon time resolution: from single SPAD to silicon
²¹¹³ photomultiplier,” *IEEE T. Nucl. Sci.*, vol. 61, no. 5, pp. 2678–2686, 2014.
- ²¹¹⁴ [66] S. Ritt, “The DRS chip: Cheap waveform digitizing in the GHz range,” *Nucl. Instrum. Meth. A*,
²¹¹⁵ vol. 518, no. 1, pp. 470–471, 2004.
- ²¹¹⁶ [67] M. Francesconi *et al.*, “A new generation of integrated trigger and read out system for the MEG II
²¹¹⁷ experiment,” in *5th International Conference on Modern Circuits and Systems Technologies*, IEEE,
²¹¹⁸ 2016.
- ²¹¹⁹ [68] www.hzcpophotonics.com/en_index.html
- ²¹²⁰ [69] M. Raggi, V. Kozuharov, “Proposal to search for a dark photon in e+ on target collisions at DĀNE
²¹²¹ linac”, Advances in High Energy Physics Volume 2014 (2014), Article ID 959802
- ²¹²² [70] M. Raggi *et al.*, “Performance of the PADME Calorimeter prototype at the DANE BTF”, *Nucl.
Instrum. Meth. A*, vol. 862, pp 31-35, 2017
- ²¹²⁴ [71] G. De Lellis *et al.*, “Nuclear emulsions,” in CW Fabjan and H Schopper, *Elementary Particles: Detectors for Particles and Radiation*, vol. 21B, Springer, 2011.
- ²¹²⁶ [72] M. De Serio *et al.*, “High precision measurements with nuclear emulsions using fast automated microscopes,” *Nucl. Instrum. Meth. A*, vol. 554, no. 1, pp. 247–254, 2005.
- ²¹²⁸ [73] N. Armenise *et al.*, “High-speed particle tracking in nuclear emulsion by last-generation automatic
²¹²⁹ microscopes,” *Nucl. Instrum. Meth. A*, vol. 551, no. 2, pp. 261–270, 2005.
- ²¹³⁰ [74] L. Arrabito *et al.*, “Hardware performance of a scanning system for high speed analysis of nuclear
²¹³¹ emulsions,” *Nucl. Instrum. Meth. A*, vol. 568, no. 2, pp. 578–587, 2006.
- ²¹³² [75] A. Alexandrov *et al.*, “Further progress for a fast scanning of nuclear emulsions with Large Angle
²¹³³ Scanning System,” *J. Instrum.*, vol. 9, no. 02, p. C02034, 2014.
- ²¹³⁴ [76] A. Alexandrov *et al.*, “A new fast scanning system for the measurement of large angle tracks in nuclear
²¹³⁵ emulsions,” *J. Instrum.*, vol. 10, no. 11, p. P11006, 2015.
- ²¹³⁶ [77] A. Alexandrov *et al.*, “A new generation scanning system for the high-speed analysis of nuclear emulsions,” *J. Instrum.*, vol. 11, no. 06, p. P06002, 2016.
- ²¹³⁸ [78] A. Alexandrov *et al.*, “The continuous motion technique for the new generation scanning system,”
²¹³⁹ submitted to *J. Instrum.*, 2017.
- ²¹⁴⁰ [79] E. Eskut *et al.*, “The CHORUS experiment to search for $\nu_\mu \rightarrow \nu_\tau$ oscillation,” *Nucl. Instrum. Meth.
A*, vol. 401, no. 1, pp. 7–44, 1997.
- ²¹⁴² [80] R. Acquafredda *et al.*, “The OPERA experiment in the CERN to Gran Sasso neutrino beam,” *J.
Instrum.*, vol. 4, no. 04, p. P04018, 2009.
- ²¹⁴⁴ [81] N. Agafonova *et al.*, “Discovery of τ Neutrino Appearance in the CNGS Neutrino Beam with the
²¹⁴⁵ OPERA Experiment,” *Phys. Rev. Lett.*, vol. 115, no. 12, p. 121802, 2015.
- ²¹⁴⁶ [82] T. Nakamura *et al.*, “The OPERA film: New nuclear emulsion for large-scale, high-precision experiments,” *Nucl. Instrum. Meth. A*, vol. 556, no. 1, pp. 80–86, 2006.
- ²¹⁴⁸ [83] G. De Lellis *et al.*, “Emulsion Cloud Chamber technique to measure the fragmentation of a high-energy
²¹⁴⁹ carbon beam,” *J. Instrum.*, vol. 2, no. 06, p. P06004, 2007.
- ²¹⁵⁰ [84] G. De Lellis *et al.*, “Measurement of the fragmentation of Carbon nuclei used in hadron-therapy,”
²¹⁵¹ *Nucl. Phys. A*, vol. 853, no. 1, pp. 124–134, 2011.
- ²¹⁵² [85] A. Aleksandrov *et al.*, “Measurement of large angle fragments induced by 400 MeV n⁻¹ carbon ion
²¹⁵³ beams,” *Meas. Sci. Technol.*, vol. 26, no. 9, p. 094001, 2015.

- ²¹⁵⁴ [86] N. I. of Standards and Technology. <https://www.nist.gov>.
- ²¹⁵⁵ [87] N. Agafonova *et al.*, “Momentum measurement by the multiple coulomb scattering method in the
²¹⁵⁶ OPERA lead-emulsion target,” *New J. Phys.*, vol. 14, no. 1, p. 013026, 2012.
- ²¹⁵⁷ [88] M. De Serio *et al.*, “Momentum measurement by the angular method in the Emulsion Cloud Chamber,”
²¹⁵⁸ *Nucl. Instrum. Meth. A*, vol. 512, no. 3, pp. 539–545, 2003.
- ²¹⁵⁹ [89] A. T. Collaboration *et al.*, “The ATLAS Data Acquisition and High Level Trigger system,” *J. Instrum.*,
²¹⁶⁰ vol. 11, no. 06, p. P06008, 2016.
- ²¹⁶¹ [90] S. Bettarini *et al.*, “The SLIM5 low mass silicon tracker demonstrator,” *Nucl. Instrum. Meth. A*,
²¹⁶² vol. 623, no. 3, pp. 942–953, 2010.
- ²¹⁶³ [91] C. Sbarra *et al.*, “The data acquisition system of the superB-SVT beam test,” *Nucl. Instrum. Meth. A*,
²¹⁶⁴ vol. 718, pp. 243–244, 2013.
- ²¹⁶⁵ [92] E. Logbook. midas.psi.ch/elog.
- ²¹⁶⁶ [93] G. Battistoni *et al.*, “The FLUKA code: an accurate simulation tool for Particle Therapy,” *Fron. Oncol.*, vol. 6, p. 116, 2016.
- ²¹⁶⁸ [94] R. Pleskac *et al.*, “The FIRST experiment at GSI,” *Nucl. Instrum. Meth. A*, vol. 678, pp. 130–138,
²¹⁶⁹ 2012.
- ²¹⁷⁰ [95] C. Agodi *et al.*, “Charged particle’s flux measurement from PMMA irradiated by 80 MeV/u carbon
²¹⁷¹ ion beam,” *Phys. Med. Biol.*, vol. 57, no. 18, p. 5667, 2012.
- ²¹⁷² [96] L. Piersanti *et al.*, “Measurement of charged particle yields from PMMA irradiated by a 220 MeV/u
²¹⁷³ ^{12}C beam,” *Phys. Med. Biol.*, vol. 59, no. 7, p. 1857, 2014.
- ²¹⁷⁴ [97] I. Mattei *et al.*, “Secondary radiation measurements for particle therapy applications: prompt photons
²¹⁷⁵ produced by ^4He , ^{12}C and ^{16}O ion beams in a PMMA target,” *Phys. Med. Biol.*, vol. 62, no. 4, p. 1438,
²¹⁷⁶ 2017.
- ²¹⁷⁷ [98] V. Vlachoudis *et al.*, “FLAIR: a powerful but user friendly graphical interface for FLUKA,” in *International Conference on Mathematics, Computational Methods & Reactor Physics*, 2009.
- ²¹⁷⁹ [99] J. Rauch and T. Schlüter, “GENFIT – a Generic Track-Fitting Toolkit,” in *J. Phys. Conf. Ser.*,
²¹⁸⁰ vol. 608, p. 012042, 2015.
- ²¹⁸¹ [100] W. Cho *et al.*, “OPTIMASS: a package for the minimization of kinematic mass functions with
²¹⁸² constraints,” *J. High Energy Phys.*, vol. 2016, no. 1, p. 26, 2016.
- ²¹⁸³ [101] W. Webber *et al.*, “Individual charge changing fragmentation cross sections of relativistic nuclei in
²¹⁸⁴ hydrogen, helium, and carbon targets,” *Phys. Rev. C*, vol. 41, no. 2, p. 533, 1990.
- ²¹⁸⁵ [102] C. Zeitlin *et al.*, “Fragmentation cross sections of 290 and 400 MeV/nucleon ^{12}C beams on elemental
²¹⁸⁶ targets,” *Phys. Rev. C*, vol. 76, no. 1, p. 014911, 2007.
- ²¹⁸⁷ [103] T. Sato *et al.*, “Particle and Heavy Ion Transport code System, PHITS, version 2.52,” *J. Nucl. Sci. Technol.*,
²¹⁸⁸ vol. 50, no. 9, pp. 913–923, 2013.